Evaluation of the PEREGRINE Monte Carlo dose calculation code for 6 MV photon beams

Emily C. Heath

Department of Medical Physics
McGill University, Montreal
June 2003

A thesis submitted to the Faculty of Graduate Studies and Research in partial fulfillment of the requirements of the degree of Master of Science in Medical Radiation Physics

Abstract

The accuracy of conventional dose calculation algorithms employed in external photon beam treatment planning is limited by their inability to fully model the radiation source and account for the electron fluence perturbations which occur in regions of non-uniform density. In this work, we evaluated the dosimetric accuracy of the PEREGRINE Monte Carlo dose calculation code for 6 MV photons. Dose profiles calculated by PEREGRINE were compared with measurements in homogeneous and heterogeneous phantoms. A comparison of dose profiles calculated by PEREGRINE and the EGSnrc Monte Carlo code was also performed. To fully model the Varian Millennium 120 leaf collimator, a new MLC component module was developed for BEAMnrc.

Overall, the agreement between PEREGRINE and measurements and EGSnrc is within 1% with the exception of the buildup region, where the accuracy of the beam model is affected by an artificially increased electron subsource weight, and for 30x30 cm^2 fields where the beam model does not accurately predict the off-axis fluence. A clinical comparison of IMRT dose distributions calculated by PEREGRINE and the CORVUS pencil beam algorithm indicates that the heterogeneity correction implemented in CORVUS underestimates the dose received by sensitive structures, receiving up to 20% of the prescribed dose, which lie in the vicinity of low density tissues.

Résumé

Les algorithmes de calcul de dose, utilisés dans les systèmes de planification de traitements externes par photons, sont limités car ils ne modèlent pas adéquatement la source de radiation et ne tiennent pas compte des perturbations causées par les électrons dans les régions de densité non-uniforme. Dans cette étude, la précision du code de Monte Carlo PEREGRINE est évaluée pour des photons de 6MV. Les profils de dose obtenus avec PEREGRINE sont comparés avec des mesures de dose à l'intérieur de matériaux homogène et héterogène et avec des profils de dose obtenus avec Monte Carlo EGSnrc. Un nouveau module pour le collimateur multi-lame (CML) est developpé pour BEAMnrc afin d'obtenir un modele du Varian Millenium 120 collimateur multi-lame.

Les résultats obtenus avec PEREGRINE et EGSnrc et les mesures de dose a l'intérieur de matériaux sont en accord avec une marge d'erreur de 1 % à l'exception des régions d'accumulation, où la précision de PEREGRINE est affectée par l'augmentation artificielle du nombre d'électrons et à l'exception des champs de 30 × 30 cm^2 où PEREGRINE ne prédit plus la fluence dans les régions de pénombre. Une comparaison des distributions de dose pour un plan de radiothérapie par intensité modulée (TRIM) calculées avec PEREGRINE et l'algorithme de CORVUS démontre que le système de correction employé par CORVUS sous-estime la dose reçue par les organes dans les régions où la dose est minime.

Acknowledgements

I would first like to acknowledge the invaluable support of my two supervisors, Dr. Jan P. Seuntjens and William Parker. Their continued guidance, availability for discussion, and encouragement at all stages of this project made it a very enjoyable experience.

I would also like to thank Dr. Ervin Podgorsak for teaching me about Medical Physics as well as for providing me the opportunity to study in the excellent academic environment of the McGill Medical Physics program.

Much of this work would not have been possible without the significant assistance of Bruce Curran, formerly of NOMOS, particularly for providing the mathematical phantoms for the PEREGRINE evaluation and his assistance with all issues relating to PEREGRINE and CORVUS. I would also like to acknowledge the financial support of NOMOS Corporation who provided partial funding for this project.

I would like to acknowledge the assistance of the staff at the McGill Medical Physics Unit including Michael Evans for the many hours spent assisting me with water tank measurements, Marina Olivares for help with TLD measurements, as well as Joe Larkin and Pierre Leger for assistance with physical measurements on the MLC and interpretation of technical drawings.

Among the students at the MPU, I would like to thank Genevieve Jarry for translating the abstract into French, Wamied Abdel-Rahman for useful discussions and advice on many topics including Monte Carlo simulations of ion chamber response, Khalid Al-Yahya whose thesis work provided a guide for my validation work with the MLC component module as well as methods for comparing patient dose distributions, and Robert Doucet for advice on TLD measurement techniques.

Table of Contents

List of Figures

Chapter 1

Chapter 2

Chapter 3

Chapter 4

Chapter 5

Chapter 6

List of Tables

Chapter 5

Chapter 1:

Introduction

1.1 Introduction

In 2002 136,900 new cases of cancer were diagnosed and 66,200 deaths were attributed to cancer making it the leading cause of premature death in Canada[1]. Of those newly diagnosed cases, approximately half received radiation therapy alone or in conjunction with another form of treatment. Ionizing radiation has been used in the treatment of cancer since shortly after the discovery of x-rays by Roentgen in 1895 and the subsequent discovery of radioactivity by Becquerel in 1896.

The radiobiological basis for radiation therapy is that ionizing radiation kills cells by damaging their DNA. The incident radiation transfers energy either directly, or indirectly through the formation of chemically reactive free radicals, to the DNA molecule resulting in the breaking of chemical bonds[2]. When many of these events occur in close proximity, multiple breaks in the sugar-phosphate backbone of the DNA molecule lead to double strand breaks (DSBs). The inability of the cell to correctly repair these DSBs causes the cell to die either spontaneously or during the cell replication process.

1.2 Radiation therapy

Radiation therapy is separated into two main areas: brachytherapy and external beam therapy. Brachytherapy consists of placing sealed radioactive sources inside or around the tumour whereas in external beam therapy radiation is delivered by a source outside the patient. The sources of the ionizing radiation used in external beam therapy include radioisotope units and accelerators. Radioisotope units make use of high energy gamma rays produced by the decay of an unstable isotope such as Cobalt-60 to a lower energy state.

Accelerators produce ionizing radiation by accelerating charged particles to high energies and colliding them into a target made of a high atomic number material. As the particles decelerate in the target, bremsstrahlung photons are produced with a spectrum of energies characterized by the accelerating potential and the target composition. Examples of early accelerators include x-ray tubes and Van der Graaff generators. In these electrostatic accelerators the particles are accelerated by a constant potential difference which limits the maximum kinetic energy of the particles to 1 MeV. Cyclic accelerators are capable of accelerating particles to much higher energies by the use of oscillating electromagnetic fields. This class of accelerator includes, among others, betatrons and cyclotrons. The most common example of an accelerator used in clinical practice is the linear accelerator (linac).

The components of a linac operating in photon mode are illustrated in Figure 1-1. Electrons produced by thermionic emission in the electron gun are accelerated to kinetic energies ranging from 4 to 25 MeV in an accelerating waveguide. The waveguide is an evacuated copper structure consisting of a series of resonant cavities which are powered by radiofrequency (RF) pulses at a frequency of 2856 MHz. The RF power required for a high energy accelerator is on the order of 5 MW, and is generated by either a magnetron or RF oscillator in combination with a klystron, and is transmitted to the accelerating waveguide through a uniform waveguide pressurized with a dielectric gas. A pulsed modulator produces the pulses which drive the RF power generation and electron gun. The electron beam in the accelerating waveguide is steered and focused through a series of electromagnets and made to strike a target composed of a high atomic number material such as tungsten. The photons produced in the target exit the evacuated portion of the accelerator head through a beryllium window and then pass through the beam collimation and monitoring system.

The beam collimation consists first of a primary collimator which defines the maximum field size of the radiation beam. The flattening filter attenuates the forward peaked intensity distribution of the photon beam such that the beam intensity stays relatively uniform as a function of off-axis distance. After the flattening filter the photons pass through two beam monitoring ionization chambers. The function of these chambers

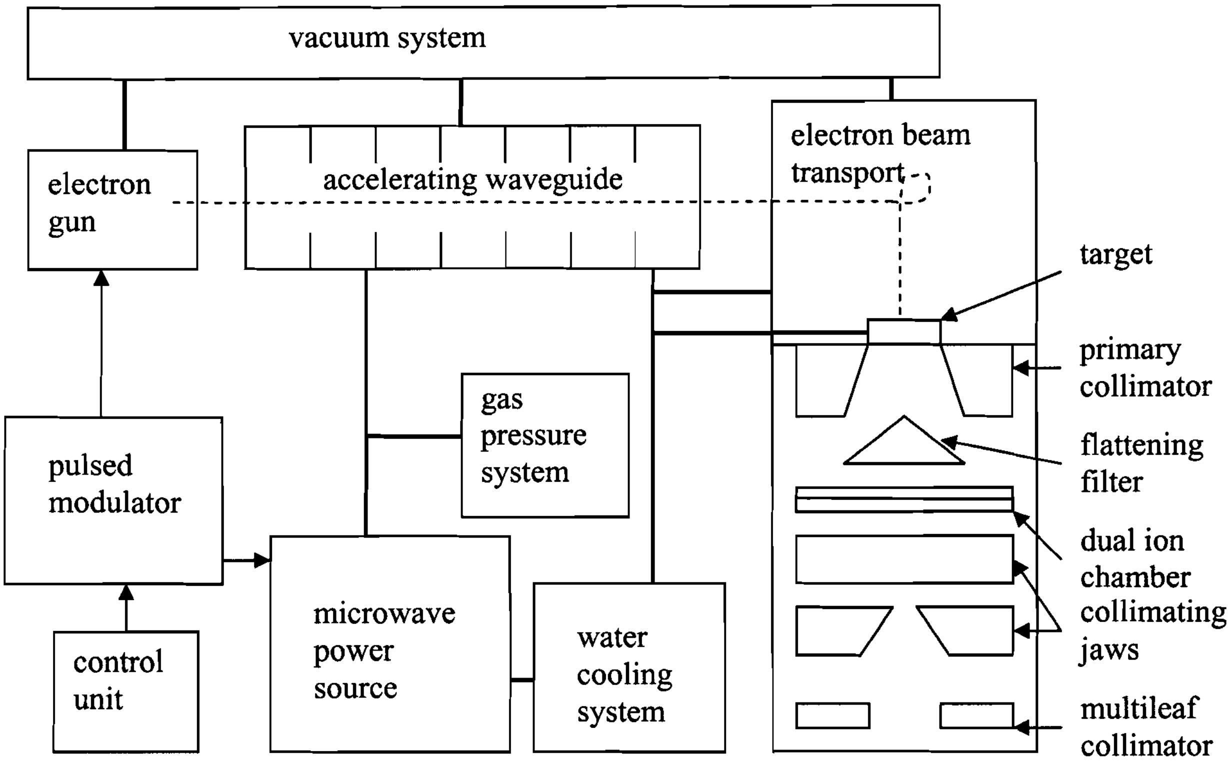

Figure 1-1: Components of a linear accelerator operating in photon mode[3].

is to monitor the radiation output so that the beam can be terminated after a specified dose has been delivered. The chamber signal is related to the absorbed dose in water at a reference point by an output calibration. Finally, the photons pass through a secondary collimation system consisting of two sets of independently moving tungsten blocks which define the radiation field size. A tertiary collimator in the form of a multi-leaf collimator may also be present.

For production of clinical electron beams, the target is retracted and the flattening filter is replaced by a set of one or two scattering foils. These foils are composed of a high atomic number material and serve to spread the width of the narrow incident electron beam intensity distribution over an area of up to 25 x 25 cm^2. As electrons are readily scattered in the air between the collimating jaws and patient, removable electron applicators are used to define the field size within a few centimeters of the patient surface.

1.3 Treatment planning

1.3.1 Treatment planning process

The treatment planning process typically consists of the following steps: target volume and sensitive structure localization, treatment field delineation and selection of beam delivery parameters, dose calculation and beam optimization, followed by treatment verification and delivery[3].

The most basic approach to treatment planning involves a determination of the location and extent of the tumour by either manual palpation or diagnostic radiographs. On the first day of treatment, skin marks are used to indicate the beam placement and to guide the choice of treatment fields. The dose delivered to the tumour is calculated using simple dosimetric functions and the assumption that the patient is uniformly composed of water. Verification of the accuracy of beam placement is carried out on the treatment unit by the acquisition of radiographs exposed for each treatment field.

The process of localization, field delineation and treatment verification can be moved away from the treatment unit by the use of a conventional simulator[4] which reproduces the geometry of a treatment unit but replaces the treatment source with a diagnostic x-ray tube or fluoroscopic unit. For this 2D treatment planning technique dose distributions are calculated for a single plane containing the tumour correcting only for the patient contour which is acquired manually through the use of a lead wire. It is important to note that the aforementioned simulation techniques are limited by the inability to visualize most tumours on conventional radiographs and fluoroscopic images. Instead, the location of the tumour is determined based on knowledge of its position in relation to bony anatomy. The advent of computed tomography (CT) made available 3-dimensional images with improved soft tissue contrast leading to improved target localization and patient contour definition for 2D planning when used in conjunction with a conventional simulator.

3-D treatment planning makes use of the CT images for delineation of target and sensitive structures in 3 dimensions and calculation of dose distributions for the entire treatment volume. Heterogeneity corrections, which correct the dose distributions based on information about the patient composition obtained from the CT data, may be applied. An integral component of the 3-D planning process is the acquisition of CT images in combination with virtual simulation software which permits reconstruction of images in any plane. The beam's eye view (BEV) projects the treatment field outline and cross-hairs over previously outlined patient structures. When overlayed on a digitally reconstructed planar radiograph (DRR) obtained from the CT data set, these DRRs replace the need for the diagnostic radiographs obtained on a conventional simulator and improves the accuracy of beam placement with respect to the target and sensitive structures.

1.3.2 Treatment plan evaluation

The goal of a radiotherapy treatment is to deliver the maximum possible dose to the tumour without exceeding the dose tolerances for the normal tissue, thereby decreasing the chances of any side effects. An increase in dose leads to an increased probability of tumour control and reduces the chance of a recurrence of the cancer. The required dosimetric accuracy of a radiotherapy treatment, as defined in ICRU Report 50[5], is that the dose delivered to the planning target volume (PTV) should be within +7 % and -5 % of the dose prescribed by the physician. This PTV contains the detectable extent of the malignancy in addition to some margins to account for subclinical disease and uncertainties in the tumour localization, organ motion and patient setup. However, in the case of both target and normal tissues, it is not only the delivered dose but also the volume of tissue receiving that dose which will determine the outcome of the treatment.

Treatment plans are commonly evaluated based on isodose distributions, dose statistics, and dose volume histograms (DVHs). DVHs are used to display volumetric information about the distribution of the dose within a particular structure and may displayed in two forms, differential and cumulative. The differential DVH is a frequency distribution of the number of voxels which receive a dose within a given dose interval, or bin, while the cumulative DVH is an integrated form of the differential DVH. Examples of ideal and typical cumulative DVHs for both target and sensitive structures are shown in Figure 1-2.

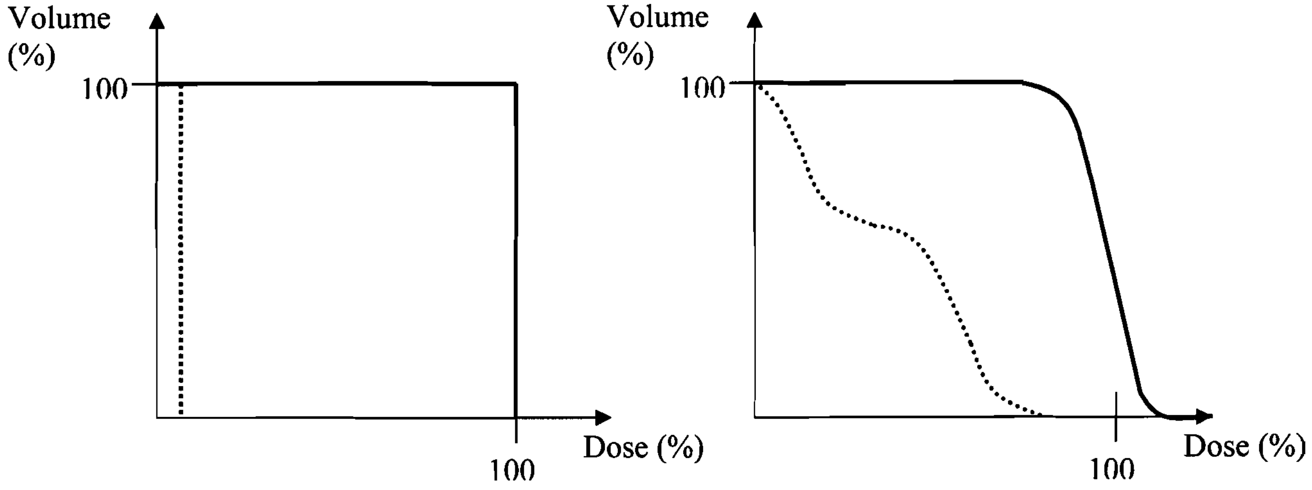

Figure 1-2: Example of a cumulative Dose Volume Histogram for a target and normal tissue for (a) ideal and (b) typical treatment. The solid line indicates target tissue and the dashed line indicates normal tissue.

1.3.3 Forward and Inverse treatment planning

Three-dimensional treatment planning is carried out in either a ‘forward’ or ‘inverse’ method. In the conventional or forward-planned technique the user selects the beam configuration based on the available patient data and on his or her experience. After the dose distribution is calculated, changes to the plan may be made to further improve the distributions. Complex intensity distributions such as those used in intensity modulated radiation therapy (IMRT) are often generated by an ‘inverse’ treatment planning system. In the inverse treatment planning process the user specifies the criteria for dose delivery to the target and critical structures, usually in the form of a dose volume histogram. The planning software then uses an iterative process of varying each element of the intensity distribution to find the optimized intensity which minimizes a cost function[6]. An example of a cost function, which is used in the CORVUS inverse treatment planning software (NOMOS Corp., Cranberry Township, PA), is the difference between the DVH for the current intensity distribution and the DVH specified by the user.

1.4 IMRT

An example of a dose distribution obtained from a simple arrangement of four uniform parallel opposed photon beams is shown in Figure 1-3a. While for certain treatment sites simple beam arrangements are adequate to provide adequately conformal and uniform coverage of the tumour, in other sites, such as the head and neck the presence of sensitive structures in the vicinity of the tumour will limit the dose that can be delivered with a simple field arrangement. The dose requirements outlined in section 1.3.2 can be met by the use of multiple beams whose apertures are conformed to the tumour by the use of shielding blocks or a multi-leaf collimator. Recently this has been extended to the use of non- uniform beam intensities to further improve beam conformity and sparing of normal tissues therefore allowing higher doses to be delivered. An example of a dose distribution obtained using this intensity-modulated radiation therapy (IMRT) technique is shown in Figure 1-3b.

IMRT can be delivered by numerous methods including the use of physical compensators, modulating the intensity of a scanned photon beam, a modulated fan beam technique (tomotherapy) and the use of multi-leaf collimators[7]. A multi-leaf collimator (MLC) is a beam collimating device consisting of independently motor driven leaf pairs. Computer controlled motion of these leaves during the delivery of radiation allows arbitrary intensity distributions to be produced. The technique of IMRT delivery with an MLC is specified as being either "step and shoot" or dynamic. In the first technique the desired intensity distribution is delivered as a series of static subfields with the radiation beam being turned off while the MLC leaves change position from one field to the next.

In a dynamic IMRT delivery the MLC leaves are continuously in motion while the beam remains on. In principle, the dynamic IMRT treatment results in a more accurate delivery of the desired intensity distribution since it is not limited to a finite number of static MLC fields and requires shorter treatment times. The leaf positions as a function of delivered dose are specified in a leaf sequence file which is generated by use of a leaf sequencing algorithm[8]. This algorithm is designed to accurately reproduce the desired dose distribution while minimizing the delivery time and accounting for any limitations on movement of the MLC leaves. Other factors which may be considered include the shape of the MLC leaves and radiation leakage between the leaves.

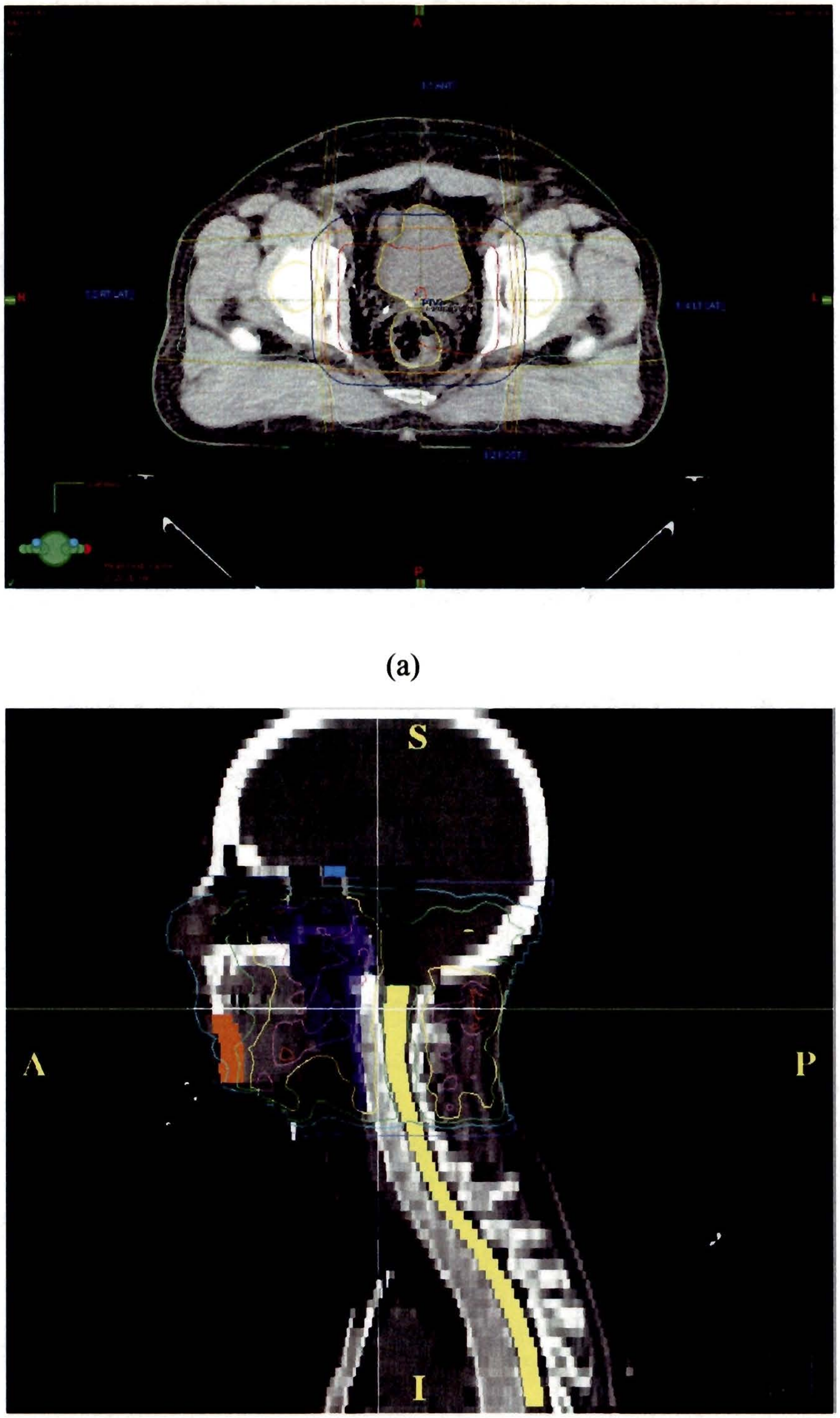

Figure 1-3: Comparison of dose distributions obtained using (a) conventional four field treatment of the prostate (b) IMRT treatment of the head and neck region consisting of 13 fields delivered at 7 different gantry angles.

1.5 The role of Monte Carlo techniques in IMRT treatment planning

The highly complex nature of IMRT brings into question issues related to the accuracy of the treatment planning and delivery. The treatment planning accuracy is determined by the accuracy of the CT data, target and sensitive structure delineation and the dose calculation algorithm. In order to obtain a 5% uncertainty in delivered dose, the dose calculation must have an uncertainty of less than 2.5%[3]. The conventional dose calculation algorithms employed in most treatment planning systems use many approximations which may compromise the accuracy of IMRT dose calculations. For example, by not fully modeling the components of the accelerator head, a conventional dose calculation algorithm does not fully account for the influence of the MLC on the incident radiation beam. In the case of an IMRT treatment, the MLC is used to define the treatment fields so the effects of MLC leakage and the tongue and groove can become significant. These contributions primarily affect the accuracy of the dose calculation in regions of low dose and therefore are of concern in the calculation of dose delivered to sensitive structures. A further concern is the correction of dose in areas of non-uniform tissue density. Conventional algorithms assume the patient to be uniformly composed of water and then apply simple correction techniques which do not account for the electron fluence perturbations which occur at the interfaces between two different media. This can lead to significant errors in the dose calculated in these regions[9].

The accuracy of IMRT dose calculations can be improved by the use of a Monte Carlo dose calculation code. A Monte Carlo code simulates radiation transport by using machine generated random numbers to sample from the probability distributions describing the particle interactions. By simulating the transport of the incident particles through the accelerator head, a Monte Carlo code explicitly accounts for the MLC leakage and effect of the leaf tongue and groove. Furthermore, a Monte Carlo code calculates the dose deposited in the medium instead of dose to water and inherently accounts for inhomogeneities. As electron transport is modeled, the fluence perturbations in these regions will also be accounted for.

The PEREGRINE Monte Carlo dose calculation code (NOMOS Corp., Cranberry Township, PA) is the first commercially available Monte Carlo code for calculation of photon beam dose distributions. The code is available in conjunction with the NOMOS

CORVUS inverse treatment planning where it is used as a verification tool for IMRT dose distributions calculated using the CORVUS dose calculation algorithm.

1.6 Thesis objective and organization

The objective of this thesis is to perform an evaluation of the dosimetric accuracy of the PEREGRINE Monte Carlo dose calculation code for 6 MV photon beams. This evaluation is performed by comparing measured dose profiles with profiles calculated by PEREGRINE in both homogeneous and heterogeneous phantoms. A model of the Varian CL21EX linear accelerator (Varian Oncology Systems, Palo Alto, CA), including the Varian 120 leaf collimator, was also built using the EGSnrc/BEAMnrc code to compare dose profiles calculated using the EGSnrc Monte Carlo code with PEREGRINE.

The second chapter provides an overview of the physical processes of interactions of ionizing radiation with matter and concepts of radiation dosimetry. The third chapter reviews the use of Monte Carlo techniques for the simulation of radiation transport and describes the Monte Carlo codes used in this study. In the fourth chapter the development and validation of a new component module for the BEAMnrc code which models the Varian 120 leaf collimator is described. The fifth chapter summarizes the detectors and measurement techniques used for measurement of dose in homogeneous and heterogeneous phantoms as well as the Monte Carlo simulations performed for the comparison. The results of this evaluation are described in Chapter 6 and finally conclusions and a summary of future work is provided in Chapter 7.

1.7 References

[1] National Cancer Institute of Canada, "Canadian Cancer Statistics 2002," Toronto (2002).

[2] E. Hall, *Radiobiology for the Radiologist* (J.R. Lippincott Co., Philadelphia, 1994).

[3] J. Van Dyk, *The Modern Technology of Radiation Oncology: A Compendium for Medical Physicists and Radiation Oncologists* (Medical Physics Publishing, Madison, Wisconsin, 1999).

[4] F.M. Khan and R.A. Potish, *Treatment Planning in Radiation Oncology* (William and Wilkins, Baltimore, 1998).

[5] ICRU, "Prescribing, Recording and Reporting Photon Beam Therapy," ICRU Report No.50, International Commission on Radiation Units and Measurements, Bethesda (1993).

[6] S. Webb, "Optimisation of conformal radiotherapy dose distributions by simulated annealing," Phys. Med. Biol. **34**, 1349-1370 (1989).

[7] IMRT Collaborative Working Group, "Intensity-Modulated Radiotherapy: Current Status and Issues of Interest," Int. J. Radiation Oncology Biol. Phys. **51,** 880-914 (2001).

[8] T.R. Bortfeld, D.L. Kahler, T.W. Waldron and A.L. Boyer, "X-ray field compensation with multileaf collimators," Int. J. Radiation Oncology Biol. Phys. **28**, 723-730 (1994).

[9] M.R. Arnfield, C. Hartmann-Siantar, L.Cox and R. Mohan, "The impact of electron transport on the accuracy of computed dose," Med. Phys. **27**, 1266-1274 (2000).

Chapter 2:

Physics of Radiation Therapy

2.1 Physics of radiation therapy

2.1.1 Photon interactions

Photons are defined as an indirectly ionizing form of radiation. This refers to the fact that photons transfer energy to electrons and positrons which then produce ionizations in the medium. The probability of a photon interacting in a medium is described by an exponential attenuation coefficient. The number of photons *N(x)* transmitted through a slab of material of thickness x is calculated as follows:

$$N(x) = N_0 e^{-\mu x}, \tag{2.1}$$

where N_0 is the initial number of photons incident on the slab and μ is sum of the linear attenuation coefficients for all the physical processes involved. Photon interactions occurring in the energy range of radiation therapy include photoelectric interactions, Rayleigh scattering, Compton scattering, pair and triplet production, and photo-nuclear interactions. The relative predominance of three of these interactions as a function of photon energy and atomic number of the medium is shown in Figure 2-1.

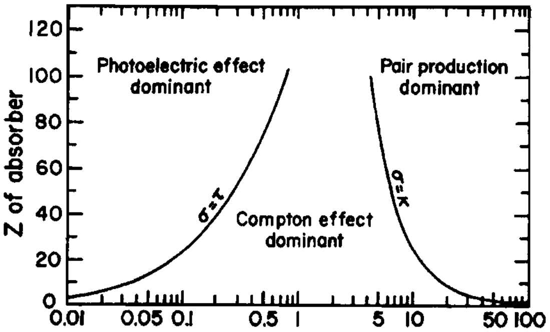

Figure 2-1: Relative predominance of three types of photon interactions occurring in the energy range of radiation therapy[1].

At the low energy range of radiation therapy the photoelectric effect is the predominant type of interaction. The incident photon collides with an atom and transfers all its energy to a bound electron which is ejected with a kinetic energy corresponding to the difference of the incident photon energy and the electron's binding energy. The resulting vacancy in the atomic shell structure may then be filled by an electron from a higher energy state in a process termed atomic relaxation. The energy lost by the electron as it moves to a lower energy state may be emitted as a fluorescent photon or an Auger electron. These fluorescent photons are also called "characteristic x-rays" as they are emitted with discrete energies which are determined by the shell structure of the atom. In the production of Auger electrons, the energy is transferred to a higher shell electron and the relaxation process is continued until all resulting vacancies are moved to the outer shell. The probability of a photoelectric interaction varies with photon energy and atomic number as $(Z/h\nu)^3$. The probability of interaction is highest when the photon energy is slightly higher than the binding energy of the electron and this is manifested graphically as sharp peaks in the attenuation coefficients which correspond to the binding energies of the various atomic shells.

Rayleigh scattering occurs when a photon is elastically scattered by an atom. There is no transfer of energy to the medium and the photon is predominantly scattered through small angles. The probability of interaction varies with photon energy and atomic energy as $Z/(h\nu)^2$.

The predominant photon interaction process in tissue at megavoltage photon energies is Compton scattering. In this case an incident photon transfers a portion of its energy to an atomic electron resulting in a scattered photon and an energetic electron. The probability of interaction is independent of the atomic number and decreases with increasing incident photon energy. The cross-section is calculated using the Klein-Nishina approximation of the atomic electron being free, however at low energies a correction is applied to account for the binding energy of the electron.

Pair production may occur when the incident photon energy is greater or equal to 1.022 MeV. The photon is absorbed by the nucleus of the atom and an electron-positron pair is produced. For incident photon energies exceeding $4m_0c^2$ triplet production may occur. In this case the photon interacts with an atomic electron resulting in the ejection of two electrons and a positron. The probability of pair and triplet interactions varies increases with energy and atomic number.

Photo-nuclear disintegration occurs when a photon with energy greater than 10 MeV interacts with the nucleus resulting in the emission of a photoneutron. This interaction is mainly of interest in radiation protection issues for high energy linear accelerators.

The total mass attenuation coefficient for different media as a function of photon energy is shown in Figure 2-2.

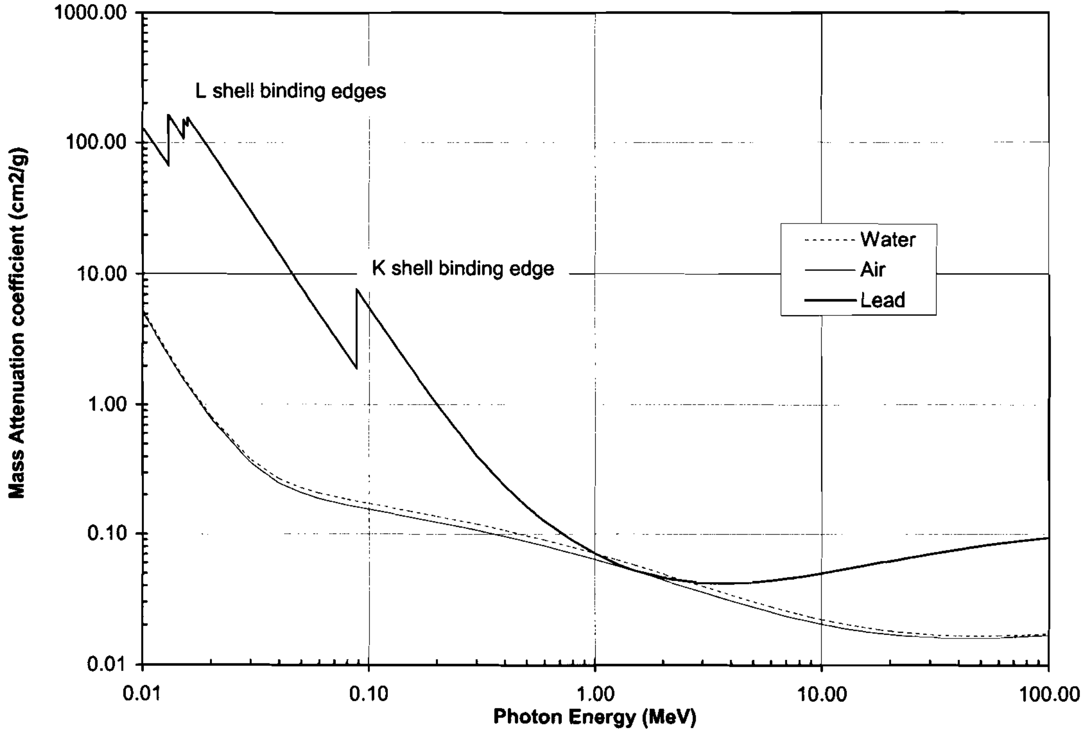

Figure 2-2: Total mass attenuation coefficient in lead, water and air as a function of incident photon energy (data obtained from NIST tables[2]).

2.1.2 Electron Interactions

Electrons undergo two types of interaction within a medium: collisional and radiative. The type of interaction is determined by the distance between the electron's path and the atomic nucleus as illustrated in Figure 2-3:

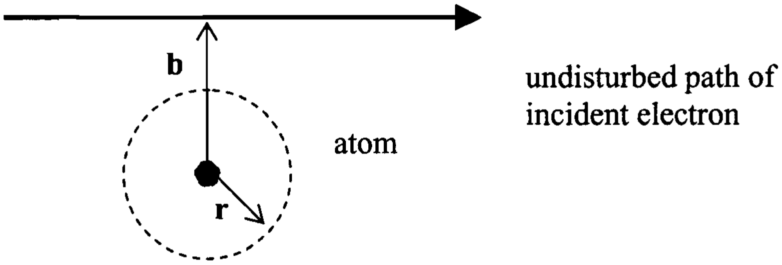

Figure 2-3: Model of electron interacting with an atom; r is the atomic radius and b is defined as the impact parameter.

where b is defined as the impact parameter and r is the atomic radius. When the impact parameter is much larger than the atomic radius, the electron will transfer a small amount of energy to the outer atomic electrons. These "soft collisions" account for half of the electron interactions in a medium. If the impact parameter is approximately equal to the atomic radius the incident electron may transfer as much as 50% of its kinetic energy in a head-on collision with an atomic electron. These "hard collisions" are much less frequent but result in the ejection of a high energy electron called a delta ray or "knock-on" electron. If the incident electron passes within the atomic radius it will undergo an interaction with the nucleus resulting in either elastic scattering of the electron or production of an x-ray photon. The latter radiative process is termed bremsstrahlung and is the method by which photon beams are generated in x-ray tubes and linear accelerators.

A fourth type of electron interaction, positron annihilation, exists in which a positron and electron annihilate to produce two 0.511 MeV photons which are approximately co-linear depending on the kinetic energy of the incident particles.

2.1.3 Fluence and Kerma

The particle fluence Φ is defined as the number of particles dN crossing through a surface of area dA:

$$\Phi = \frac{dN}{dA} \quad . \tag{2.2}$$

Similarly, the energy fluence Ψ is defined as the total kinetic energy of the particles passing through a surface dA:

$$\Psi = \frac{dN \cdot h\nu}{dA} , \tag{2.3}$$

where $h\nu$ is the photon energy. As mentioned previously, deposition of energy by photons is a two step process. The first step involves the transfer of energy from the incident photon to electrons in the medium. The energy transferred per unit mass at a point in the medium is defined as the kerma (Kinetic Energy Released per unit MAss). The unit of kerma is the Gray (Gy) which is equivalent to one Joule per kilogram. The total kerma is the sum of the energy transferred by a photon of energy $h\nu$ which results in collissional and radiative electron interactions and is calculated as follows:

$$K = \Phi\left(\frac{\mu_{tr}}{\rho}\right)h\nu = K_{coll} + K_{rad} , \tag{2.4}$$

$$\text{where } \left(\frac{\mu_{tr}}{\rho}\right) = \left(\frac{\mu}{\rho}\right)\frac{E_{tr}}{h\nu},$$

and ρ is the physical density, $\left(\mu/\rho\right)$ is the mass attenuation coefficient and E_{tr} is the average energy transferred which is calculated from the sum of the energy transferred to electrons by each type of photon interaction. The collisional kerma K_{coll} is calculated from the mass-energy absorption coefficient μ_{ab}/ρ as follows:

$$K_{coll} = \Phi\left(\frac{\mu_{ab}}{\rho}\right)h\nu, \tag{2.5}$$

$$\text{where } \mu_{ab} = \mu_{tr}(1-g),$$

and the bremsstrahlung fraction g is the fraction of transferred energy lost to radiative interactions.

2.1.4 Stopping Power

The stopping power S is defined as the amount of kinetic energy T lost by a charged particle per unit path length x through radiative and collisional interactions:

$$S = \frac{dT}{dx} = S_{col} + S_{rad} . \tag{2.6}$$

The formula for the mass collisional stopping power of an electron is as follows:

$$\frac{S_{col}}{\rho} = \frac{2\pi r_e^2}{\beta^2}\frac{N_A Z}{A}\left(\ln\left(T/I \right)^2 + \ln(1+\tau/2) + F^{-}(\tau) - \delta \right), \tag{2.7}$$

$$\text{where } F^{-}(\tau) = \left(1-\beta^2\right)\left[1 + \tau^2/8 - (2\tau+1)\ln 2\right] \text{ and } \tau = T/m_0c^2,$$

and N_A is Avogadro's number, A is the atomic mass number, r_e is the classical radius of the electron and β is related to the velocity of the electron. The collisional stopping power is proportional to the number of electrons per unit mass in the medium and inversely proportional to the electron kinetic energy. The density effect parameter δ accounts for the decrease in stopping power with increasing medium density. Polarization of the medium by the path of the incident electron causes the charge of distant atomic electrons to be screened thereby reducing the stopping power. This polarization effect is dependent on the density of the medium. The formula for the mass radiative stopping power of an electron is:

$$\frac{S_{rad}}{\rho} = \frac{1}{137}\left(\frac{e^2}{m_0c^2}\right)^2 \frac{N_A Z^2}{A}(T + m_0c^2)\overline{B}_r, \tag{2.8}$$

where $\overline{B}_r$ is a function of Z and T. The radiative stopping power varies strongly on the atomic number of the medium and also increases with increasing kinetic energy. The collisional and radiative mass stopping powers of an electron in water and lead are shown in Figure 2-4.

The above definition of stopping power is termed the unrestricted stopping power. In some cases we are interested only in the energy deposited within a given distance of the electron track. The high energy delta electrons produced in hard collisions deposit their energy some distance away from the particle track and therefore must be excluded from the stopping power determination in this case. For the calculation of the restricted stopping power L_Δ a threshold Δ is specified for the energy transferred. The choice of the threshold energy depends on the dimensions of the volume of interest. The restricted stopping power is therefore always smaller than the unrestricted stopping power.

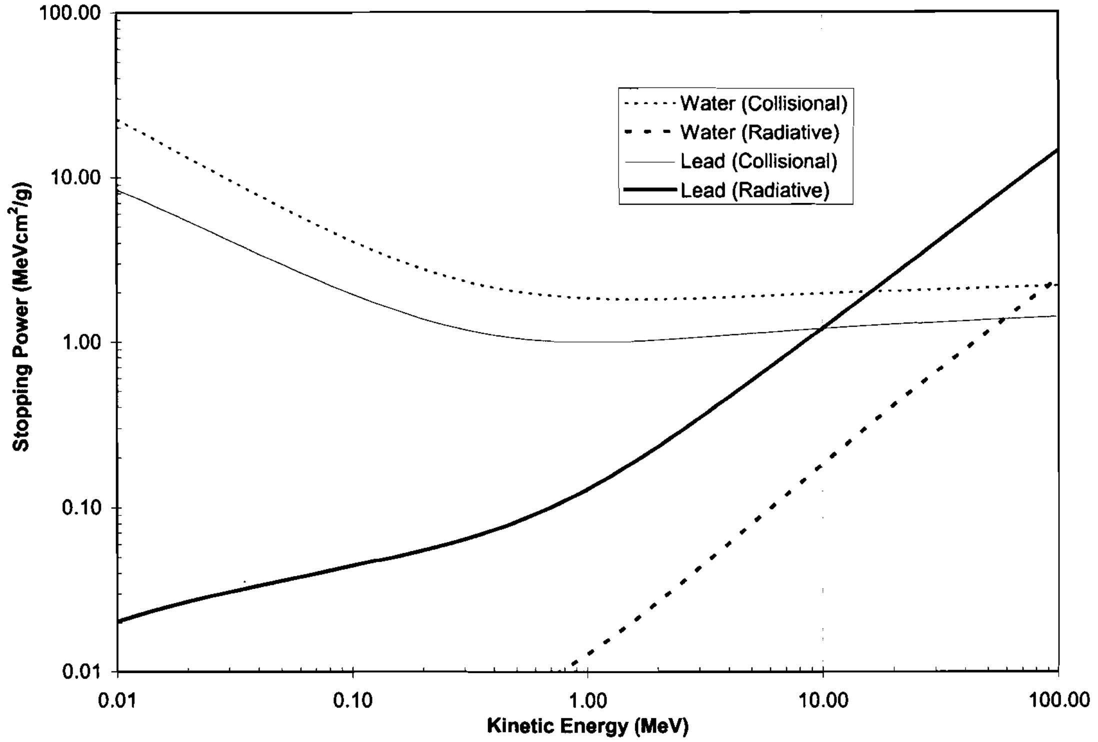

Figure 2-4: Radiative and Collisional stopping power in lead and water (data obtained from NIST tables[2]).

2.1.5 Absorbed dose

The absorbed dose is defined as the net energy deposited at a point per unit mass of material. The unit of dose is the Gray, or Joules per kilogram. The absorbed dose can be determined from the collisional kerma at a point where charged particle equilibrium (CPE) exists, as outlined in the following section.

2.1.6 Charged particle equilibrium

The concept of charged particle equilibrium (CPE) is integral to the determination of the absorbed dose in a medium. The CPE condition is fulfilled when the number of charged particles entering and leaving a volume of interest are equal. Under these conditions the absorbed dose equals the collisional kerma at the same point. The concept of CPE for a photon beam incident on a medium is illustrated in Figure 2-5.

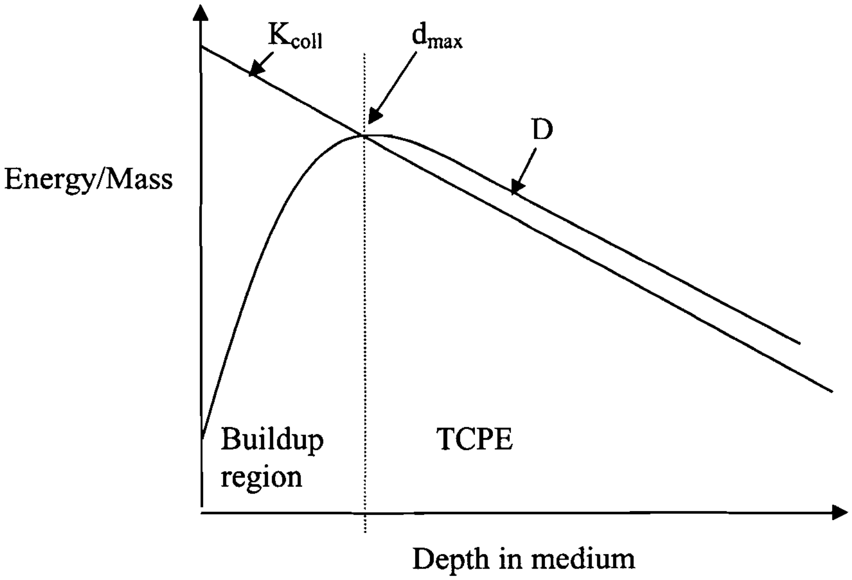

Figure 2-5: Energy deposition by photons in a medium illustrating the concept of CPE.

The incident photons interact in the medium releasing electrons and thereby increasing the electron fluence. This leads to an initial increase in the absorbed dose. At the same time the collisional kerma decreases as a result of exponential attenuation of incident photons. In this initial buildup region there are more electrons leaving a given volume than entering it. At a characteristic depth d_{max}, corresponding to a maximum in the absorbed dose, charged particle equilibrium is reached and the dose and K_{coll} are equal. Beyond this point the effect of photon attenuation dominates and a state of transient charged particle equilibrium (TCPE) exists and the dose is written as follows:

$$D = \beta K_{coll}, \tag{2.9}$$

where $\beta > 1$ and accounts for the fact that the energy transferred by a photon is deposited by electrons downstream from the site of the photon interaction.

2.1.7 Cavity theory

The Bragg-Gray cavity theory[3,4,5] relates the dose deposited in a cavity inside a medium to the dose at the same point in the absence of the cavity. This can be applied to the measurement of absorbed dose in a medium where the detector composition is different from that of the medium. The concept of the Bragg-Gray cavity in a medium is illustrated in Figure 2-6.

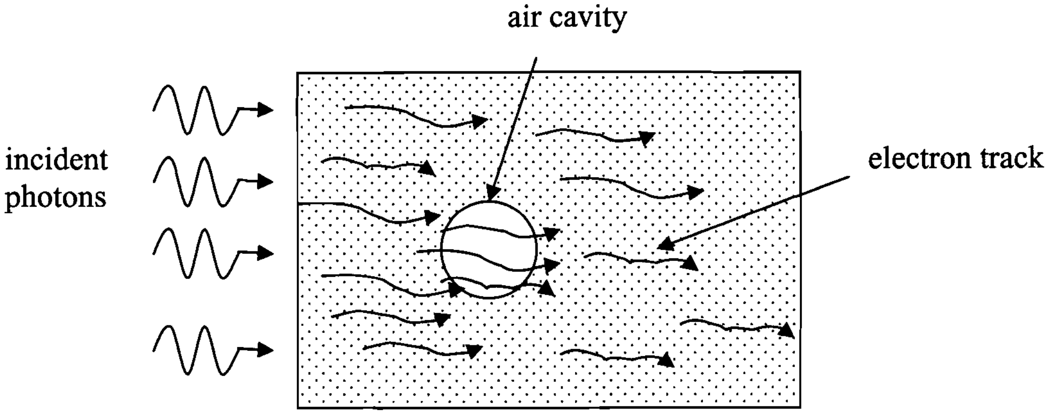

Figure 2-6: Illustration of a Bragg-Gray cavity within a medium showing electron tracks crossing the cavity[6].

To satisfy the conditions for a Bragg-Gray cavity: (1) charged particle equilibrium must exist within the medium, (2) the cavity must be small compared to the range of the charged particles which cross it and (3) the energy deposited in the cavity must come solely from these charged particles. The absorbed dose deposited by electrons is a product of the electron fluence and collisional stopping power in the medium.

$$D = \left(\frac{S_{coll}}{\rho}\right)\Phi \quad . \tag{2.10}$$

If conditions (1) and (2) are met then the electron fluence is constant across the cavity and the dose in the medium can be related to the cavity dose as follows:

$$D_{cav} = D_{med}\left(\frac{\bar{S}}{\rho}\right)_{med}^{cav} \quad . \tag{2.11}$$

where $\left(\frac{\bar{S}}{\rho}\right)_{med}^{cav}$ is the ratio of the stopping powers averaged over the energy spectrum in each of the media.

The Spencer-Attix cavity theory[7] is an extension of the Bragg-Gray cavity which accounts for delta electrons produced in the medium which may not have sufficient energy to cross the cavity. A threshold Δ is specified which is the energy required for an electron to cross the cavity. Restricted stopping powers are used to limit the energy transferred such that the electrons have sufficient kinetic energy to cross the cavity.

$$D_{cav} = D_{med}\left(\frac{\overline{L}_{\Delta}}{\rho}\right)_{med}^{cav} . \tag{2.12}$$

A further consideration is the case of a larger cavity where the electron range is shorter than the cavity size so that photons effectively deposit their dose directly in the cavity in addition to the dose deposited by electrons. In this case the Burlin cavity theory[8] may be applied which uses a cavity size dependent factor d to weight the contributions of the photons and electrons to the cavity dose.

$$D_{cav} = D_{med}\left(d\left(\frac{\overline{L}_{\Delta}}{\rho}\right)_{med}^{cav} + (1-d)\left(\frac{\overline{\mu}_{ab}}{\rho}\right)_{med}^{cav} \right) . \tag{2.13}$$

2.2 Dosimetry of photon beams

2.2.1 Introduction

A dosimeter is a device which converts the dose deposited in its medium to a measurable signal. Dosimeters are classified as being either absolute or relative. An absolute dosimeter is one in which the dose may be determined without the need for a calibration measurement in an ionizing radiation field. An example of an absolute dosimeter is the calorimeter where the energy deposited is related to the measured rise in temperature by the specific heat capacity of the medium. Relative dosimeters require a measurement of the signal for a known dose in order to determine a calibration factor. Examples of relative dosimeters include ionization chambers, thermoluminescent dosimeters (TLDs), film, Fricke dosimeters and diodes.

An ideal dosimeter has a stable, linear response to dose and does not introduce any perturbation of the dose in the medium by its presence. This latter criterion requires careful choice of the detector composition such that it responds in similar fashion to the incident radiation as the medium in which the dose is being measured.

2.2.2 Ionization chambers

The ionization chamber is the most commonly used dosimeter in radiotherapy. There are two main types of ion chamber designs: cylindrical and parallel-plate. A diagram of a parallel-plate ionization chamber is shown in Figure 2-7.

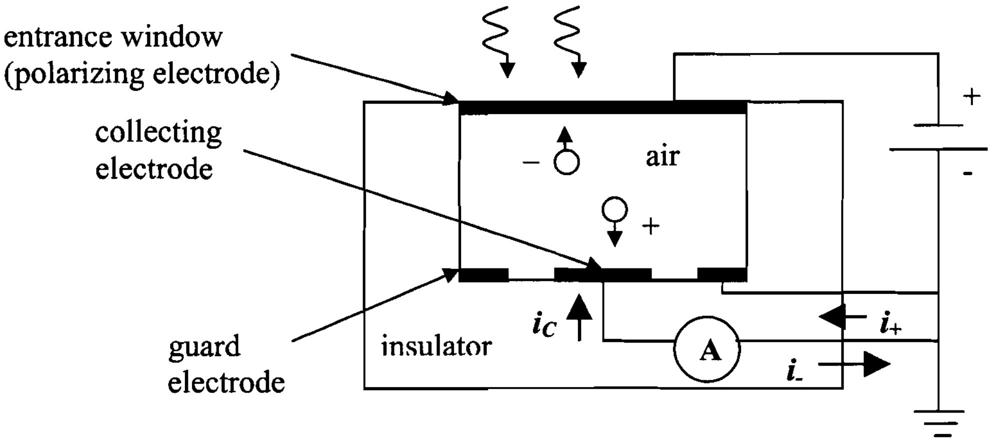

Figure 2-7: Diagram of a parallel-plate ionization chamber.

Incident photons release electrons in the medium which ionize the air molecules inside the chamber cavity. A constant potential difference is applied between the polarizing and collecting electrodes which causes ions to move to the electrodes. Depending on their charge, ions either remove or add electrons to the measuring electrode and therefore cause a current (i_+ or i_-) to flow. The chamber is connected to an electrometer which supplies the polarizing voltage and permits either the direct measurement of current or integrated charge. The charge Q released in the chamber volume by the incident radiation is related to the dose deposited in the chamber air cavity D_{gas} by the following relationship:

$$D_{gas} = \left(\frac{Q}{m_{gas}}\right)\left(\frac{W}{e}\right)_{gas}, \qquad (2.14)$$

where m_{gas} is the mass of the sensitive volume and $\left(\frac{W}{e}\right)_{air}$ = 33.97 eV/ion pair is the mean energy required to release one ion pair in air..

The purpose of the guard electrode is to collect any leakage currents due to contamination of the insulating material. The measured signal increases with increasing voltage until a saturation point is reached where all ions are collected. The polarizing voltage is chosen such that the ion chamber operates near or at this saturation region. The signal may also vary with the sign of the polarizing voltage. A small signal i_C, misleadingly termed the "Compton" current, is induced by interactions of photons and electrons in the collecting electrode and cable. When the chamber is operated under a positive bias the measured signal $I(+V)$ is the sum Compton current and signal due to collection of positive ions i_+. When the bias is reversed the signal $I(-V)$ will be the signal due to collection of negative ions i_- minus the Compton current. In order to remove the effect of the Compton current it is necessary to take the average of the measured signal under both polarities.

$$\begin{aligned} I(+V) &= i_+ + i_C \\ I(-V) &= i_i - i_C \\ i_+ = i_- &= \frac{1}{2}\left(I(+V) + I(-V)\right) \end{aligned} \quad . \tag{2.15}$$

2.2.3 Film dosimetry

Radiographic film, in addition to its use in diagnostic radiology, has also found applications in radiation dosimetry due to its high resolution and convenience for measurement of two-dimensional dose distributions. The composition of a typical double-emulsion film is shown in Figure 2-8. The emulsion layer is composed of flat

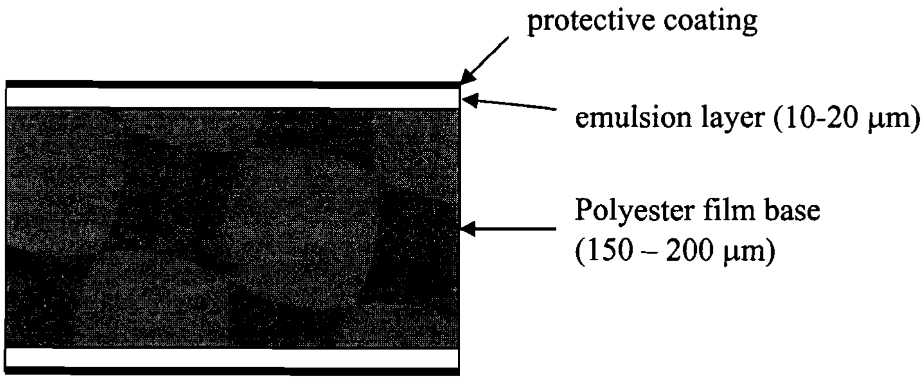

Figure 2-8: Composition of a double-emulsion radiographic film[9] *showing the 10 - 20 μm thick radiation sensitive emulsion layer deposited on either side of a 150 – 200 μm polyester base.*

silver halide crystals, typically 1 μm in dimension, suspended in a gelatin matrix. These silver iodobromide crystals respond to ionizing radiation by causing the film to become opaque. Defects in the crystals allow silver ions to move freely within the crystal structure. Incident photons ionize bromine atoms in the crystal to produce free electrons which then neutralize the free silver ions causing deposition of a silver atom. Accumulation of these silver atoms is responsible for darkening of the film and formation of the latent image. Generally the amount of deposited silver atoms is proportional to the deposited dose. After it has been exposed, the film is subjected to a chemical developing process which amplifies the size of the silver grains and fixes them on the film. Unlike the ionization chamber, film can only measure the total dose deposited and gives no information regarding the dose rate. Film is therefore defined to be an integrating dosimeter.

The absorbed dose is determined by measuring the optical density (OD) of the film with a densitometer consisting of a light source and photosensor. The measured relative transmittance of the film is converted to *OD* by the following relationship:

$$OD = \log_{10}\left({}^{L_0}\!/_{L_t} \right), \tag{2.16}$$

where L_0 and L_t are the incident and transmitted light intensity, respectively. Measurements of optical density for a series of known doses are used to construct a characteristic response curve, which can then be used to determine the dose for any measured *OD*. An example of a characteristic curve is shown in Figure 2-9. The film response is characterized by a linear region in which the optical density is a linear function of absorbed dose. At very high doses the film becomes saturated and the optical density is unchanged with increasing dose. All the latent centres in the silver halide crystals become neutralized so further exposure cannot cause deposition of more silver grains. Similarly, at very low doses which are insufficient to deposit a detectable number of silver grains, the optical density is constant at a level determined by exposure of the film by ambient light and processing, defined as fogging, and the transmittance of the film base layer.

Radiochromic film is a relatively new type of film dosimeter which changes color when exposed to ionizing radiation. This film does not require any chemical processing

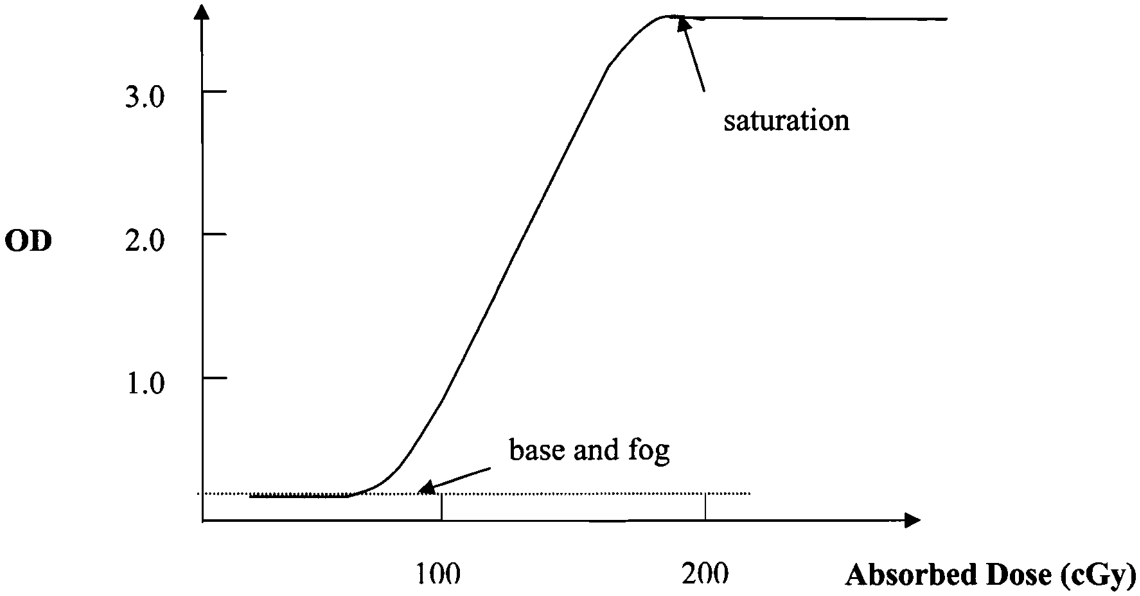

Figure 2-9: Example of a characteristic film response curve. The response curve consists of a linear portion in which the optical density is linear function of the dose deposited in the film. At very high doses the optical density is unchanged with increasing dose and the film is said to be 'saturated'. Below a threshold dose the optical density of the film is constant at a level determined by the transmittance of the film base layer (base) and darkening of the film sensitive layer by exposure to ambient light and processing conditions (fog).

and has an effective atomic number similar to that of tissue resulting a relatively energy independent response compared to that of radiographic film[10].

2.2.4 Thermoluminescent dosimeters

Thermoluminescent dosimeters (TLDs) are a type of integrating dosimeter which store the energy deposited by ionizing radiation within their crystal structure and re-release this energy in the form of visible light upon heating. Available as a powder or as small rods and chips, TLDs are manufactured by adding small amounts of impurities to pure phosphor crystals which results in defects in the crystal structure. As shown in Figure 2-10, incident radiation excites electrons from the valence band to the conduction band where they can move freely and at the same time releases a free moving hole in the valence band. In a perfect crystal structure the hole and electron would recombine and release a photon. However in this case, intermediate energy states in the forbidden band introduced by the impurities act as electron traps. When the crystal is heated a trapped electron acquires sufficient energy to move to the conduction band where it will recombine with a trapped hole at a luminescent centre causing the release of a visible light photon.

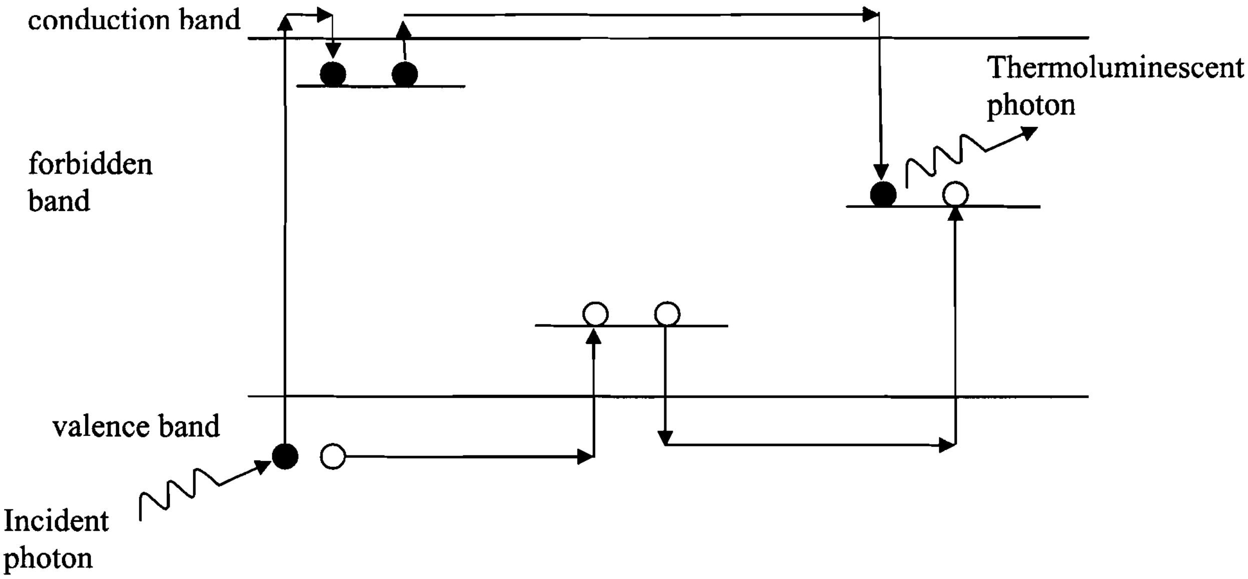

Figure 2-10: Model of thermoluminescence[11].

This thermoluminescent signal is measured using a reader which consists of a heating filament, a conducting pan for ensuring uniform heating of the TLD and a photomultiplier tube (PMT) which converts the emitted visible light photons to an electrical charge. A plot of the TLD signal as a function of crystal temperature is called the characteristic glow curve. An example of a glow curve for lithium fluoride is shown in Figure 2-11. The glow curve consists of a series of temperature dependent peaks which are associated with electron traps of different energy levels. The dose is measured from either the height of a particular peak or by integrating the area under the glow curve. The low temperature peaks are associated with electrons in low energy traps which acquire sufficient energy at room temperature to recombine within a few seconds to days. Due to the short decay time of these low temperature peaks the TLD signal is strongly dependent on the time which elapses between the exposure and readout. The readout of TLDs is often carried out in a nitrogen atmosphere to reduce the occurrence of non-radiation induced thermoluminescence (NRI-TL). These spurious signals lead to a peak at a temperature above that of the main thermoluminescence peak and are thought to be mechanically induced at the surface of the TLD[12].

An annealing procedure may be used to remove the low energy peaks by either waiting a day before readout or heating the TLD to approximately 100 °C for 10 minutes. Similarly, by heating the crystal to 400 °C for at least 1 hour followed by an extensive cooling period all electrons and holes are removed from the trapping centers effectively 'erasing' the stored dose.

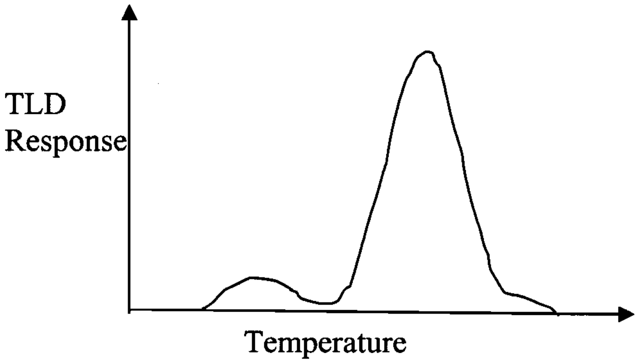

Figure 2-11: Characteristic glow curve for lithium fluoride.

2.3 Photon beam dose calculation

2.3.1 Basic dosimetric functions

The basic geometry of an external beam radiotherapy treatment is shown in Figure 2-12. A point source of radiation in air placed at a distance f from the patient surface. The projected field size of the incident radiation beam on the surface is A. Many dosimetric functions exist which relate the dose at a given point in the phantom to the dose at a reference point. Examples of these functions include the percentage depth dose (PDD), off-axis ratio (OAR) and relative dose factor (RDF).

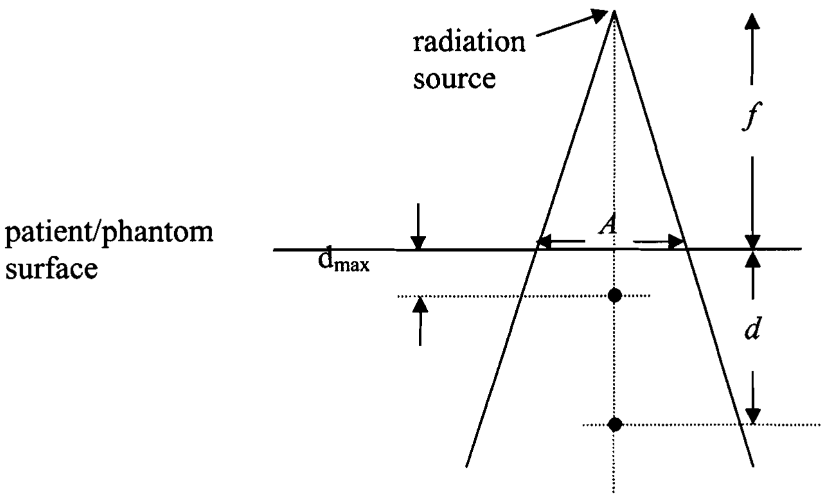

Figure 2-12: Basic geometry of external beam radiotherapy.

The percentage depth dose relates the central axis dose at a depth *d* to the dose at the depth of maximum dose.

$$PDD(d,A,f,hv) = 100 \times \frac{D(d,A,f,hv)}{D(d_{\max},A,f,hv)} \quad . \tag{2.17}$$

The off-axis ratio relates the dose at a depth *d* and distance *x* from the central axis to the dose at the same depth on the central axis.

$$OAR(x) = \frac{D(x)}{D_{CAX}} \quad . \tag{2.18}$$

The relative dose factor, also referred to as the output factor, relates the dose for a field size *A* at the depth of maximum dose to the dose at the same depth for a reference field size of 10x10 cm^2.

$$RDF(A) = \frac{D(d_{\max},A)}{D(d_{\max},10)} \quad . \tag{2.19}$$

2.3.2 3-Dimensional pencil beam dose calculation algorithm

While the dosimetric functions mentioned above can be used to determine the dose at any point within a flat, homogeneous phantom they are inadequate for determining the three-dimensional dose distribution within a patient. Information about the patient contours and composition available from CT images has prompted the development of more sophisticated 3-D dose calculation algorithms, an example of which is the finite-size pencil beam (FSPB) model[13] implemented in the CORVUS Inverse Treatment Planning software (NOMOS Corp, Cranberry Township, PA). Dose calculation algorithms are classified as either model-based or correction-based with the FSPB model belonging to the former group[14].

The principle of the FSPB model is to divide the incident beam into a set of finite-sized square pencil beams. The dose at a point is then calculated as the sum of the individual contributions from each of these pencil beams[15]:

$$D(d,x,y) = MU \cdot \sum_{j-1}^{n_j} F(x_j,y_j)T(x_j,y_j)FSPB(d,x-x_j,y-y_j) \ , \qquad (2.20)$$

where MU is the total number of monitor units delivered and $F(x_j,y_j)$ and $T(x_j,y_j)$ are functions describing the incident fluence distribution and transmission through beam modifiers such as a wedge or multi-leaf collimator. The FSPB is derived from the convolution of the pencil beam dose deposition kernel and the source kernel. The dose kernel describes the primary and scatter dose deposited by the pencil beam. The primary dose kernel has been analytically determined[16] to have the form:

$$K_P(d,r) = P_\lambda(d)e^{-\mu d} \cdot \frac{\gamma e^{-\gamma r}}{F(r)} \ , \qquad (2.21)$$

where $P_\lambda(d)$ is the primary equilibrium dose due to the first interactions of primary photons and $F(r)$ is a function accounting for the shape of the incident fluence profile. $P_\lambda(d)$ and μ are determined by fitting zero field size dose extrapolated from measurements to the following relationship:

$$P(d) = P_\lambda e^{-\mu d} , \qquad (2.22)$$

and λ is derived from an analytical relationship with μ. The scatter dose kernel is derived from the difference between the measured total dose and calculated primary dose as a function of depth and radius. The source kernel describes the distribution of primary photons produced in the target and the secondary photons which are scattered from various components in the accelerator head. Based on measurements the source kernel has been described by a sum of two Gaussian functions[17]:

$$H(r) = a_1 e^{-b_1 r^2} + a_2 e^{-b_2 r^2}, \tag{2.23}$$

where the parameters a_1, a_2, b_1 and b_2 are chosen to fit calculated penumbra to measured data.

To calculate the dose in regions of non-uniform density the effective pathlength correction method[18] is employed. The depth of the point at which the dose is calculated is scaled by the integral of the relative electron densities along the incident pencil beam and the pencil beam contribution FSPB($d,x-x_j,y-y_j$) in Equation (2.20) is replaced by FSPB($l_{eff},x-x_j,y-y_j$) where the effective depth l_{eff} is calculated as follows:

$$l_{eff} = \int_0^l \frac{\rho_e(l)}{\rho_e^{H_2O}} dl \ . \tag{2.24}$$

The relative electron density ρ_e is obtained from the CT data via a calibration curve relating the CT number to relative electron density. It is important to note that this correction scales the FSPB only in depth and no lateral scaling is applied to account for the lateral spread of the pencil beam.

2.9 References

[1] F.H. Attix, *Introduction to Radiological Physics and Radiation Dosimetry*, (John Wiley & Sons, New York, 1986).

[2] National Institute of Science and Technology, Gaithersburg, MD.

[3] W.H. Bragg, *Studies in radioactivity*, (MacMillan and Co., London, 1912).

[4] L.H. Gray, "The absorption of penetrating radiation," Proc. Roy. Soc. **A122**, 647-668 (1929).

[5] L.H. Gray, "An ionization method for the absolute measurement of y-ray energy," Proc. Roy. Soc. **A156**, 578-596 (1936).

[6] H.E. Johns and J.R. Cunningham, *The Physics of Radiology*, (Charles C. Thomas, Springfield, 1983).

[7] L.V. Spencer and F.H. Attix, "A theory of cavity ionization," Radiation Res. **3**, 239-254 (1955).

[8] T.E. Burlin, "A general cavity theory of ionization," Br. J. Radiology **39**, 727-734 (1966).

[9] A.B. Wolbarst, *Physics of Radiology*, (Medical Physics Publishing, Wisconsin, 1993).

[10] AAPM Task Group 55, "Radiochromic film dosimetry: Recommendations of AAPM Radiation Therapy Task Group 55," Med. Phys. **25**, 2093-2115 (1998).

[11] A.F. McKinlay, *Thermoluminescence Dosimetry*, (Medical Physics Handbooks, Adam Hilger Ltd. Bristol, 1981).

[12] R. Cameron, N. Suntharalingam and G.N. Kenney, *Thermoluminescent Dosimetry*, (University of Wisconsin Press, Madison, 1968).

[13] J.D. Bourland and E.L. Chaney, "A finite-size pencil beam model of photon dose calculations in three dimensions," Med. Phys. **19**, 1401-1411 (1992).

[14] T.R. Mackie and J.R. Palta, "Teletherapy: Present and Future," *Proceedings of the AAPM 1996 Summer School* (American Association of Physicists in Medicine, College Park, 1996).

[15] NOMOS, "CORVUS Beam Utilities 4.1 User Manual," NOMOS Corporation, Cranberry Township, PA , 2002.

[16] P.S. Nizin and X.S. Chang, "Primary dose in photon beams with lateral electronic disequilibrium," Med. Phys. **18**, 744-748 (1991).

[17] D.A. Jaffray and J.J. Battista, "X-ray sources of medical linear accelerators: Focal and extra-focal radiation," Med. Phys. **20**, 1417-1427 (1993).

[18] J.E. O'Connor, "The variation of scattered x-rays with density in an irradiated body," Phys. Med. Biol. **1**, 352-369 (1957).

Chapter 3:

Monte Carlo Techniques

3.1 Monte Carlo techniques for radiation transport

Monte Carlo techniques are a mathematical approach to solving problems governed by probability distribution functions. The advantage of using these techniques is that they may be applied to problems for which analytical or experimental solutions are not determinable. A basic outline of the Monte Carlo method is illustrated in Figure 3-1. A random number is used to sample an event based on the probability distribution function describing the physical process being investigated. The result of this sampled event is scored and the process is repeated many times to obtain information about the average value and statistical uncertainty of the result.

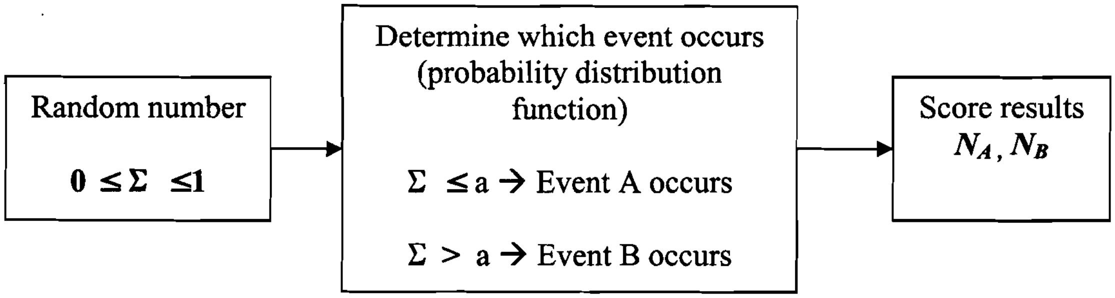

Figure 3-1: Basic outline of the Monte Carlo method. A random number Σ is used to sample an outcome, based on the probability distribution function describing the problem to be solved.

Analytical methods for calculation of radiation transport within a medium are mathematically very complex and solutions are limited without the introduction of approximations. Furthermore, analytical approaches yield only the final state of the particle with no information about its passage through the medium. Monte Carlo techniques can be applied to radiation transport by using machine generated random numbers to sample from the probability distributions describing the particle interactions. The trajectory of a single incident particle, including all other particles which may be created along its path, is termed a history. By simulating a large number of these histories, information can be obtained about the average values as well as statistical fluctuations of macroscopic quantities of interest such as absorbed dose and particle or energy fluence in a region of interest. An example of a shower of particles produced in a Monte Carlo simulation is shown in Figure 3-2. An incident photon undergoes a Compton interaction with an electron at point A and the resultant scattered electron leaves the volume of interest. The scattered photon then initiates a pair production event at point B and the resultant positron annihilates with an electron at point C to produce two annihilation photons. All particles generated during this shower are tracked until their energy fall below a specified cutoff or until they leave the volume of interest.

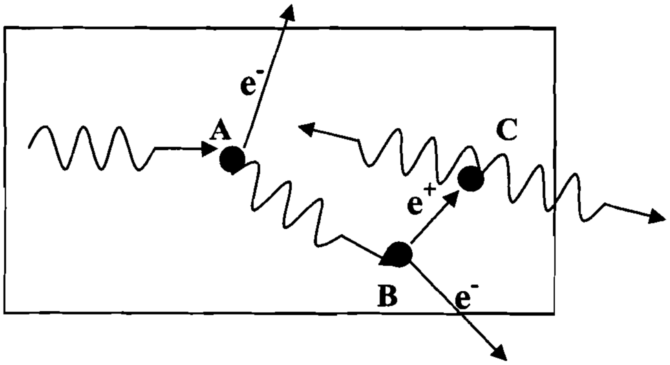

Figure 3-2: Example of a shower of particles simulated by a Monte Carlo code for radiation transport. The incident photon undergoes a Compton interaction at A and the scattered photon initiates a pair production event at B. The resultant positron annihilates with an electron at C to produce to annihilation photons.

A Monte Carlo code for radiation transport has four components: cross-section data from which the probability distributions for each particle interaction may be derived, particle transport algorithms which describe the interaction processes, a definition of the geometry in which the particles are being transported, and a method for scoring quantities of interest.

3.2 Photon Transport

The steps of the photon transport algorithm are summarized in Figure 3-3. The process begins by placing the photon's parameters on the stack. The stack is a register which contains information about all current particles to be transported including the energy, position and direction cosines. The parameters of the particle occupying the first position on the stack are obtained for transport. If the particle's energy falls below a cutoff specified by the user for

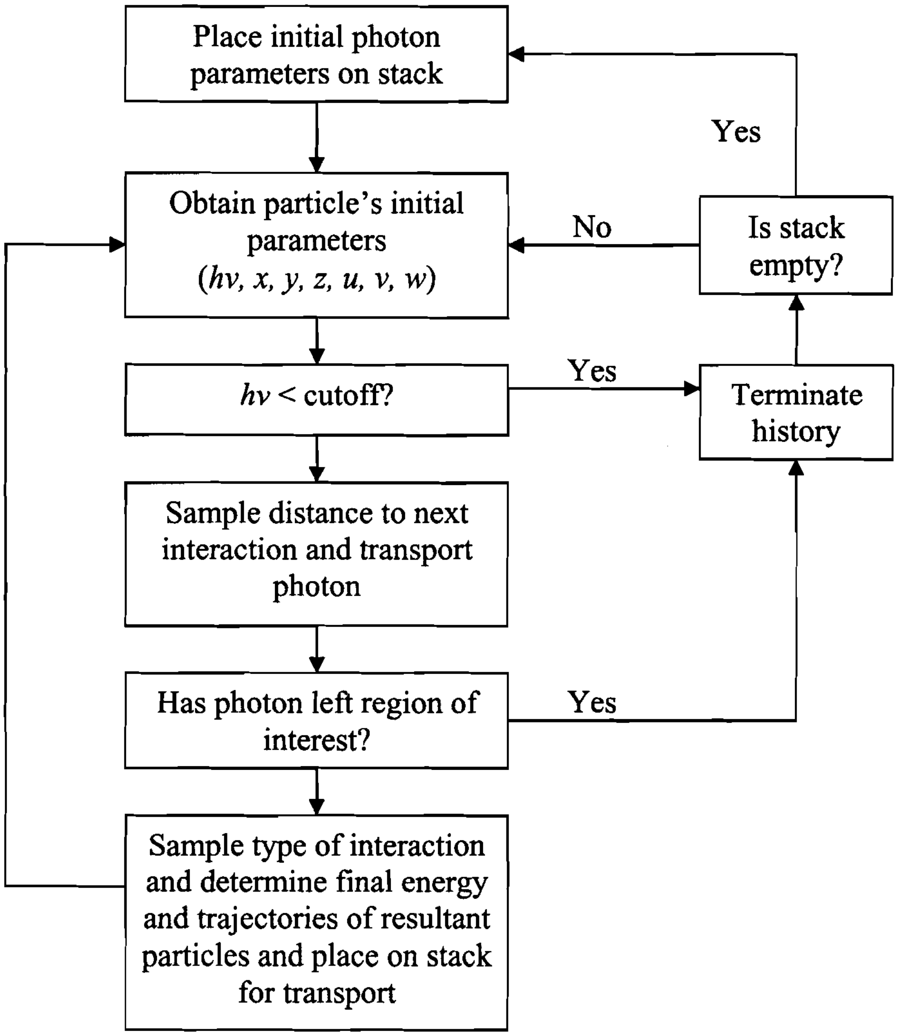

Figure 3-3: Flow diagram showing steps of the photon transport process[1].

particle transport the particle will be discarded and the process begins again for the particle occupying the next position on the stack. If not, the next step is to determine the distance the particle's next interaction. The probability *p(x)* of a particle interacting within a distance x is described by exponential attenuation:

$$p(x) = 1 - e^{-\mu x}, \tag{3.1}$$

where μ is the sum of the linear attenuation coefficients for all the different photon interactions. The probability of interaction is sampled by obtaining a random number R_1 between 0 and 1 and the distance to the point of interaction is calculated as follows:

$$x = 1 - \frac{1}{\mu}\left(1 - R_1\right). \tag{3.2}$$

The photon is transported by the distance x along its current trajectory to the point of interaction. If the photon has left the region of interest the history is terminated, otherwise the next step is to determine the type of interaction which occurs. A second random number R_2 between 0 and 1 is obtained to sample the probability of interaction. By comparing R_2 to the branching ratios for each interaction, the type of interaction is selected. An example is shown below for the case where only photoelectric, Compton and pair production are considered:

$$R_2 \le \frac{\mu_{pe}}{\mu_{tot}} \qquad \text{photoelectric interaction occurs,}$$

$$\frac{\mu_{pe}}{\mu_{tot}} < R_2 < \frac{\mu_{pe} + \mu_{compton}}{\mu_{tot}} \qquad \text{Compton interaction occurs,}$$

$$\frac{\mu_{pe} + \mu_{compton}}{\mu_{tot}} \le R_2 \qquad \text{pair production occurs.}$$

Knowing the type of interaction, the energy and direction of all resulting particles can be determined. These particles are placed on the stack for subsequent transport. Moving to the particle occupying the next position on the stack, the transport process is repeated until the stack is emptied. At this point transport of a new incident photon is placed on the stack and a new history is simulated.

3.3 Electron Transport

Compared to photons, electrons undergo many times more interactions per unit path length. For the purpose of macroscopic energy deposition calculations it is therefore not practical to simulate electron transport on a step by step basis. The condensed history technique proposed by Berger[2] breaks the path of an electron into a series of straight steps for which the effects of individual interactions are grouped together. There exists two classes of condensed history codes. In a *class I* code the creation of secondary particles, such as bremsstrahlung photons and delta electrons, does not affect the energy and direction of the primary electron. The energy lost by an electron for each step is calculated using unrestricted stopping powers. In a *class II* code, secondary particles with energies above a specified threshold are transported separately and continuous energy losses between the discrete interactions are calculated using restricted stopping powers. The electron transport process is illustrated in Figure 3-4.

A *class I* transport code begins by selecting the electron which occupies the first position on the stack. The particle is transported by a predetermined step size t and the scattering angle $\theta(t)$ and lateral deflection ρ is determined from multiple scattering theory[3,4]. Using the scattering angle, a pathlength correction is then applied to correct for curvature of the electron's path as shown in Figure 3-5.

$$\begin{aligned} s &= \frac{t}{2}\left(1+\cos\theta(t)\right) \\ \rho &= \frac{1}{2}t\sin\theta(t) \end{aligned} \quad . \tag{3.3}$$

Knowing the corrected pathlength, the energy lost by the particle is determined and the final energy and direction of the electron are calculated. Secondary particles may be generated along each step based on predetermined distributions for a given energy loss grid.

A *class II* code is similar to a photon transport algorithm in that the distance between discrete interactions is determined based on the total cross-sections for production of bremsstrahlung photons and delta electrons. A step size is then selected and the particle is transported in a straight line, with the scattering angle and energy loss being determined at each step, until the site of the discrete interaction is reached. If the energy of the secondary particle exceeds the threshold for bremsstrahlung photons or delta electrons set by the user, then the energy and direction of the primary particle are changed accordingly and the secondary particle is placed on the stack for transport.

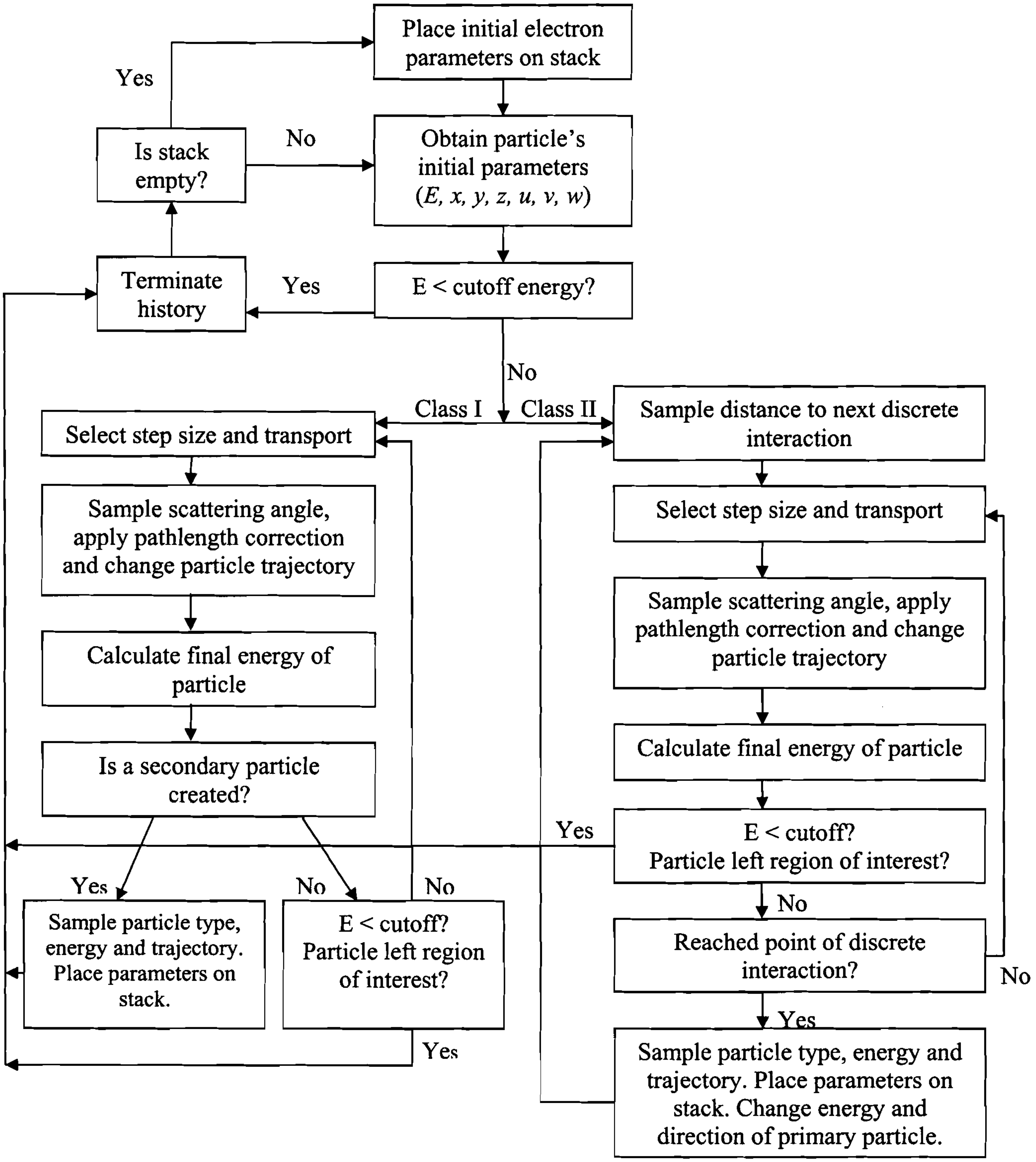

Figure 3-4: Flow diagram illustrating steps of electron transport for Class I and Class II algorithms[1].

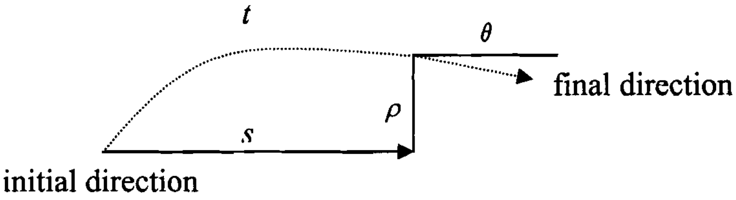

Figure 3-5: Electron pathlength correction; s is the corrected pathlength calculated from the step size t, lateral deflection ρ and scaterring angle θ [1].

3.4 Statistics and calculation efficiency

The scoring routine of a Monte Carlo code calculates the estimate of the mean x and standard error s_x of scored quantities of interest such as dose and fluence. A simulation of N histories is usually split into a series of n batches and, assuming a normal distribution, the mean $\overline{x}$ and standard error $s_{\overline{x}}$ are calculated for each batch as follows[5]:

$$\overline{x} = \frac{1}{n}\sum x_i \,, \tag{3.4}$$

$$s_{\overline{x}} = \sqrt{\frac{\sum\limits_{i=1}^{n}(x_i-\overline{x})^2}{n(n-1)}} = \sqrt{\frac{s^2}{n}} \,, \tag{3.5}$$

where $\overline{x}$ is the average value of quantity x for batch n and s^2 is an estimate of the variance. Another approach is to score these quantities on a history by history basis[6] and in this case equation (3.5), for N histories, is replaced by the following:

$$s_{\overline{x}} = \sqrt{\frac{1}{N-1}\left(\frac{\sum\limits_{i=1}^{N}x_i^2}{N} - \left(\frac{\sum\limits_{i=1}^{N}x_i}{N}\right)^2\right)} \tag{3.6}$$

For a normal distribution in the limit of a large number of histories the quantity Ns^2 is assumed to be constant. Therefore the uncertainty of a scored quantity is inversely proportional to the number of simulated histories and consequently the calculation time. The efficiency ε of a Monte Carlo calculation is defined as:

$$\varepsilon = {}^{1}\!/_{Ts^2} \,, \tag{3.7}$$

where T is the computing time required to obtain an estimated variance s^2.

3.5 Variance reduction techniques

The efficiency of a Monte Carlo simulation can be improved through the use of variance reduction techniques to either reduce the calculation time for a given variance or the variance for a given CPU time. However, careful validation of these techniques is required to avoid introducing errors in the simulation.

The "range rejection" technique is often applied in electron transport algorithms to terminate the transport of a particle whose range is less than the distance to the nearest geometrical boundary. By ending the particle transport within the current region the production of any secondary particles generated by the electron along the remainder of its path is neglected. The transport of particles which are moving away from a region of interest may be randomly terminated by application of a "Russian roulette" technique which removes the particles with a certain probability and subsequently increases the weight of the surviving particles. Another method of improving the calculation efficiency of an electron transport algorithm is by the use of larger step sizes when far away from a geometrical boundary. This technique is used in the PRESTA[7] electron transport algorithm of the EGS4 Monte Carlo code.

The relatively lower probability of photon interaction necessitates a large number of incident histories to reduce the variance of the scored quantities. Therefore the efficiency of a photon simulation can be increased by artificially increasing the probability of interaction. The "interaction forcing" and "exponential transform" techniques force photons to interact within a geometrical region or bias the sampling procedure for calculating the distance to the next interaction, as defined in Equation 3-2, to improve the probability of interaction within a specific region at the expense of other regions along the photon's path. To avoid introducing errors in the calculation, the particle weights are reduced to compensate for the increased interaction probability and, for every scattered particle, an unscatterred particle is regenerated with a complementary weight. Another method of increasing the probability of interaction is to artificially increase the photon cross-sections. This cross-section enhancement is used in the ETRAN[8] and EGS Monte Carlo codes. A variance reduction technique which has a particular application in the simulation of photon beams produced by linear accelerators is the use of bremsstrahlung splitting in the target. The efficiency of the production of bremsstrahlung photons in the target can be increased by splitting every bremsstrahlung photon into *N* photons each with a weighting of *1/N.*

3.6 The EGSnrc Monte Carlo code

The Electron Gamma Shower (EGS) Monte Carlo code simulates the transport of photons and electrons in various geometry and media in an energy range of a few keV to TeV. The original version was developed in 1978 by Ford and Nelson at the Stanford Linear Accelerator Center for simulation of high energy electrons in lead. The code was subsequently modified[9,10] to allow simulations in media with atomic number ranging from 1 to 100 and to extend photon and electron transport to energies of 0.1 MeV and 0.01 MeV, respectively. The code is written in the MORTRAN3 language which is a FORTRAN pre-processor.

The EGS code simulates the following physical processes: bremsstrahlung photons, knock-on electrons, positron annihilation, multiple scattering of charged particles, pair production, Compton scattering, Rayleigh scattering and photoelectric interactions. The code uses a *class II* condensed history electron transport algorithm called PRESTA[7] (Parameter Reduced Electron Step Transport Algorithm) which employs a path length and lateral displacement correction based on the Moliere[3] multiple scattering theory. Variance reduction techniques such as bremsstrahlung splitting, Russian roulette and range rejection are available.

Cross-section and stopping power data required for the simulations is prepared using the PEGS4 pre-processor. The Klein-Nishina cross-sections are calculated for Compton interactions while the cross-sections for other photon interactions are obtained from data tabulated by Storm and Israel[11]. Restricted stopping powers are calculated using the formulation of Seltzer and Berger[12] based on bremsstrahlung and delta electron thresholds AP and AE specified by the user.

In 2000 a new version of the code called EGSnrc[13] was made available. The major improvements compared to EGS4 include a new electron transport algorithm PRESTA II which incorporates a new multiple scattering theory that accounts for relativistic spin effects and an improved boundary crossing algorithm. The improved boundary crossing algorithm restricts the electron step size and switches to single scattering mode in the vicinity of a geometrical boundary. The low energy photon physics have also been expanded to account for binding effects in Compton scattering and atomic relaxations.

The structure of the EGSnrc code is shown in Figure 3-6. The code consists of two

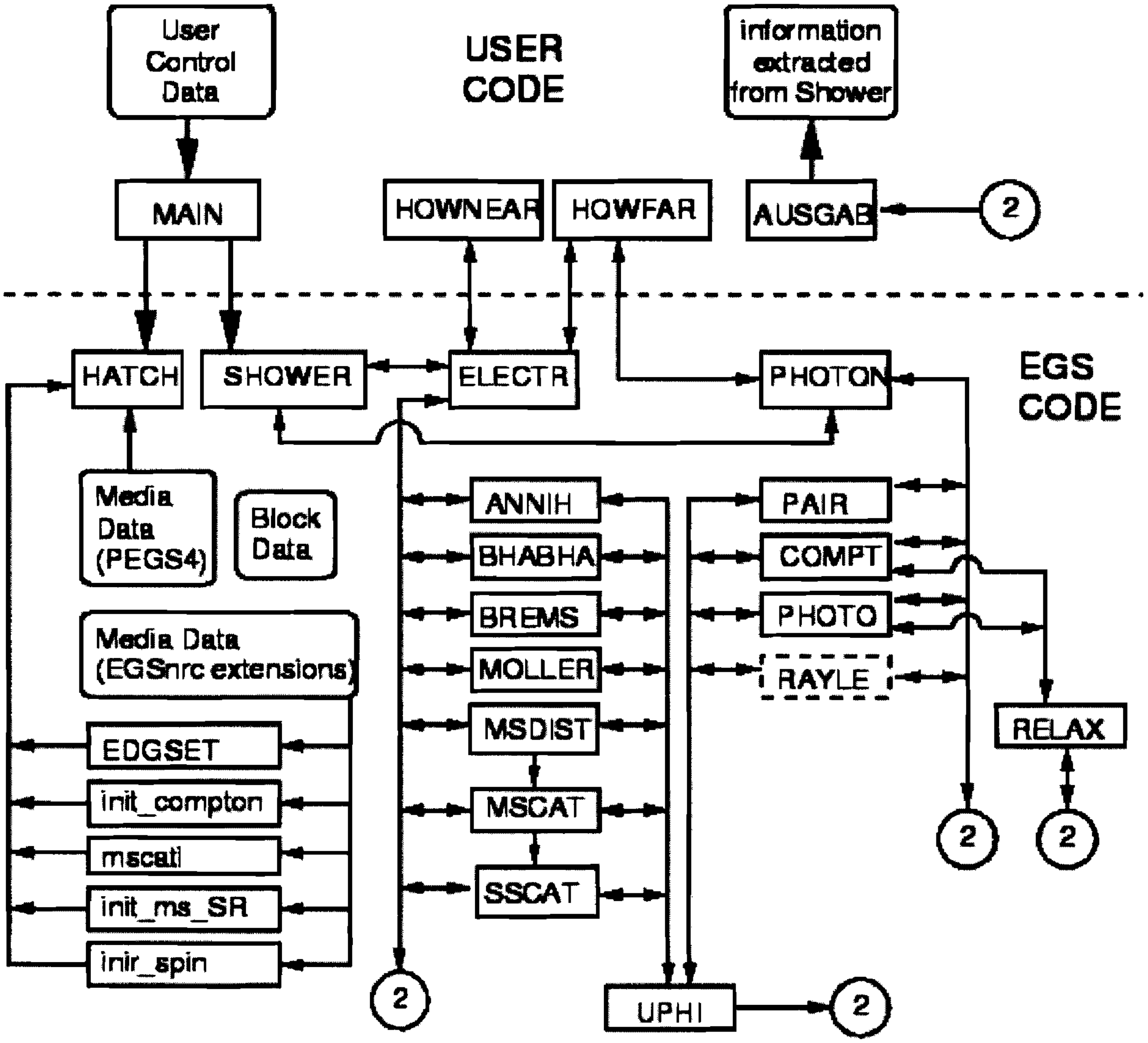

Figure 3-6: Structure of the EGSnrc Monte Carlo code[14]

main sections: the user code and the EGS code. The EGS code section contains the particle transport algorithms and cross-section data and generally does not require any modification by the user. The user code section consists of the MAIN, HOWFAR, HOWNEAR and AUSGAB subroutines which handle the data in the input file, define the geometry and define the scoring quantities of interest, respectively. The input file contains information about simulation parameters such as number of incident histories, source type and cutoff energies for particle transport.

The HOWFAR and HOWNEAR components[15] of the code are concerned with defining the simulation geometry, in particular determining the distance between the particle and the nearest boundary. Specifically, HOWFAR calculates the distance along the particle's trajectory to the nearest boundary. The subroutine is called with a given step size USTEP, calculated from equations similar to Equation 3.2 and other restrictions such as the maximum fractional energy loss per step, and returns the minimum of USTEP or distance to the nearest boundary and, if a crossing occurs, the new region number. The HOWNEAR subroutine is used for electron transport and is called by PRESTA to determine the minimum distance in any direction to the nearest boundary. The geometry is defined as a mesh of sub-regions defined by simple geometrical shapes. Each sub-region is assigned a medium index and a change in this index indicates that a boundary crossing has occurred.

3.7 The EGSnrc user codes

The EGSnrc code includes several user codes for scoring different quantities in a specific geometry. These include DOSXYZnrc and DOSRZnrc which score dose in Cartesian and cylindrical coordinates, respectively, and the SPRRZnrc, CAVRZnrc and FLURZnrc codes which respectively score restricted collisional stopping power ratios, ion chamber parameters, and fluence spectra in cylindrical coordinates.

3.8 BEAMnrc

The BEAMnrc user code[16] simulates photon and electron beams produced by linear accelerators, orthovoltage, and cobalt-60 units. The code, which is based on the EGSnrc Monte Carlo code system, produces as its output a phase space file containing the position, energy, charge, direction and history of interactions of all particles at a specified scoring plane within the accelerator model. An accelerator model is built from a series of independent component modules (CMs), each of which models a specific geometrical shape. These CMs contain the HOWFAR and HOWNEAR subroutines specific to the geometry being modeled as well as subroutines for obtaining the data from the input file which contains the materials, dimensions and location of each CM. The model "building" process consists of specifying which CMs are to be included and assigning a unique identifier to each component. The CM subroutines are then added at appropriate locations to the main BEAMnrc code to create a unique code for modeling the specific accelerator.

3.9 PEREGRINE

The PEREGRINE[17] Monte Carlo dose calculation system was originally developed at the Lawrence Livermore National Laboratory. Currently available with the NOMOS CORVUS inverse treatment planning system (NOMOS Corp, Cranberry Township, PA), PEREGRINE is the first commercially available Monte Carlo dose calculation code for photon beams. Variance reduction techniques are employed to improve the dose calculation efficiency in the patient but the most significant gain in efficiency is due to the use of a source model to describe the distribution of particles in the accelerator head above the collimating jaws.

The source model[18] is based on simulations of the accelerator head using the BEAM/EGS4 code. The phase space file is scored at the bottom of the monitor unit chamber and the LATCH parameter is used to determine the location of the last interaction of each particle. As shown in Figure 3-7, the particles in the phase space are identified as originating in one of four subsources: primary photons from the target, scattered photons from primary collimator and flattening filter, and all electrons. To avoid transporting particles which will be blocked by the collimating jaws, the particles are transported in straight lines along their current trajectories and those that fall outside the region where the energy fluence drops below 0.2% of the maximum value are discarded. In the case of the target photons this cutoff radius corresponds to a 40x40 cm^2 field size. For the scattered photons the cutoff is dependent on the openings of the collimating jaws and therefore tables of radial cutoffs as a function of jaw position are tabulated. For the electron subsource the radial cutoff is chosen such that the buildup region dose was independent of the chosen cutoff.

A set of correlated histograms are calculated for both the isocenter and source plane of each subsource to describe the energy, radial and angular distributions of the particles emanating from each source. In the isocenter plane this includes a description of the rotationally symmetric planar energy fluence and the energy spectrum.

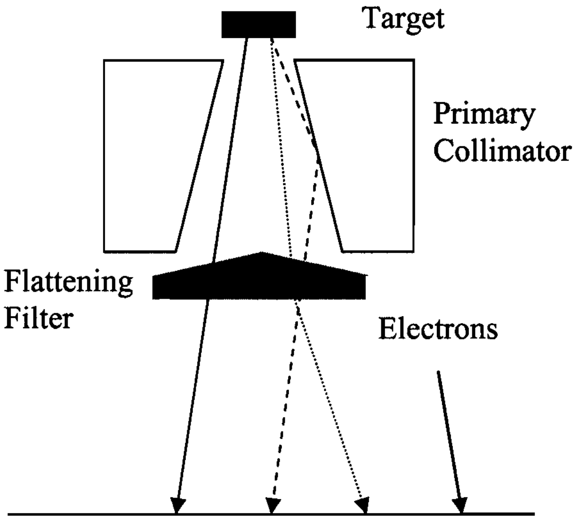

Figure 3-7: Schematic diagram illustrating the four components of the PEREGRINE source model: primary photons originating in the target, scattered photons from the primary collimator and flattening filter, and all electrons.

In the latter case, the isocenter plane is divided into annular tiles and the energy spectrum is calculated for each tile. The position of each subsource within the accelerator head is determined by projecting the particles in the phase space back along their trajectories and determining where they converge to a minimum radius along the z axis. The tiles in the isocenter plane are backprojected to the virtual source plane and probability distributions describing the starting radial and angular positions of the particles for each tile are calculated.

These histograms, along with information about the geometry, composition and location of any beam modifiers, are stored in a device file. Also included in this file are monitor chamber backscatter factors as a function of jaw setting[19]. Since the collimating jaws are not included in the phase space simulations the model does not account for particles which are backscattered from the jaws into the monitor unit chamber, therefore increasing the signal and reducing the delivered dose. A dose per monitor unit calibration factor for a reference field size and depth is also specified in the device file.

To account for variation in the energy of photon beams produced by individual linear accelerators an instantiation step is performed before the PEREGRINE beam model is implemented for calculations. This step involves determining the incident electron beam energy on the target which matches a calculated off-axis profile to measurement at a depth of 10 cm for a 38 x 38 cm^2 field. Device files are created for a range of incident electron beam energies and an interpolation between these files is performed to obtain a device file for the tuned electron beam energy.

The process of sampling an incident particle from the source model is illustrated in Figure 3-8. Based on the jaw settings for the current field the radial cutoffs are determined and the energy delivered to the isocenter plane by the remaining particles in each subsource is calculated. The source of the incident particle is then sampled based on the fractional energy contribution of each subsource. The coordinates in the isocenter plane (x_{iso},y_{iso}) are uniformly sampled and the relative energy fluence at the corresponding radial position R_{iso} is used to modify the particle weight.

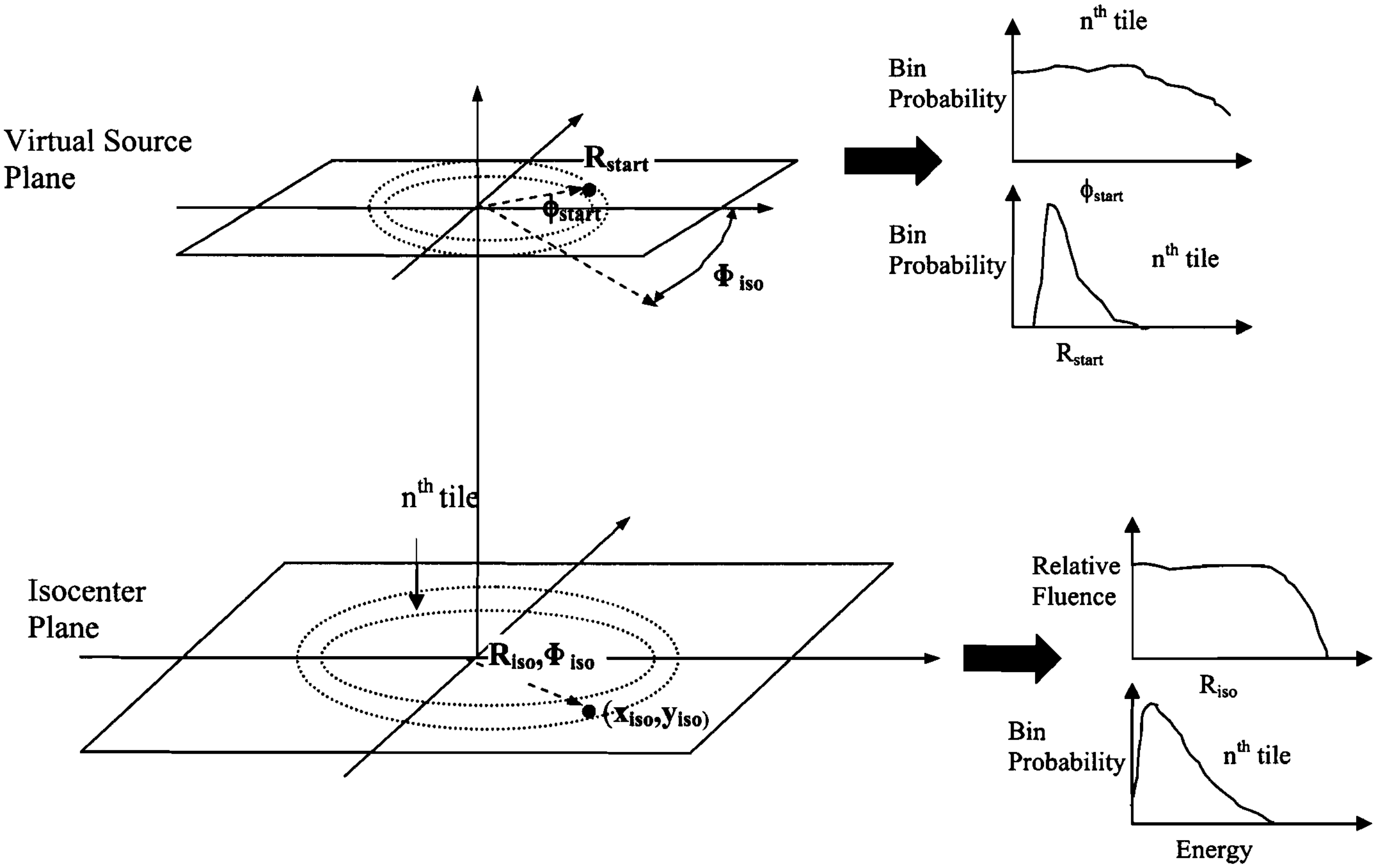

Figure 3-8: Sampling process for PEREGRINE source model. Based on a uniformly sampled starting position in the isocenter plane, the particle energy, weight and trajectory are determined from a set of correlated histograms generated for each subsource of the model.

The energy of the particle is randomly sampled from the isocenter tile which is closest to the particle's position. The next step is to sample the starting radial R_{start} and angular position ϕ_{start} in the virtual source plane. Knowing the position in both planes allows the trajectory of the particle to be calculated. The particle is then moved to the bottom of the monitor unit chamber before beginning transport through the beam modifiers.

Once a particle is sampled from the source model it is transported through the collimating jaws and multi-leaf collimator. The patient is described by a 3-dimensional density grid derived from CT data. As shown in Figure 3-9, an independent grid of overlapping spheres called dosels is used for scoring dose.

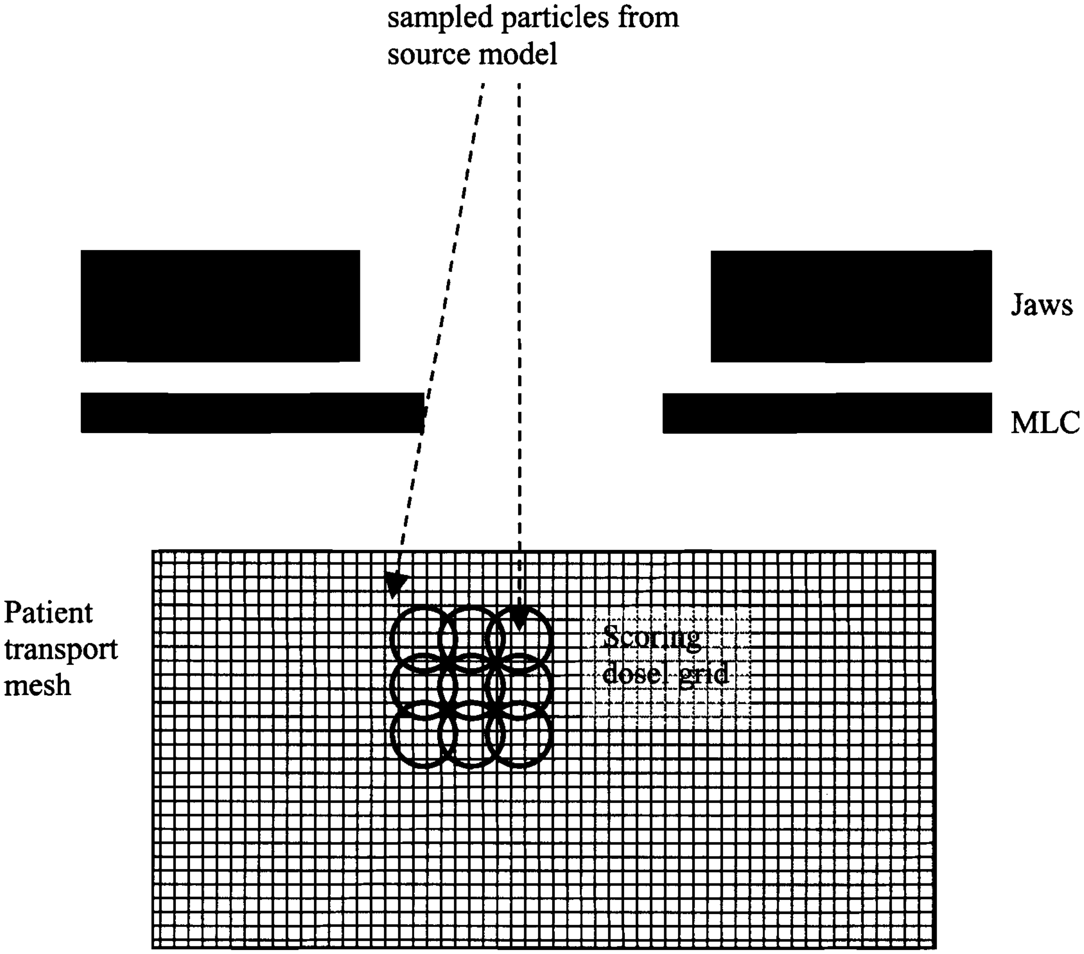

Figure 3-9: PEREGRINE dose calculation process. Particles are sampled from the source model and transported through the beam modifiers and patient transport mesh derived from CT data. Dose is scored in an independent mesh of overlapping spheres called dosels.

PEREGRINE uses a photon transport algorithm similar to that implemented in EGSnrc with certain variance reduction techniques, such as the Woodcock tracing technique[20], to increase the computational efficiency. The Woodcock tracing technique involves calculating the distance to the next photon interaction site based on the maximum total cross-section μ_{max} for the whole transport medium. When the interaction site is reached the probability of interaction, based on the cross-section μ for the current voxel, is randomly sampled to determine if the interaction is fictitious or does in fact occur. In the case of a fictitious interaction the photon's energy and trajectory are unchanged. A *class II* condensed history electron transport technique is used with a path length and lateral deflection correction based on multiple scattering theory. Range rejection is used to terminate the transport of a particle whose energy is less than that required to travel 1/3 of a voxel's dimensions. Bremsstrahlung photons are modeled only by subtracting their energy from the incident electron, the angular deflection is not accounted for. Cutoff energies of 0.1 keV and 521 keV (including the rest mass) are used for photon and electron transport, respectively.

The photon cross-section data is obtained from the Lawrence Livermore National Laboratory Evaluated Photon Data Library[21]. Restricted stopping powers are calculated based on formulas from ICRU Report 37[22] while cross-section data for bremmstrahlung and delta electrons are obtained from the Lawrence Livermore National Laboratory Evaluated Electron Data Library[23]. Particle splitting, Russian roulette and source particle reuse are also implemented to improve calculation efficiency. Electrons are restarted at the bottom of the beam modifiers and photons at the CT grid.

3.10 References

[1] D.W.O. Rogers and A.F. Bielajew, "Monte Carlo Techniques of Electron and Photon Transport for Radiation Dosimetry," *The Dosimetry of Ionizing Radiation*, (Academic Press, New York, 1990).

[2] M.J. Berger, "Monte Carlo Calculation of the Penetration and Diffusion of Fast Charged Particles," *Methods in Computational Physics Volume 1: Statistical Physics* (Academic Press, New York,1963).

[3] G. Moliere, "Theorie der Streuung schneller geladener Teilchen II:Mehrfach-und Vielfachstreuung," Z. Naturforsch. **3a**, 78 (1948).

[4] S. Goudsmit and J.L. Saunderson, "Multiple Scattering of Electrons," Phys. Rev. **57**, 24 (1940).

[5] P.R. Bevington and D.K. Robinson, *Data Reduction and Error Analysis for the Physical Sciences*, (McGraw-Hill, New York, 1992).

[6] B.R.B. Walters, I. Kawrakow and D.W.O. Rogers "History by history statistical estimators in the BEAM code system," Med. Phys. **29**, 2745 – 2752 (2002).

[7] A.F. Bielajew and D.W.O Rogers, "PRESTA – The "Parameter Reduced Electron-Step Transport Algorithm" for electron Monte Carlo transport," NRCC Report PIRS-0042, NRCC Canada (1987).

[8] M.J. Berger and S.M. Seltzer, "ETRAN, Monte Carlo code system for electron and photon transport through extended media," *Documentation for RSIC Computer Code Package CCC-107* (Oak Ridge Natl. Lab., Oak Ridge, Tennessee, 1973).

[9] W.R. Nelson, J. Hirayama and D.W.O Rogers, "The EGS4 code system," Stanford Linear Accelerator Report SLAC-265 (1985).

[10] A.F. Bielajew, H. Hirayama, W.R. Nelson and D.W.O. Rogers "History, overview and recent improvements of EGS4," NRCC Report PIRS-0436, NRCC Canada (1994).

[11] E.Storm and H.I. Israel, "Photon cross-sections from 1 keV to 100 MeV for element Z=1 to Z=100," Atomic Data and Nuclear Data Tables **7**, 565-681 (1997).

[12] M.J. Berger and S.M. Seltzer, "Tables of Energy Losses and Ranges of Electrons and Positrons," NASA Report SP-3012, NASA Washington (1964).

[13] I. Kawrakow, "Accurate condensed history Monte Carlo simulation of electron transport. I EGSnrc, the new EGS4 version," Med Phys **27**, 485 – 498 (2000).

[14] I. Kawrakow and D.W.O. Rogers, "The EGSnrc Code System: Monte Carlo Simulation of Electron and Photon Transport," NRCC Reports PIRS-701, NRC Canada (2001).

[15] A.F. Bielajew, "HOWFAR and HOWNEAR: Geometry Modeling for Monte Carlo Particle Transport," NRCC Reports PIRS-0341 (1995).

[16] D.W.O. Rogers, B.A. Faddegon, G.X. Ding, C.M. Ma and J. We, "BEAM: A Monte Carlo code to simulate radiotherapy treatment units", Med Phys **22**, 503– 524 (1995).

[17] C.L. Hartmann Siantar, R.S. Walling, T.P. Daly, B. Faddegon, N. Albright, P. Bergstrom, A.F. Bielajew, C. Chuang, D. Garrett, R.K. House, D. Knapp, D.J. Wieczorek and L.J. Verhey, "Description and dosimetric verification of the PEREGRINE Monte Carlo dose calculation system for photon beams incident on a water phantom," Med. Phys. **28**, 1322-1337 (2001).

[18] A.E. Schach von Wittenau, L.J. Cox, P.M. Bergstrom, Jr., W.P. Chandler and C.L. Hartmann Siantar, "Correlated histogram representation of Monte Carlo derived medical accelerator photon-output phase space", Med. Phys. **26**, 1196-1211 (1999).

[19] C. Duzenli, B. McClean and C. Field, "Backscatter into the beam monitor chamber: Implications for dosimetry of asymmetric collimators," Med. Phys. **20**, 363-367 (1993).

[20] I. Lux and L. Koblinger, *Monte Carlo Particle Transport Methods:Neutron and Photon Calculations*, (CRC Press, Boca Raton, 1991).

[21] D.E. Cullen, M.H. Chen, J.H. Hubbell, S.T. Perkins, E.F.Plechaty, J.A. Rathkopf and J.H Scofield, Lawrence Livermore National Laboratory Report UCRL-50400, Volume 6, LLNL, Livermore (1989).

[22] ICRU, "Stopping Powers for Electrons and Positrons," ICRU Report No. 37, International Commission on Radiation Units and Measurements, Bethesda (1984).

[23] S.T. Perkins, D.E. Cullen and S.M. Seltzer, Lawrence Livermore National Laboratory Report No. UCRL-50400, Vol. 31, LLNL, Livermore (1991).

Chapter 4:

Development and validation of a new MLC component module for BEAMnrc

4.1 Multi-leaf collimators

A multi-leaf collimator (MLC) is a beam collimation device which consists of opposing pairs of motor driven leaves. The independent motion of the leaves makes it possible to define irregular field shapes therefore allowing the radiation field to be conformed to the tumour. This has led to the application of MLCs in the replacement of conventional shield blocks and, more recently, for delivery of intensity modulated radiation therapy (IMRT) where computer controlled motion of the leaves, with the radiation beam on, allows the delivery of arbitrary intensity patterns.

4.2 The Varian Millenium 120 leaf MLC

The Varian Millenium 120 leaf collimator (Varian Oncology Systems, Palo Alto, CA) consists of 80 inner leaves and 40 outer leaves whose width project to 0.5 cm and 1.0 cm, respectively, at isocenter. A photograph of the MLC is shown in Figure 4-1, with an inner leaf extended. A cross-sectional view of the inner and outer leaves is illustrated in Figure 4-2. The leaves are composed of a tungsten alloy whose physical density ranges from 17.0 to 18.5 g/cm^3, depending on the alloy composition[1]. The outer and inner leaves are 6.7 cm and 6.5 cm in height, respectively. To account for the beam divergence and minimize the geometric penumbra across the leaves, the leaf sides are focussed towards the target. Likewise, the leaf ends are rounded to maintain a fairly constant penumbra size as a function of the leaf position[2]. This design leads to a non-linear relationship between the physical leaf opening and the projection at the isocenter plane[3]. The leaves are driven linearly in and out of the field by a motor driven lead screw which extends to within approximately 2 cm of the leaf end. When the leaves are driven to their furthest extent from the carriage, approximately 15 cm, the driving screw is retracted leaving a 3 mm diameter hole in the leaf.

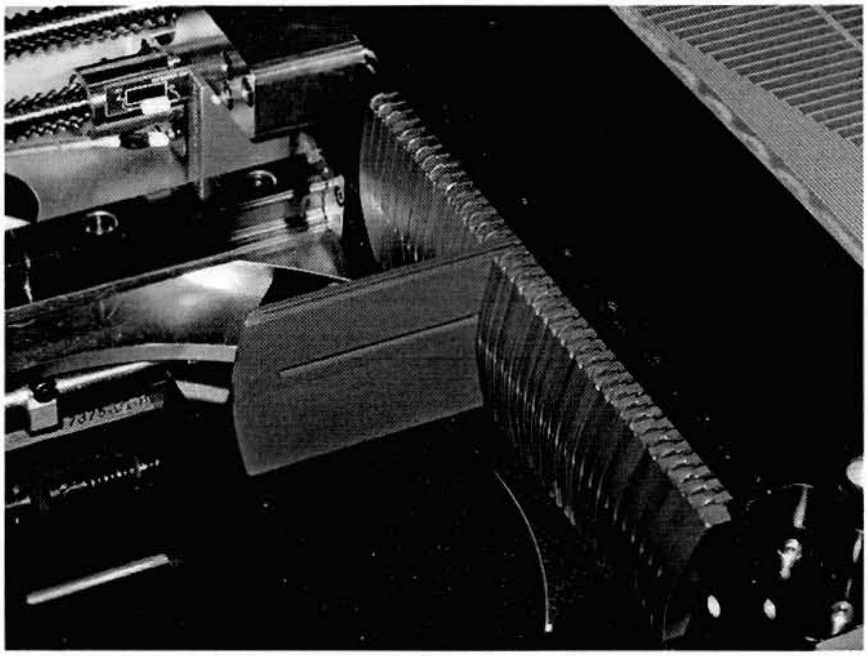

Figure 4-1: Leafbank of Millenium 120 leaf MLC with an inner leaf extended. Each leaf bank consists of 20 outer leaves and 40 inner leaves whose width project to 0.5 cm and 1.0 cm, respectively, at isocenter. The leaves are driven in and out of the field by a motor driven lead screw (note driving screw hole in extended leaf).

The leaf movement is supported by a rail on which the leaves slides and and the leaf has a small tip on the opposite side to compensate for the missing material due to the railing groove. To minimize friction and allow the leaves to move freely, adjacent leaves are separated by a small air gap which is designated as the interleaf air gap. An interlocking tongue and groove design blocks the direct path of any leakage radiation between adjacent leaves, however a certain amount of radiation is scatterred between the leaves and contributes to the interleaf leakage. To avoid collisions between opposing leaves, a small air gap exists between a completely closed leaf pair. The combination of this abutting leaf gap and the rounded leaf ends also contribute to a significant leakage between each closed opposing leaf pair. For IMRT treatment plans the total dose delivered is the sum of many subfields and therefore the summed contribution of these abutting leaf and interleaf leakage effects can become significant in low dose regions.

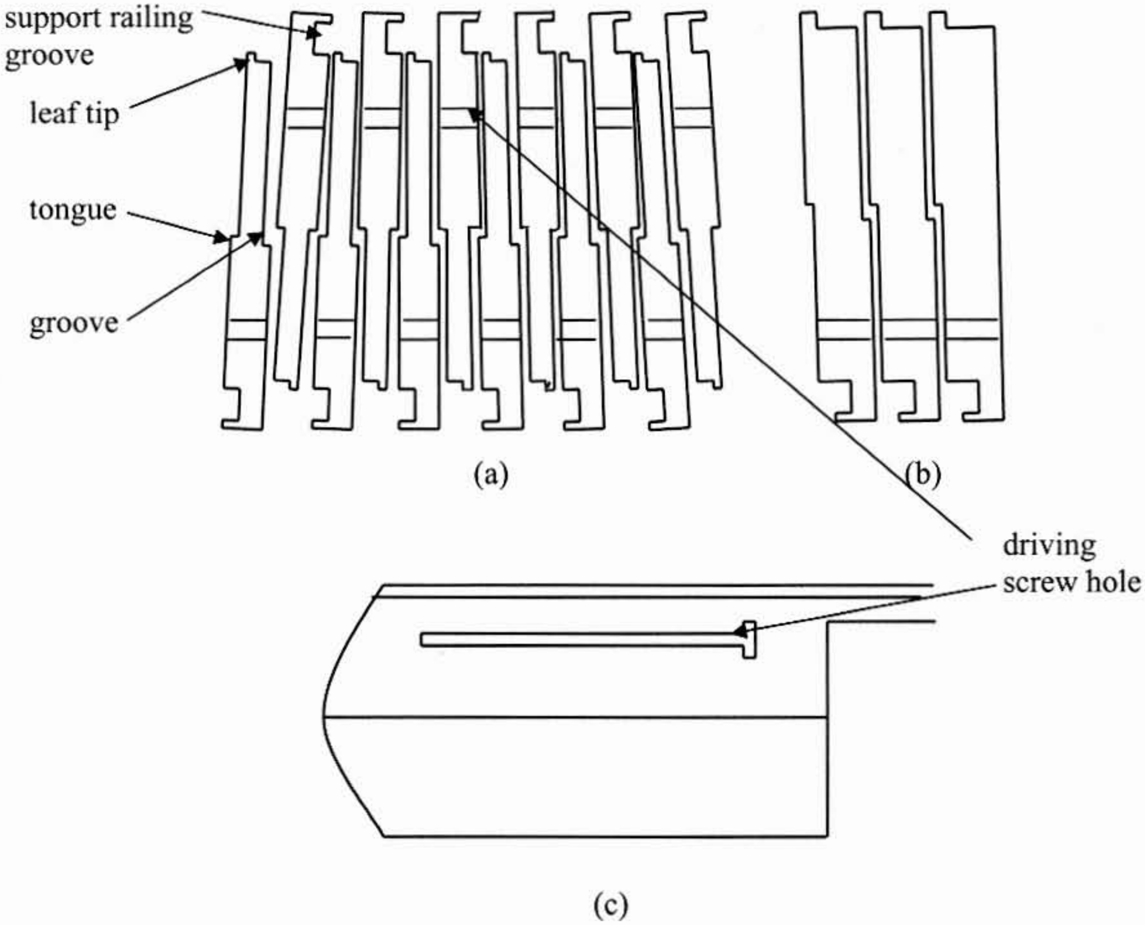

Figure 4-2: Cross-sectional view of (a) inner and (b) outer MLC leaves and (c) side view of a leaf illustrating the support railing groove, leaf tip, tongue, groove and driving screw hole.

An additional concern is the effect of the tongue and groove as illustrated in Figure 4-3. Due to the extra material of the tongue the field profile defined by the leaf in field (a) does not fall off uniformly. Instead there is a small step in the profile caused by the attenuation provided by the tongue. In a field sequence where two adjacent leaves alternately block the field, as shown in (a) and (b), in the summed profile (c) the area which is covered by the tongue and groove can be underdosed by as much as 33%, depending on the tongue and groove design[4].

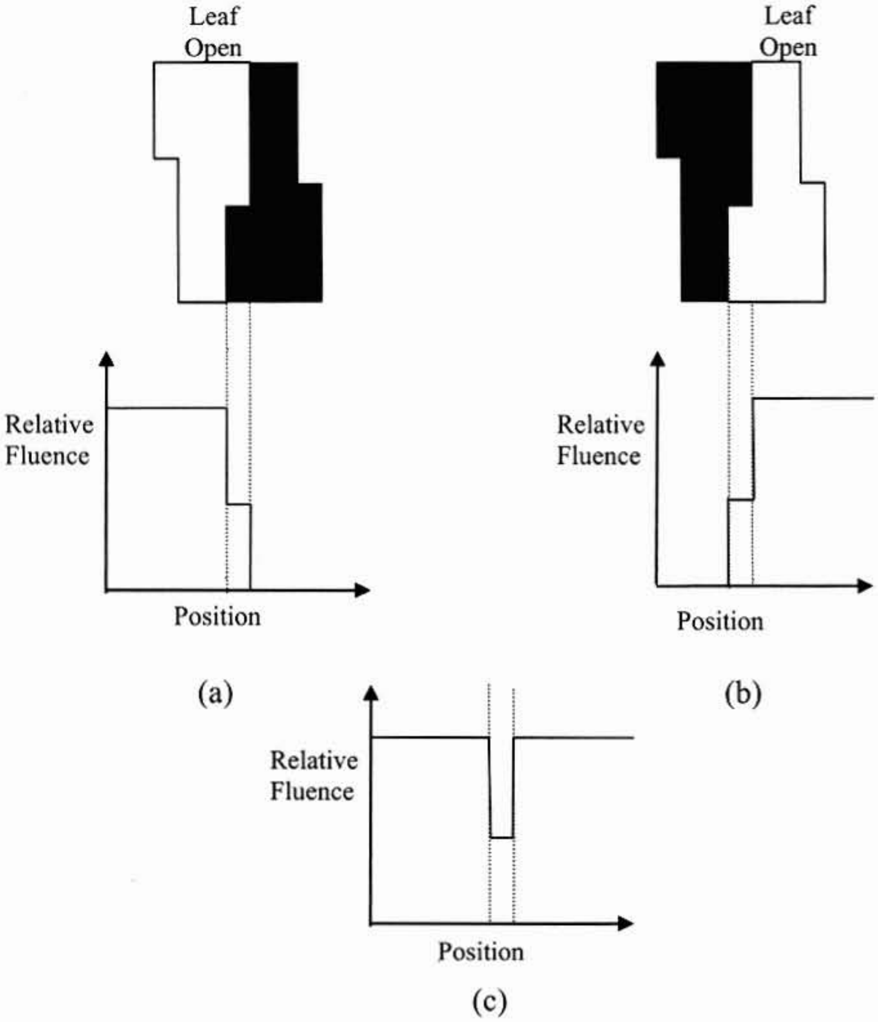

Figure 4-3: Illustration of the tongue and groove effect. The sum of two sequences in which the groove (a) and tongue (b) of adjacent leaves alternately block the field results in a underdosage (c) in the region where the tongue and groove overlap.

4.3 VARMLC component module

One of the currently available component module in BEAMnrc for modelling MLCs is called VARMLC[5]. The geometry of this CM is defined in Figure 4-4. The leaves are modeled as diverging rectangular slabs with an interlocking tongue and groove and either rounded or focused leaf ends. It is important to note that all the leaf dimensions, with the exception of the leafwidth, are defined for the MLC as a whole and only a single leaf geometry type can be modeled. Furthermore, features such as the leaf tips, driving screw hole

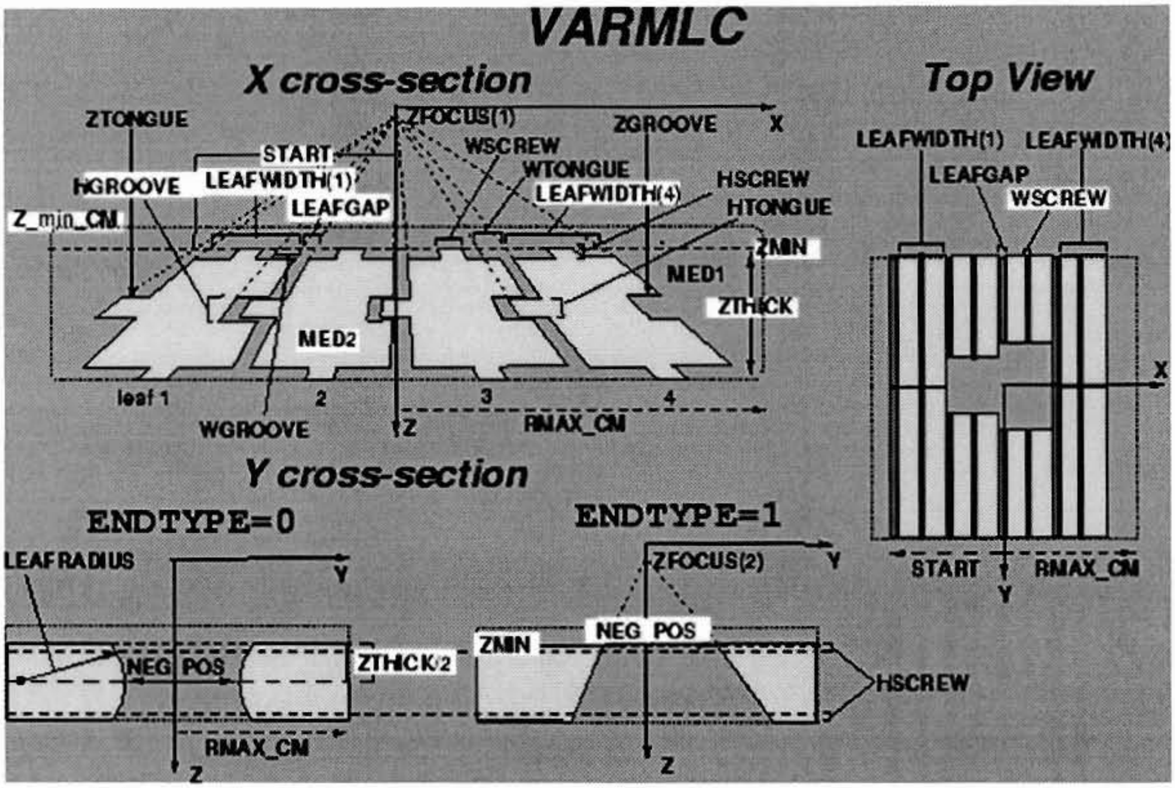

Figure 4-4: Geometry of the VARMLC component module[6].

and leaf groove are not supported by this geometry. Therefore it is not possible to accurately model the Millennium 120 leaf MLC using the VARMLC component module.

4.4 DYNVMLC component module

The existing VARMLC component module was modified to produce a new CM, called DYNVMLC, which fully models the geometry of the Millenium 120 leaf collimator. These modifications include a refined geometry which models the three distinct leaf types and the definition of leaf dimensions on an individual basis.

The geometry of the three leaf types modelled in the new CM: Target, Isocenter and Full, are illustrated in Figure 4-5. To account for the difference in thickness of the inner and outer leaves, the inner leaves are offset vertically from the component module boundaries Z_{min} and Z_{max} by a small air gap designated by the variable *TIPGAP*. The leaf hole, tips and support railing groove are fully modelled and the divergent leaf sides and option of rounded or divergent leaf ends, as defined in VARMLC, are unchanged.

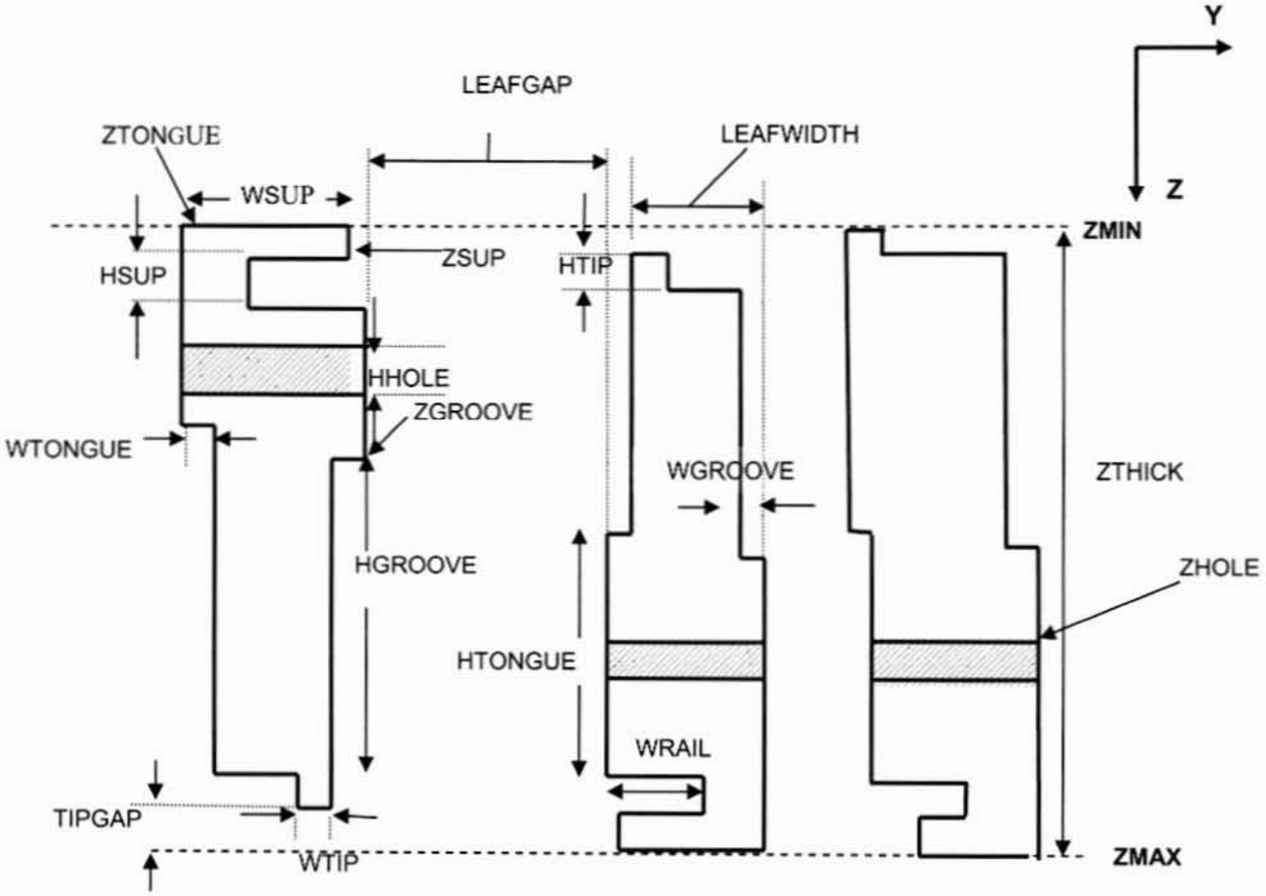

(a) Target, Isocenter and Full leaf geometry

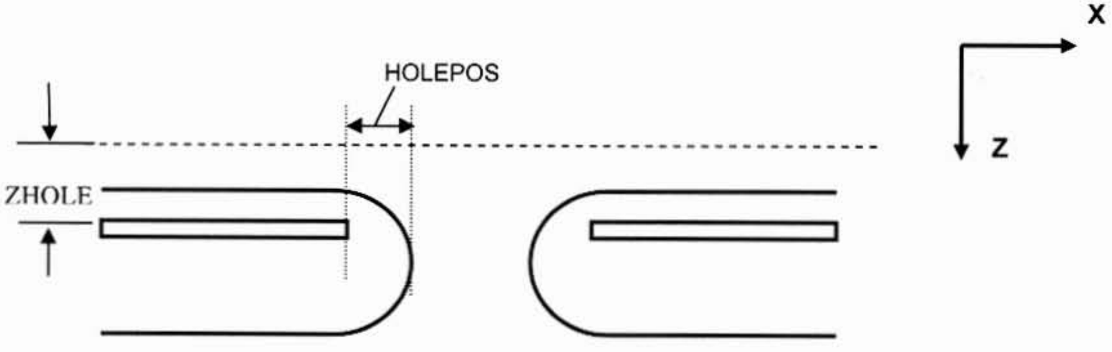

(b) Location of driving screw hole

Fig 4-5: Geometry of DYNVMLC component module illustrating the three leaf types: Target, Isocenter and Full.

The INPUT subroutine was modified to read in the dimensions for each leaf and store them in an array using the leaf number as an index. Based on the relative Z positions of the tongue and groove the leaf type is determined and a series of checks are performed to test for overlap between adjacent leaves and any other errors in the leaf geometry. Each leaf is divided into a set of sub-regions bound by a series planes in the X, Y, and Z directions as shown in Figure 4-6. Depending on the orientation of the leaves, the X or Y planes diverge to account for the focussed leaf sides. The medium of each sub-region is defined to be leaf material, air or the medium of the driving screw hole, which is set as air. Depending on the sub-region in which a particle is located, the HOWFAR subroutine uses a geometry specific calculation to determine the intersection of the particle's current trajectory with a plane defining the leaf medium boundary. Similarly the HOWNEAR subroutine calculates the minimum of the distances to the nearest boundary planes in the X, Y and Z directions.

All leaf dimensions were obtained from the manufacturer's technical drawings. An interleaf gap of 0.0057 cm was determined by directly measuring the width of a pack of leaves in the MLC and subtracting the individual leaf widths. A tungsten alloy with a composition of 90% tungsten, 6% nickel, 2.5% copper and 1.5% iron was used for the leaf material. To account for variations in the manufactured leaf density, the density was chosen to match the MLC leakage and transmission predicted by the model to measurements, as discussed in the following section. The air gap between the abutting leaves was also determined by fitting the predicted abutting leaf leakage to measurements.

To test the modified component module geometry a ray tracing of particle trajectories through the MLC was performed with the leaf medium set to air. Each time a particle crossed a boundary between the leaf material and air its coordinates were output to a file. A three dimensional projection of an iscocenter leaf pair is shown in Figure 4-7. Shown in Figure 4-8 is a two-dimensional projection of two full leaves followed by two target/isocenter leaf pairs. The detailed leaf geometry, including the rounded leaf ends, driving screw hole, leaf tips, support railing groove and divergent leaf sides, are clearly visible in the ray tracings. A vertical air gap between the tongue and groove of adjacent leaves is visible and the size of this air gap alternates between adjacent inner leaves.

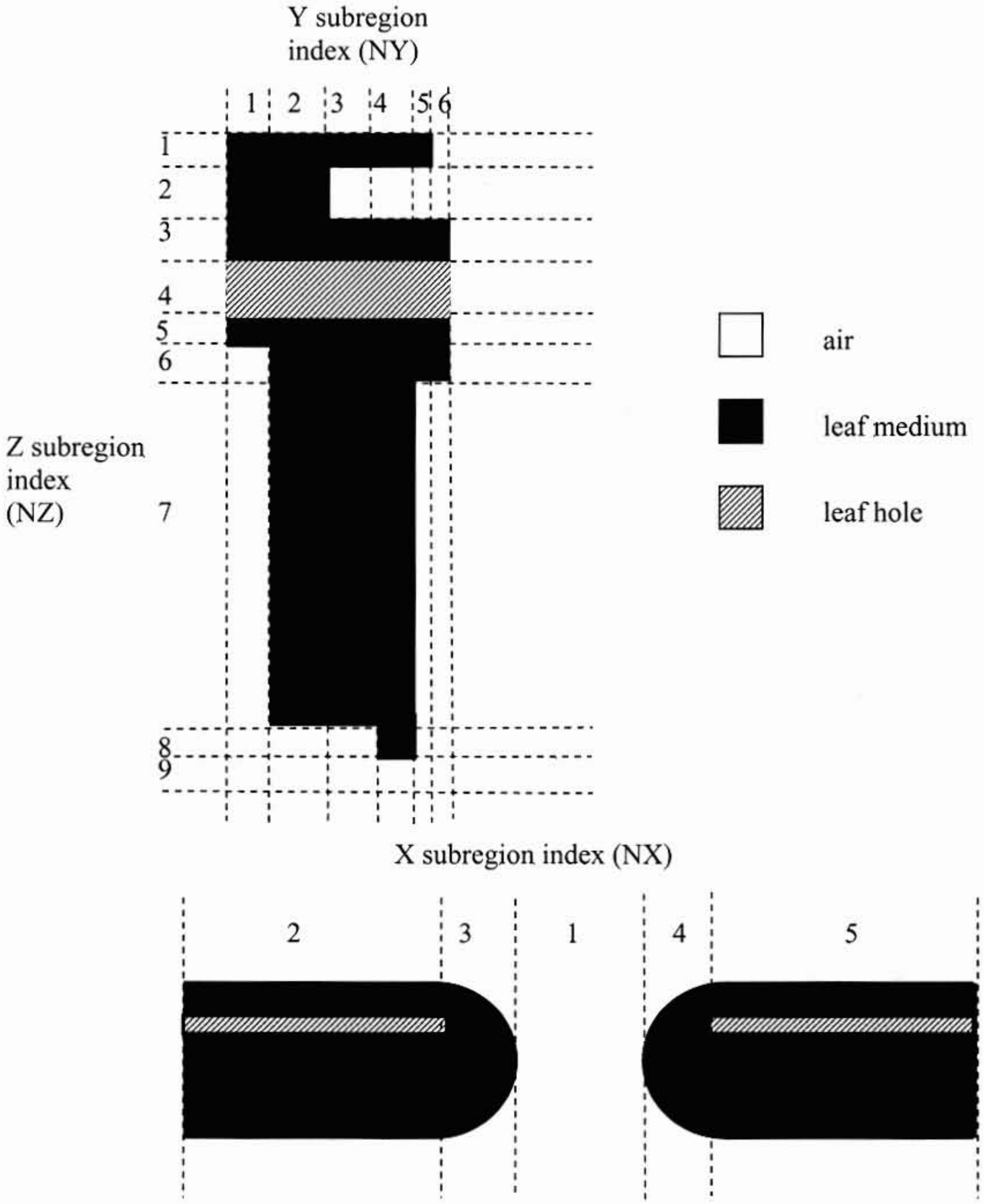

Figure 4-6: An example of subregion assignment for a target leaf. Each subregion is bound by a set of planes in the X,Y and Z directions. The direction of leaf motion is in the X direction. The planes in the Y direction are divergent with their focus at the target.

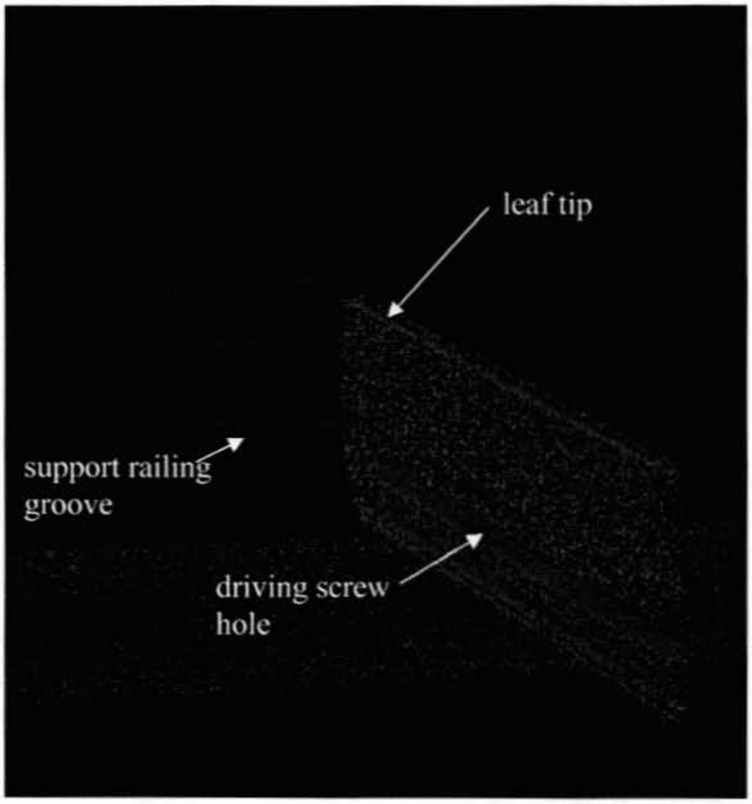

Figure 4-7: Ray tracing of an isocenter leaf pair showing the supporting rail groove, leaf tip and driving screw hole.

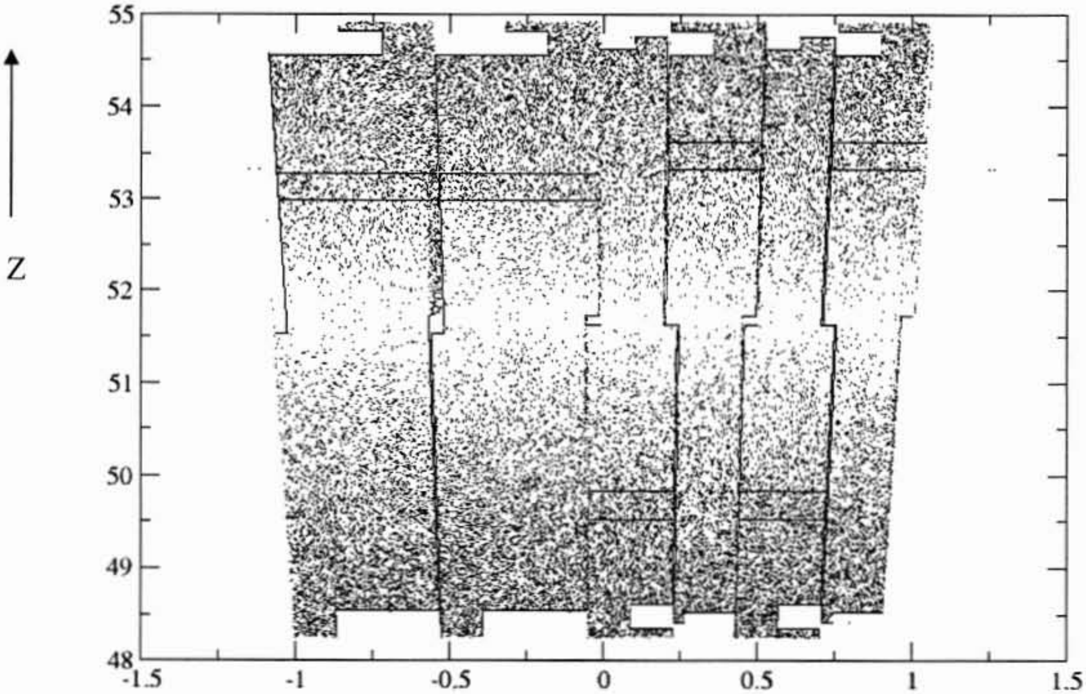

Figure 4-8: Two-dimensional projection of a ray tracing of two full leaves followed by two target/isocenter leaf pairs. The divergent leaf sides are shown (the focus is at Z=0) in addition to the vertical air gap between the tongue and groove of adjacent leaves.

4.5 Varian CL21EX accelerator model

A model of the Varian CL21EX linear accelerator incorporating the new DYNVMLC CM was built using the BEAMnrc[7] code. A diagram of the linear accelerator is shown in Figure 4-9, the MLC is not visualized but would be located below the secondary collimating jaws with the leaves oriented so that their direction of motion is parallel to the X jaws. The dimensions, location and composition of each component were obtained from the manufacturer. A pencil beam of electrons is incident on the front face of the target located at the origin of the accelerator model. The medium between each component module was specified to be air.

The characteristics of the phase space obtained using such an accelerator model are very sensitive to correct selection of incident electron beam parameters such as mean energy

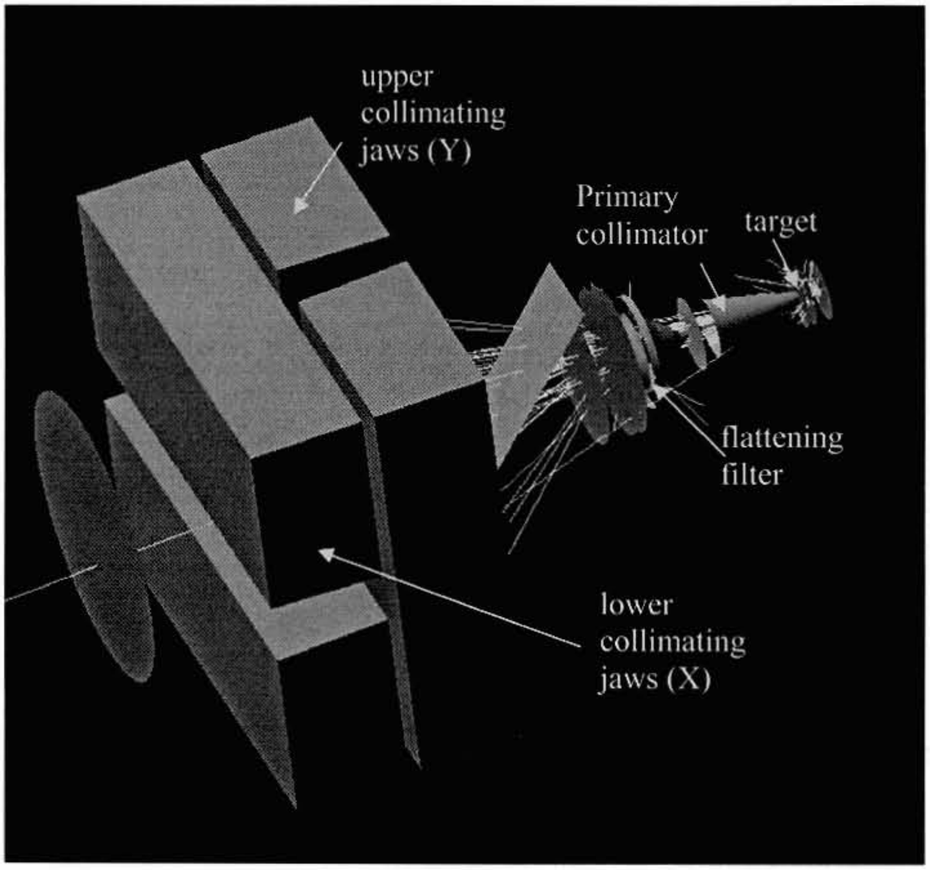

Figure 4-9: BEAMnrc model of CL21EX linear accelerator showing the trajectories of photons produced in the target. Also shown are the target, primary collimator, flattening filter, upper and lower collimating jaws. The MLC, not shown, is located below the X jaws.

and radial intensity distribution[8]. Accurate modeling of the materials and dimensions of each component such as the flattening filter is also critical. The accelerator model was validated by comparing simulated depth dose and off-axis profiles for a 10x10 cm^2 field with measured profiles.

A phase space file was simulated for a 10x10 cm^2 field assuming a 6 MeV incident electron beam having a Gausssian intensity distribution with a full-width at half maximum of 0.1 cm.. Photon and electron cutoff energies of 0.01 MeV and 0.700 MeV (including the rest mass), respectively, were specified and the phase space file was scored at a distance of 100 cm from the front face of the target. In the target, bremsstrahlung splitting with photon split number of 20 was used to increase the calculation efficiency. Approximately 435 million incident histories on the target were simulated to obtain 18 million particles in the phase space file. This phase space file was then applied to a water phantom, using the DOSXYZnrc user code, and depth dose and off-axis profiles were scored. The particles in the phase space file were re-used approximately 50 times to simulate 1 billion incident histories. A comparison of measured and simulated profiles is shown in Figure 4-10 and 4-11.

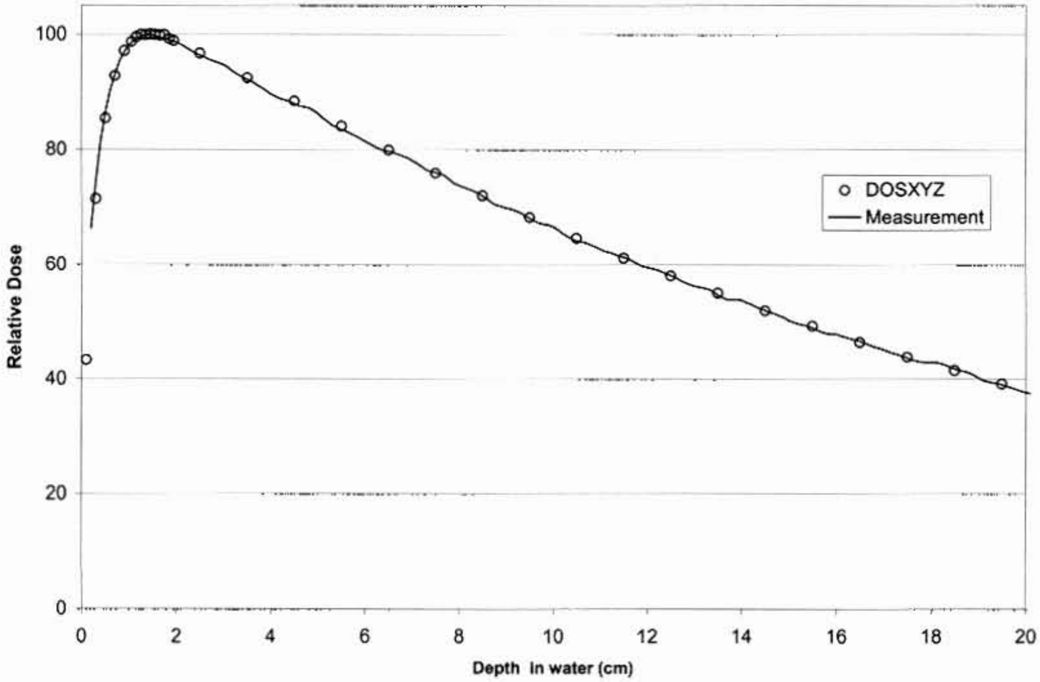

Figure 4-10: Comparison of measured and simulated 10x10 cm^2 6 MV depth dose profiles in water for a Varian CL21EX linear accelerator. The solid line indicates the measurement performed with an Exradin A14P microchamber and the open circles indicate the simulation performed with BEAMnrc/DOSXYZnrc.

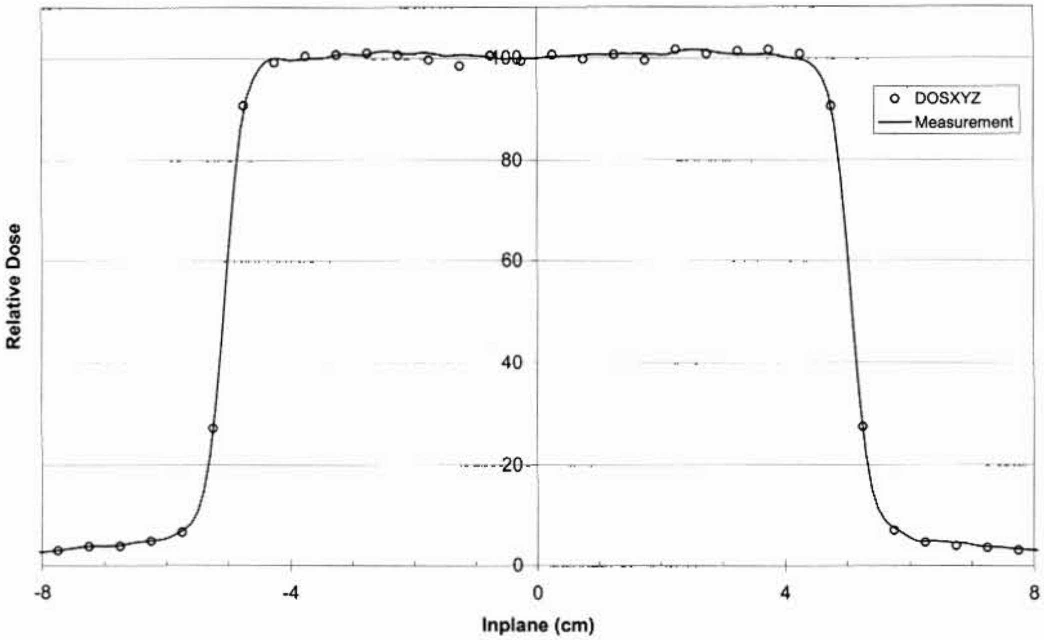

Figue 4-11: Comparison of measured and simulated 10x10 cm^2 6 MV inplane profile at a depth of 1.5 cm in water for a Varian CL21EX linear accelerator. The solid line indicates the measurement performed with an Exradin A14P microchamber and the open circles indicate the simulation performed with BEAMnrc/DOSXYZnrc.

4.6 MLC leakage validation

The leaf material density and abutting leaf air gap were chosen to match simulated MLC leakage profiles with measurements. The interleaf and abutting leaf leakage were measured using Kodak therapy verification XV-2 film (Kodak Inc., Rochester, NY) at a depth of 5 cm in Solid Water (Model 457, Gammex-RMI, Middleton, WI). A reference film was exposed to 100 MU for a 10x10 cm^2 field with the MLC leaves retracted. For measurement of the interleaf leakage, a second film was exposed to 5000 MU with the jaws open to 10x10 cm^2 and the MLC leaves blocking the field. A third film was exposed to 400 MU with the MLC leaves closed for measurement of the abutting leaf leakage. All films were scanned using a Therados FDM 7035 densitometer (Scanditronix, Uppsala, Sweden) in the orientations shown in Figure 4-12. The interleaf leakage profile was scanned at a 2 cm offset from the abutting leaves while the abutting leaf leakage profile was scanned under the centre of a leaf pair. A film calibration curve, shown in Figure 4-13, was obtained by measuring the optical density of a set of films exposed to doses ranging from 0 to 120 cGy. The calibration curve was used to convert the optical density of each scanned profile to dose and the ratio of the blocked field dose profile to the average open field dose was calculated.

A 10x10 cm^2 blocked field was simulated using the BEAMnrc model of the CL21EX linear accelerator, incorporating the Millenium 120 leaf collimator, with the measured 0.0057 cm interleaf air gap with the abutting leaf air gap ranging from 0 cm to 0.1 cm and the leaf density ranging from 16.94 g/cm^3 to 19.3 g/cm^3. Approximately 1 billion incident histories on the target were simulated to obtain 1 million particles in the phase space file. Photon and electron cutoff energies of 0.01 MeV and 0.700 MeV, respectively, were specified and bremsstrahlung splitting was used to improve the calculation efficiency. Profiles at a depth of 5 cm in Solid Water were simulated using DOSXYZnrc at the same locations. The particles in phase space file were re-used 200 times to simulate 200 million incident histories on the Solid Water phantom.

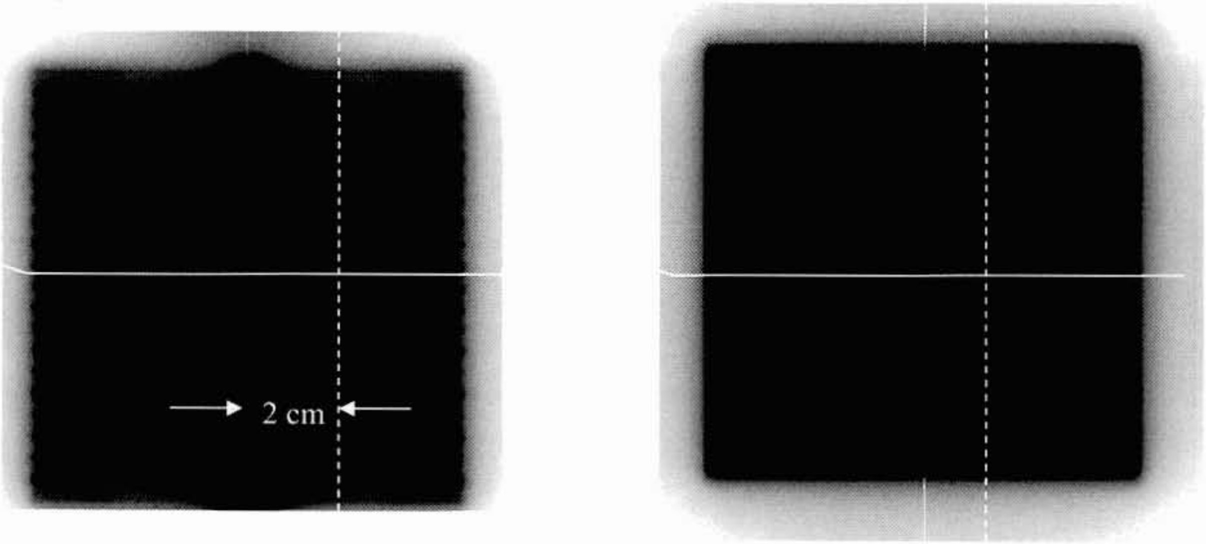

Figure 4-12: Film measurements of MLC leakage for 6 MV at 5 cm depth in Solid Water. The dashed line indicates the location of the interleaf leakage profile measurement and the solid line indicates the location of the abutting leaf leakage measurement.

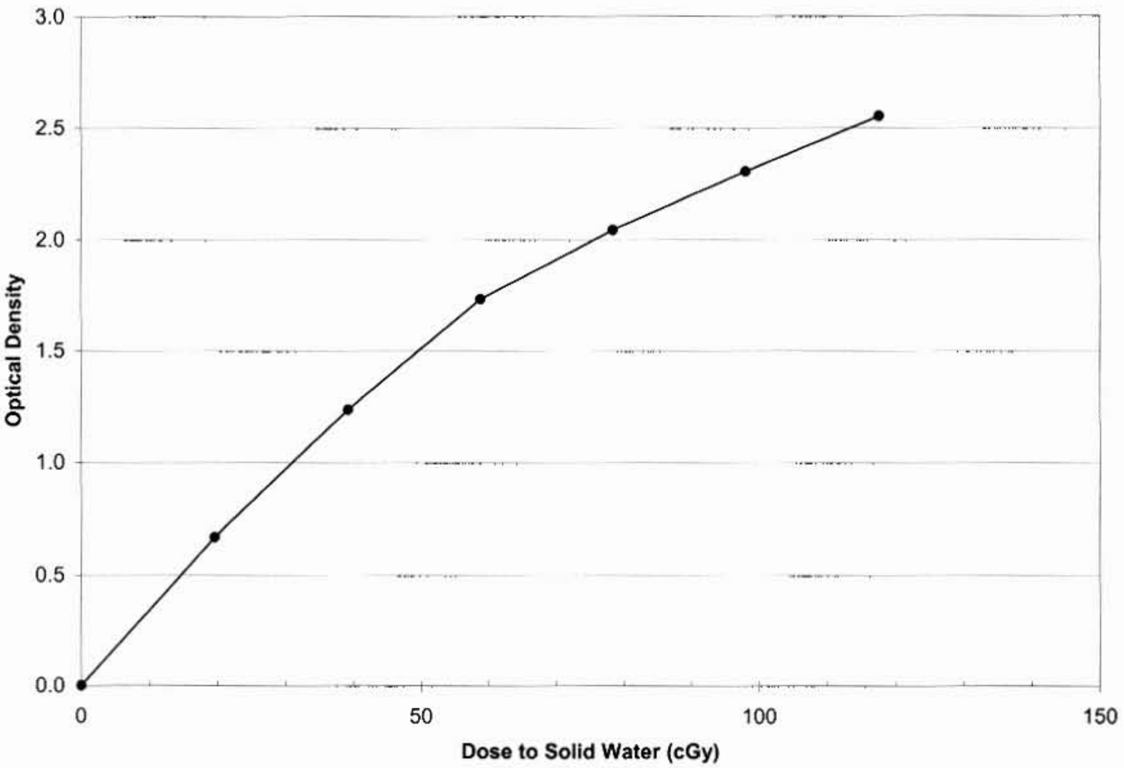

Figure 4-13: Calibration curve for Kodak therapy verification XV2 film obtained by irradating a series of films at a depth of 1.5 cm in Solid Water to doses ranging ranging from 0 to 120 cGy.

An X-Y plot of the transmitted radiation in the blocked field phase space file is shown in Figure 4-14. The high intensity region along the central axis is due to the abutting leaf leakage while areas of high intensity between adjacent leaves correspond to the interleaf leakage. There is also a reduction in transmitted intensity approximately 3 cm from the central axis which is the projected limit of the leaf driving screw hole.

As shown in Figures 4-15 and 4-16, an abutting leaf gap of 0.004 cm and density of 18 g/cm^3 were found to provide best agreement between measured and simulated leakage profiles. The alternating height of the maxima in the interleaf leakage profile is due to the vertical offset of the inner leaves which leads to a variation in the height of the air gap between the tongue and groove of adjacent leaves. The average measured transmission through the inner leaves is 1.3% and the interleaf leakage varies from 1.4% to 1.6%. The differences between the measured and simulated interleaf leakage profiles are attributed to a combination of the statistical uncertainty in the BEAMnrc/DOSXYZnrc simulations, which was approximately ± 2% of the measured value, the measurement uncertainty and the possible need for further density optimization.

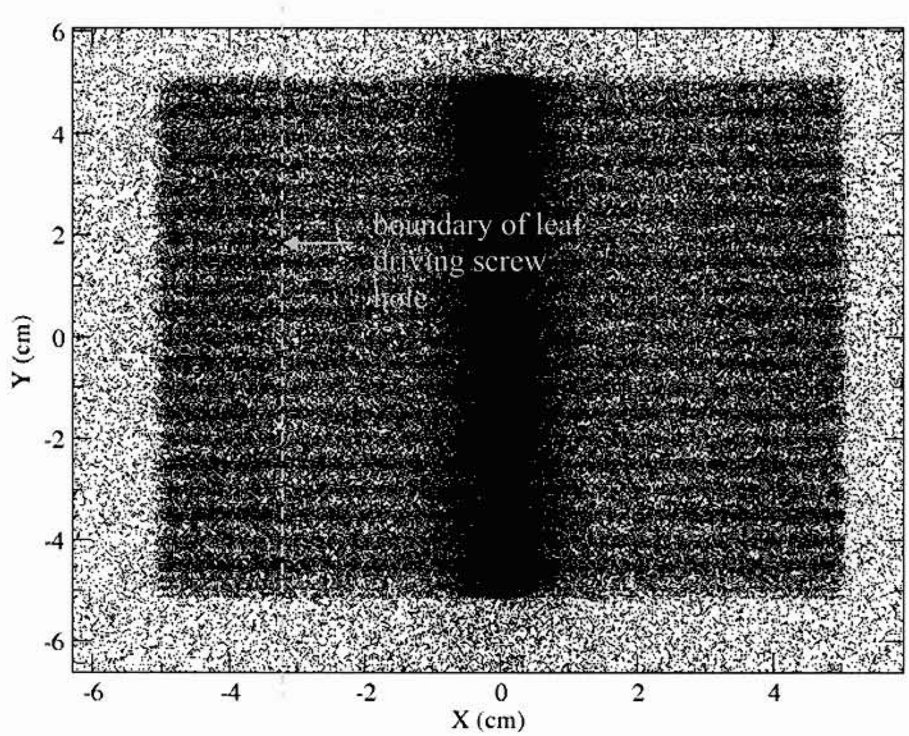

Figure 4-14: X-Y plot of transmitted radiation for a 10x10 cm^2 field with the MLC leaves blocking the field. The high intensity region at X=0 corresponds to the leakage between the abutting leafs. The alternating intensity along the Y direction corresponds to the interleaf leakage. A reduction in the transmitted intensity at approximately 3 cm corresponds to the extent of the leaf driving screw hole.

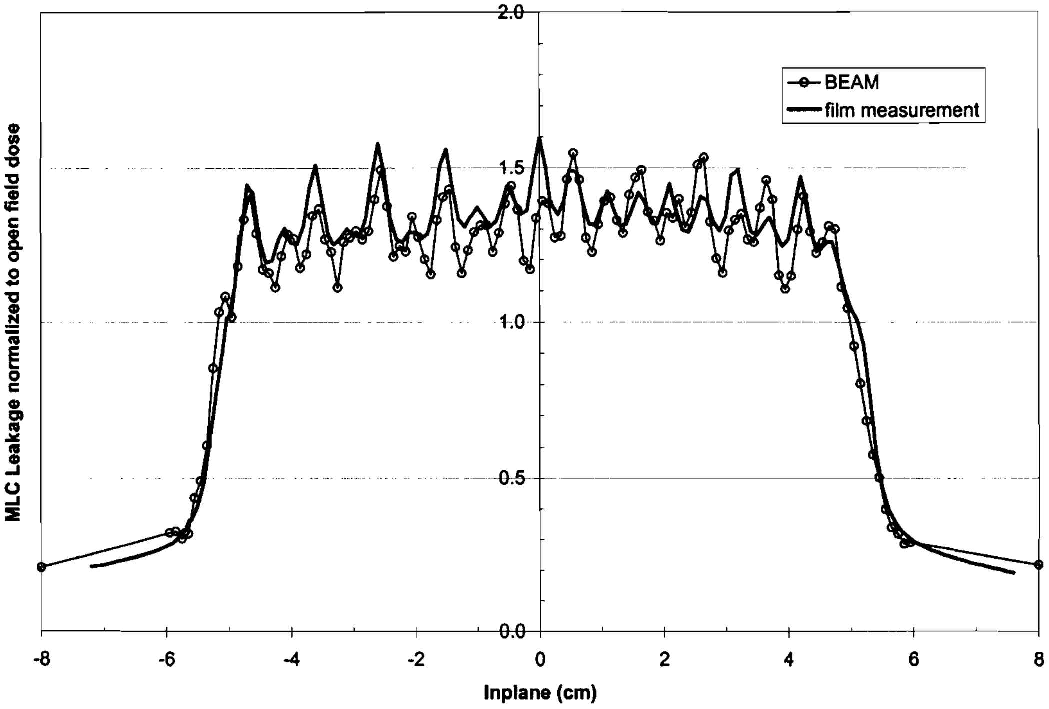

Figure 4-15: A comparison of measured and simulated 6 MV 10x10 cm^2 interleaf leakage profiles at a 2 cm offset from the central axis at a depth of 5 cm in Solid Water. The leaf material density is 18.0 g/cm^3 for the BEAMnrc simulation.

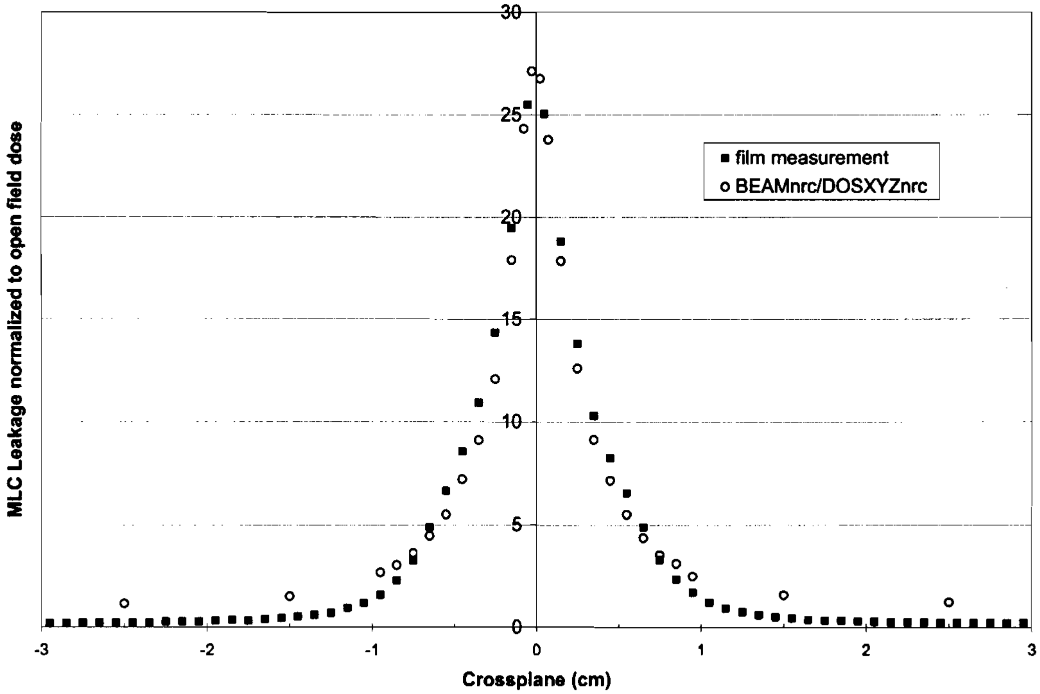

Figure 4-16: A comparison of 6 MV abutting leaf leakage profiles for a 10x10 cm^2 blocked field at a depth of 5 cm in Solid Water. The abutting leaf air gap is 0.004 cm for the BEAMnrc simulation.

The measured leakage between the abutting leaf is 26%. The uncertainty in the simulated profile is within ± 2% of the measured value. The resolution of the film measurement is limited by the 1 mm step size used for scanning the film. The discrepancies between the width of the measured and simulated abutting leaf leakage peak may be explained by uncertainty in the film positioning. A small offset in the position of the profile along the inplane direction, perpendicular to the direction of leaf motion, results in a wider peak due to increased contributions from the interleaf leakage. Another possible explanation is that the MLC leaf ends are not exactly rounded, as was assumed in the model. The underestimation of the measured leakage dose away from the abutting leaf gap seen in Figure 4-16 is attributed to the insufficient dose delivered to this portion of the film. At very low doses the film response is non-linear. Due to a combination of the limited dose range of the XV2 film and an approximate factor of 20 difference between the magnitudes of the interleaf and abutting leaf leakage, it is not possible to simultaneously obtain an optimum optical density for the portion of the film underneath the leaves without saturating the film in the region under the abutting leaf gap. This limitation could be overcome with the use of a film with an extended dose range, such as Kodak EDR2 which saturates at a dose of approximately 700 cGy compared to a saturation level of 200 cGy for XV2 film[9].

4.7 Summary

Modifications were made to the existing VARMLC component module in BEAMnrc to model the Varian Millenium 120 leaf collimator. This new component module, which we call DYNVMLC, models the geometry of the three leaf types found in the 120 leaf MLC. A model of the Varian CL21EX linear accelerator, including the 120 leaf MLC, was built using BEAMnrc and the MLC model was validated by selecting the leaf density and abutting leaf gap to match simulated leaf leakage profiles with film measurements performed at a depth of 5 cm in Solid Water. Dose distributions calculated using this accelerator model are then compared with PEREGRINE, as described in Chapter 5.

4.8 References

[1] AAPM Task Group No. 50, "Basic applications of multileaf collimators," AAPM Report No. 72, American Association of Physicists in Medicine (2001).

[2] J.R. Palta, D.K. Yeung and V. Frouhar, "Dosimetric considerations for a multileaf collimator system," Med. Phys **23**, 1219-1224 (1996).

[3] A.L. Boyer and S. Liu, "Geometric analysis of light-field position of a multileaf collimator with curved ends," Med. Phys. **24**, 757-762 (1997).

[4] M.S. Huq, I.J. Das, T. Steinberg and J.M. Galvin, "A dosimetric comparison of various multileaf collimators," Phys. Med. Biol. **47**, 159-170 (2002).

[5] A. Kapur, C.M. Ma and A.L. Boyer, "Monte Carlo simulations for multileaf collimator leaves: design and dosimetry," *Proc. Chicago 2000 World Congress on Medical Physics and Biomedical Engineering* (2000).

[6] D.W.O. Rogers, C.M. Ma, G.X. Ding and B. Walters, "BEAMnrc Users Manual," NRCC Report PIRS-0509(A), National Research Council of Canada, 1996.

[7] D.W.O. Rogers, B.A. Faddegon, G.X. Ding, C.M Ma and J.We, "BEAM: A Monte Carlo code to simulate radioatherapy treatment units," Med. Phys. **22**, 503-524 (1995).

[8] D. Sheikh-Bagheri and D.W. Rogers, "Sensitivity of megavoltage photon beam Monte Carlo simulations to electron beam and other parameters," Med. Phys. **29**, 379-390 (2002).

[9] X.R. Zhu, P.A. Jursinic, D.F. Grimm, F. Lopez, J.J. Rownd and M.T. Gillin, "Evaluation of Kodak EDR2 film for dose verification of intensity modulated radiation therapy delivered by a static multileaf collimator," Med. Phys. **29**, 1687-1692 (2002).

Chapter 5:

Equipment and Experimental Techniques

5.1 Introduction

In this chapter we describe the experimental method used to evaluate the PEREGRINE Monte Carlo code for 6 MV photons in homogeneous and heterogeneous phantoms. All measurements and Monte Carlo simulations were carried out for the 6 MV beam of a Varian CL21IEX linear accelerator at a source to surface distance (SSD) of 100 cm and a dose rate of 300 MU/min. The output of the linac has been calibrated, using the TG-51 protocol[1], to provide a dose of 101 ± 2 cGy/100 MU at a reference depth of 1.5 cm and field size of 10x10 cm^2 defined at 100 cm SSD.

First the characteristics of the various detectors used to measure profiles and output factors in the phantoms will be described. This is followed by a description of the measurement techniques as well as Monte Carlo simulations using PEREGRINE and EGSnrc. The detector response was investigated using Monte Carlo simulations of the measurements to examine how the presence of the detector in the medium perturbs the measured dose, particularly in the buildup region and in the heterogeneous phantoms.

5.2 Detectors

5.2.1 Exradin A14P microchamber

A diagram of the Exradin A14P parallel-plate microchamber (Standard Imaging, Middleton, WI) is shown in Fig 5-1. This waterproof chamber has a geometry similar to that of a cylindrical chamber but has been designed for use as a parallel-plate chamber. The outer shell, collecting electrode and guard electrode are composed of Shonka C552 air equivalent plastic. The point of measurement is defined to be at the back of the 1 mm thick entrance window[2]. The purpose of the two vent tubes is to maintain the chamber air volume in equilibrium with atmospheric pressure or allow filling of the chamber with a dielectric liquid for use as a liquid ionization chamber[3].

The 1 mm collector-window air gap and 1.5 mm diameter sensitive volume define a 0.002 cm^3 measuring volume which makes this chamber suitable for measurement of small fields. However, due to this small collecting volume, the measured signal is very small and the contributions of the "Compton" current, arising from particle interactions in the collector and chamber stem, are significant. Furthermore, as the chamber is designed to be used in a vertical orientation, additional currents arising from irradiation of the cable also contributes to a large polarity effect. For this study the Exradin chamber was used to measure dose profiles and output factors in water. To account for this polarity effect, for this study all measurements were taken as an average of readings at two polarities.

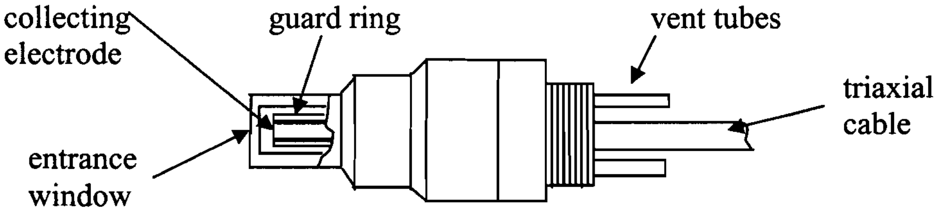

Figure 5-1: Diagram of Exradin A14P microchamber consisting of a 1.5 mm diameter cylindrical collecting electrode with concentric guard ring and an outer cylindrical shell with 1.5 mm entrance window[4].

5.2.2 Scanditronix NACP chamber

The NACP-02 chamber[5] (Scanditronix Medical AB, Sweden) is a waterproof parallel plate chamber which has an entrance window composed of a 0.1 mm mylar coating and a 0.5 mm thick graphite electrode. The body of the chamber is composed of Rexolite which has a density of 1.05 g/cm^3 and is considered to be a water equivalent plastic. There is a 2 mm air gap between the window and collecting electrode. The graphite collecting and guard electrodes have radii of 0.5 cm and 0.3 cm, respectively. The back plate of the chamber is also constructed of graphite for air equivalence. A diagram of the chamber is shown in Figure 5-2. The chamber was designed for measurement of electron beams while introducing minimal fluence perturbations. For this reason, in this study the NACP chamber was used for measuremet of dose profiles in the buildup region as well as measuring dose profiles in heterogeneous phantoms.

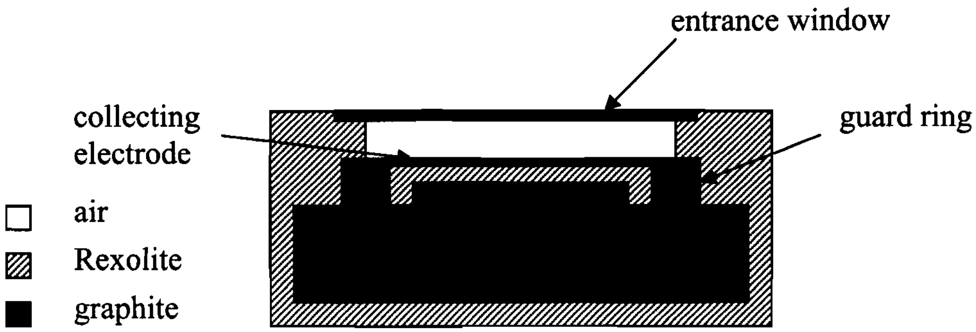

Figure 5-2: Schematic diagram of NACP parallel-plate chamber.

5.2.3 IC10 chamber

The IC10 cylindrical chamber (Wellhofer Dosimetrie, Schwarzenbruck, Germany) is a waterproof chamber with a 6 mm inner diameter and 3.3 mm long sensitive volume. The chamber wall and central electrode are constructed of air equivalent plastic Shonka C552. The effective point of measurement of this chamber is defined to be upstream from the central electrode at 0.6r where r is the radius of the chamber measuring volume[1]. The IC10 chamber is illustrated in Figure 5-3.

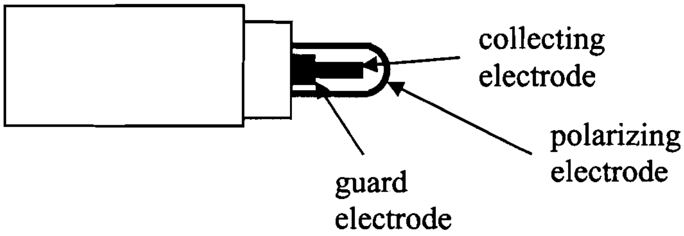

Figure 5-3: Schematic diagram of the IC10 cylindrical chamber showing the central collecting electrode, guard ring and polarizing electrode.

5.2.4 Thermoluminescent dosimeters (TLDs)

TLD-700 dosimeters (Harshaw Chemical Company, Solon, OH) have dimensions of 3.2 mm x 3.2 mm x 0.15 mm. These TLDs are composed of a lithium fluoride phosphor doped with magnesium, copper and phosphorus and have an effective atomic number of 8.2 and physical density of 2.64 g/cm^3. The percentage isotopic composition of lithium is 0.01 % ^{6}Li and 99.99% ^{7}Li. The TLDs are sensitive to photon and electrons with a useful dose range of 10 μGy to 10 Gy. The main TL peak of the glow curve occurs at 195 °C with a TL photon emitted with a wavelength in the range of 3500 – 6000 Å[6,7]. The small dimensions of these TLDs makes it possible to insert them into various phantom materials. Furthermore, the small thickness allows high resolution measurements along this dimension. In this study TLD-700 chips were used for measurement of dose inside the heterogeneous phantoms.

5.3 Homogeneous phantom measurement techniques

5.3.1 Depth dose, off-axis profiles and output factors

6 MV depth dose and off-axis phantoms were measured with the Exradin A14P chamber in a 60x60x60 cm^3 3D water phantom (Wellhofer Dosimetrie, Schwarzenbruck, Germany) on a Varian CL21EX linear accelerator. Measurements were made for collimator settings ranging from 2x2 cm^2 to 30x30 cm^2 at depths of 1.5, 5, 10, 20 and 30 cm with the field size defined by the collimating jaws and MLC leaves retracted. A polarizing voltage of 300 V was used and measurements were taken at two polarities and averaged. Depth dose profiles were shifted 0.1 cm in depth to account for the effective point of measurement of the chamber which is located behind the entrance window.

Output factors were measured at a depth of 15 cm in the water phantom for the above mentioned collimator settings. The chamber signal was measured with a Keithley Model 6517A electrometer (Keithley Instruments Inc., Cleveland, OH, USA) for both polarities and averaged.

5.3.2 Buildup region

The dose in the buildup region was measured with the NACP chamber in the 3D water phantom for a 10x10 cm^2 and 40x40 cm^2 collimator settings. The surface dose was measured with the chamber entrance window parallel to the water surface and the depth of measurement was shifted by +0.06 cm to correct for the effective point of measurement. Readings at both polarities were measured with the electrometer and averaged.

The dose in measured in the NACP detector was converted to dose to water using the Spencer-Attix cavity theory:

$$D_{med} = D_{\det}\left[\left(\frac{\bar{L}}{\rho}\right)^{med}_{\det}(d)\right]\bar{\Phi}^{med}_{\det}, \tag{5.1}$$

where $\left(\frac{\bar{L}}{\rho}\right)^{med}_{\det}(d)$ is the restricted stopping power ratio and $\Phi^{med}_{\det}$ is a term which corrects for the fluence perturbation introduced by the detector. Restricted stopping power ratios of water to air were calculated using the SPRRZnrc user code with an electron kinetic energy cutoff of 11 keV based on the average chord length of the chamber air cavity, which was calculated to be 2.9 mm. The fluence perturbation term will be discussed in a later section.

5.4 Homogeneous phantom Monte Carlo simulations

5.4.1 PEREGRINE

Open fields ranging in size from 2x2 cm^2 to 40x40 cm^2 were simulated with the jaws defining the field and the MLC leaves retracted. To avoid issues related to CT data such as beam hardening, image artifacts and non-distinct boundaries caused by voxels overlapping the medium boundaries, a mathematically defined phantom was used. The dimensions of the phantom were 50 cm x 50 cm x 30 cm with the CT number set to that of water throughout the phantom. The pixel size was 1 mm^2 and the slice thickness ranged from 1 to 4 mm.

A statistical quality factor of 0.2% was specified with each simulation requiring approximately 5 billion incident histories and 12 hrs of calculation time on a cluster of 16 800 MHz processors. The full CT resolution was set for the dose calculation resulting in a dosel radius of 2.7 mm and dose grid resolution of 3 mm. The calculated dose distributions were viewed on the CORVUS workstation and interpolated to the resolution of the CT images. Depth dose and off-axis profiles were extracted from the 3D dose distribution using the CORVUS 5.0 profile digitization tool.

To avoid averaging of the dose distribution over the CT grid in the CORVUS display, the buildup region dose was obtained directly from the PEREGRINE dose distribution file. A routine was written to read the dose distribution, which is in RTOG format[8], and extract dose profiles at a specified location within the phantom.

5.4.2 NACP chamber Monte Carlo study

To study how the fluence correction term of Equation (5.1) affects the measurement of the dose in the buildup region the geometry of the NACP chamber was simulated using the DOSRZnrc user code. The simulation geometry is shown in Figure 5-4. Using phase space files simulated for a 10x10 cm^2 and 40x40 cm^2 field the dose deposited in the chamber air cavity was simulated with the NACP chamber located at the water surface and at d_{max}. For each simulation 1 billion incident histories were used and an electron kinetic energy cut-off of 10 keV was specified. The dose deposited in the chamber air cavity D_{cav} can be directly related to the ionization Q and therefore the relative ionization should be equal to the relative cavity dose, as shown in Equation (5.2).

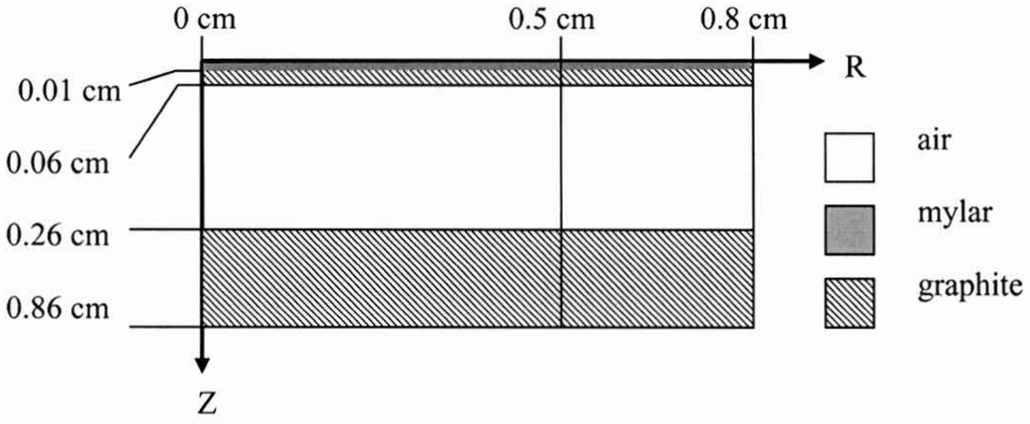

Figure 5-4: Geometry of NACP chamber simulation using the cylindrical geometry of DOSRZnrc user code.

$$D_{cav} = \left(\frac{Q}{m_{air}}\right)\left(\frac{W}{e}\right)_{air}, \tag{5.2}$$

$$\frac{D_{cav}(d)}{D_{cav}(d_{\max})} = \frac{Q(d)}{Q(d_{\max})}. \tag{5.3}$$

This relationship was used to test the accuracy of the EGSnrc simulations in the buildup region by comparing the simulated relative cavity dose with the measured relative cavity ionization. This approach was chosen to avoid issues related to detector response in the buildup region.

The perturbation correction term in Equation 5.1 was then derived by simulating depth dose curves in water using the same cut-off energies and number of incident histories as were employed in the cavity simulations. The correction factor was calculated as follows:

$$\Phi^{\det}_{water}(d) = \frac{D_{cav}(d)\left(\bar{L}/\rho\right)^{water}_{air}(d)}{D_{water}(d)} , \tag{5.4}$$

where $D_{cav}(d)$ is the simulated cavity dose at depth d and $D_{water}(d)$ is the simulated dose to water at the effective point of measurement when the chamber is position at depth d. The effective point of measurement was assumed to be on the inner surface of the entrance window. The ratio of restricted collision stopping powers $\left(\bar{L}/\rho\right)^{water}_{air}$ was calculated using SPRRZnrc.

5.5 Heterogeneous phantom measurement techniques

5.5.1 Composition of heterogeneous phantoms

Three heterogeneous phantoms, shown in Figure 5-5, were constructed consisting of 1 cm of Solid Water (Model 457, Gammex-RMI, Middleton, WI) followed by 3 or 5 cm of Equivalent Lung (Model 455, Gammex-RMI) or Bone (Model 450, Gammex-RMI) and an additional 20 cm of Solid Water. The composition of these materials is summarized in Table 5-1.

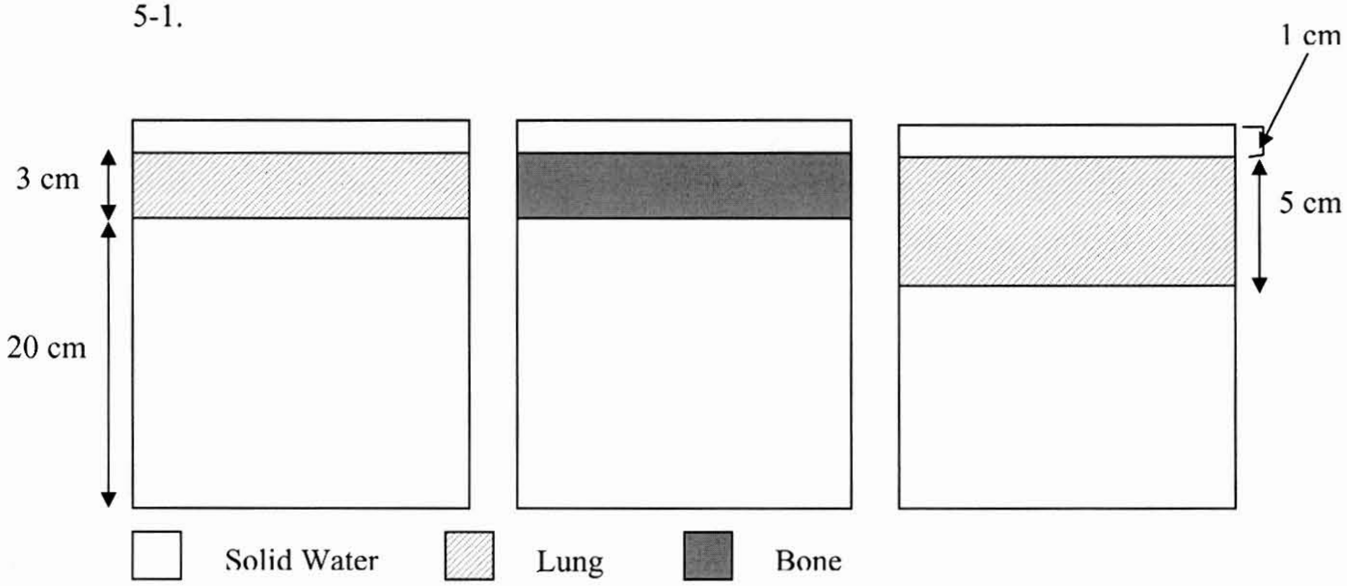

Figure 5-5: Configuration of three heterogeneous lung and bone phantoms.

Table 5-1: Percent composition by weight of water, lung and bone equivalent plastics (data obtained from Gammex-RMI, Middleton, WI).

Element	Solid Water RMI 457	Lung RMI 455	Bone RMI 450
H	8.09 %	3.1 %	8.62 %
C	67.22 %	31.26 %	68.87 %
N	2.4 %	0.99 %	2.26 %
O	19.84 %	37.57 %	17.62 %
Cl	0.13 %	0.05 %	0.11 %
Ca	2.32 %	27.03 %	2.52 %
physical density	1.035 g/cm^3	0.27 g/cm^3	1.84 g/cm^3
Z_{eff}	7.40	7.42	13.22
relative electron density	1.006	0.26	1.71

5.5.2 Conversion of dose to detector to dose in medium

The dose deposited in a detector is a function of the detector reading M_{det} and a calibration factor N_{det}:

$$D_{\text{det}} = M_{\text{det}} N_{\text{det}} \quad . \tag{5.5}$$

For the following measurements the calibration factor was determined from a measurement in a homogeneous solid water phantom at the reference depth of 1.5 cm. Using Equations (5.1) and (5.5) the detector reading is related to the dose in the medium $D_{SW}(cal)$ as follows:

$$D_{SW}(cal) = M_{\text{det}}(cal) N_{\text{det}} \left[\left(\frac{\bar{L}}{\rho} \right)_{\text{det}}^{SW} \Phi_{\text{det}}^{SW} \right]_{cal} \quad . \tag{5.6}$$

The dose to solid water at the reference point can be related to the calibration dose in water $D_w(cal)$ by the following relationship:

$$D_{SW}(cal) = K_{coll,SW} \beta_{SW} = \left[\left(\frac{\bar{\mu}_{ab}}{\rho} \right)_{w}^{SW} \beta_{w}^{SW} \right]_{cal} D_w(cal) \ , \tag{5.7}$$

where the factor β_w^{SW} was discussed in section 2.1.6 and $\left(\frac{\bar{\mu}_{ab}}{\rho}\right)_w^{SW}$ is the ratio of mass energy absorption coefficients. The calibration dose in water *D*$_w$*(cal)* is obtained from a measurement using a calibrated ionization chamber following the TG-51 protocol as follows[1]:

$$D_w^Q(cal) = M_{corr} N_{D,w}^{^{60}Co} k_Q \ , \tag{5.8}$$

where Q is the beam quality, M_{corr} is the chamber reading corrected for temperature and pressure, collection efficiency and polarity, $N_{D,w}^{^{60}Co}$ is the absorbed dose to water calibration factor in a Cobalt-60 beam and k_Q is the quality conversion factor which converts $N_{D,w}^{^{60}Co}$ to the beam quality Q. Using Equations (5.6) and (5.7) the calibration factor N_{det} can be derived:

$$N_{\mathrm{det}} = \left[\frac{D_w \left(\frac{\bar{\mu}_{ab}}{\rho}\right)_w^{SW} \beta_w^{SW}}{M_{\mathrm{det}} \left(\frac{\bar{L}}{\rho}\right)_{\mathrm{det}}^{SW} \Phi_{\mathrm{det}}^{SW}}\right]_{cal} . \tag{5.9}$$

This calibration factor may then be applied to measurement in the heterogeneous phantoms and using Equation (5.1) dose to the medium at any depth $D_{med}(d)$ is determined as follows:

$$D_{med}(d) = M_{\mathrm{det}}(d) N_{\mathrm{det}} \left[\left(\frac{\bar{L}}{\rho}\right)_{\mathrm{det}}^{med} (d)\right] \Phi_{\mathrm{det}}^{med}(d), \tag{5.10}$$

$$D_{med}(d) = M_{\mathrm{det}}(d) \frac{\left[\left(\frac{\bar{L}}{\rho}\right)_{\mathrm{det}}^{med} (d)\right] \Phi_{\mathrm{det}}^{med}(d) \left[D_w \left(\frac{\bar{\mu}_{ab}}{\rho}\right)_w^{SW} \beta_w^{SW}\right]_{cal}}{\left[M_{\mathrm{det}} \left(\frac{\bar{L}}{\rho}\right)_{\mathrm{det}}^{SW} \Phi_{\mathrm{det}}^{SW}\right]_{cal}} . \tag{5.11}$$

The restricted collision stopping power ratios were calculated using SPRRZnrc. The term $\left(\frac{\mu_{ab}}{\rho}\right)_w^{SW} \beta_w^{SW}$ was obtained from the ratio D_w^{SW} which was calculated from Monte Carlo simulations of the dose deposited at the reference depth in the homogeneous water and solid water phantoms. The fluence perturbation terms are discussed in a later section.

5.5.3 NACP chamber measurements

Depth dose profiles were measured beyond the bone/lung layer in each of the heterogeneous phantoms with the NACP chamber for a collimator setting of 10x10 cm^2. The chamber calibration factor was first determined by measurement of chamber reading at a depth of 1.5 cm in a homogeneous Solid Water phantom for a 10x10 cm^2 field. The stopping power ratios required for Equation (5.11) were calculated using the SPRRZnrc user code using an electron kinetic energy cut-off of 11 keV and the fluence perturbation terms were assumed to be unity.

5.5.4 TLD measurements

Measurement of dose inside the heterogeneous layer was performed using TLD-700 dosimeters. The TLD measurement procedure is defined in Figure 5-6.

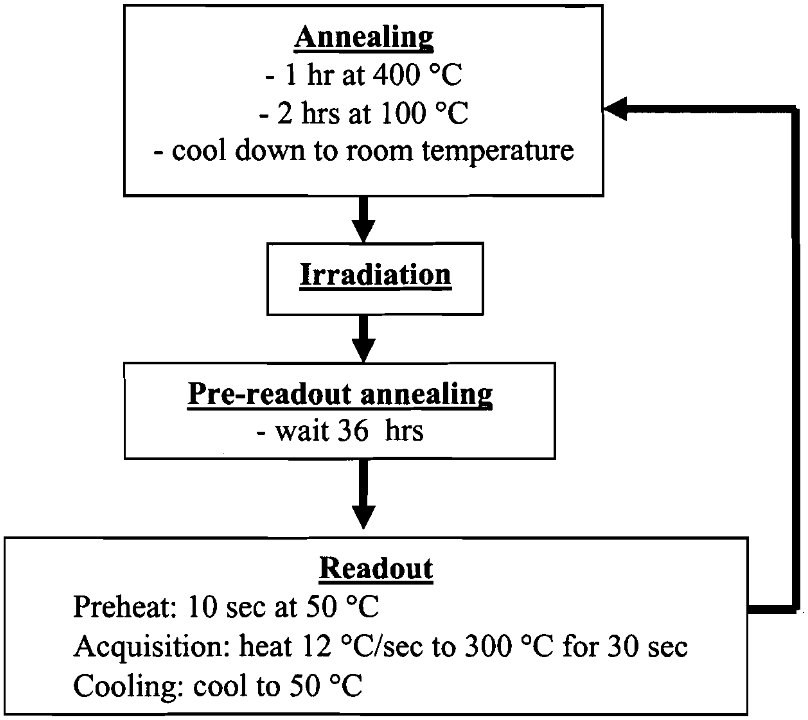

Figure 5-6: TLD measurement procedure.

. To remove any stored charge the TLDs were annealed in a computer controlled oven (PTW, Freiburg, Germany) using a programmed heating cycle of 400°C for 1 hour, followed by 2 hrs at 100 °C and subsequently cooled to room temperature. The TLDs were then irradiated and a 36 hour waiting period was observed to reduce the size of the low temperature peaks. The TLDs were read with a Harshaw QS 3500 TLD reader (Harshaw Chemical Company, Solon, OH) by first pre-heating the TLDs to 50 °C, followed by acquisition of the TL signal while heating to 300 °C at a rate of 12 °C/sec and finally cooling the TLD back to 50 °C. The TLDs were read in a nitrogen atmosphere to reduce the size of the nonradiation-induced thermoluminescence peak

An initial test of the linearity of the TLD response was performed by exposing the TLDs in groups of four at a depth of 1.5 cm in a homogeneous Solid Water phantom for a 10x10 cm^2 field with doses ranging from 0 – 160 cGy. The TLD response as a function of delivered dose is shown in Figure 5-6. It can be seen that the response is linear is this dose range.

To investigate the reproducibility of the TLD response, multiple calibration measurements were performed and the TLD reading as a function of the total delivered dose was plotted for a single dosimeter as shown in Figure 5-8. A decrease in response of approximately 6% per Gy was observed and is assumed to be caused by radiation damage in the TLD crystal from exposure to high energy photons.

To account for the reduced sensitivity of the TLDs with cumulative dose a calibration measurement was performed before and after each measurement. The average of the measured calibration factors was used. Individual calibration factors were applied to each TLD to account for variation of sensitivity within the batch. The calibration process consisted of simultaneously exposing all the TLDs in a homogeneous Solid Water phantom at a depth of 1.5 cm to 100 MU for a 10x10 cm^2 field at 100 cm SSD. The correction factors described in Equation (5.9) were applied to the TLD readings to calculate the detector calibration factors.

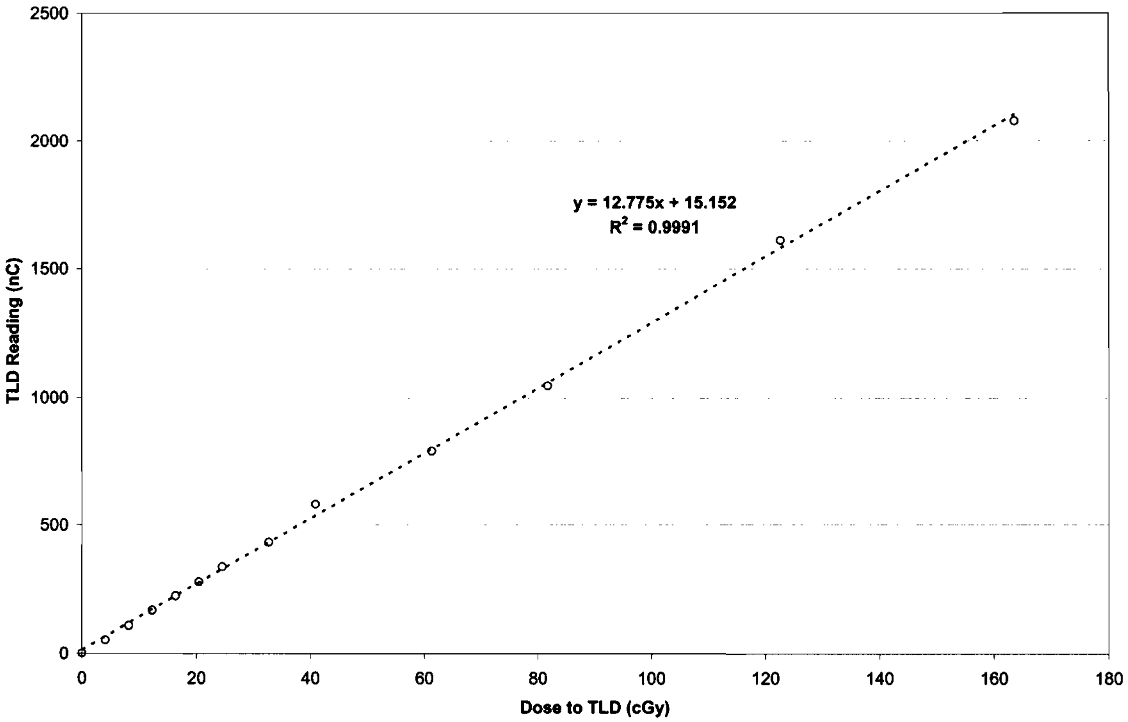

Figure 5-7: Test of linearity of TLD response as a function of dose to TLD for a single irradiation. Each point represents the average of readings for 4 TLDs.

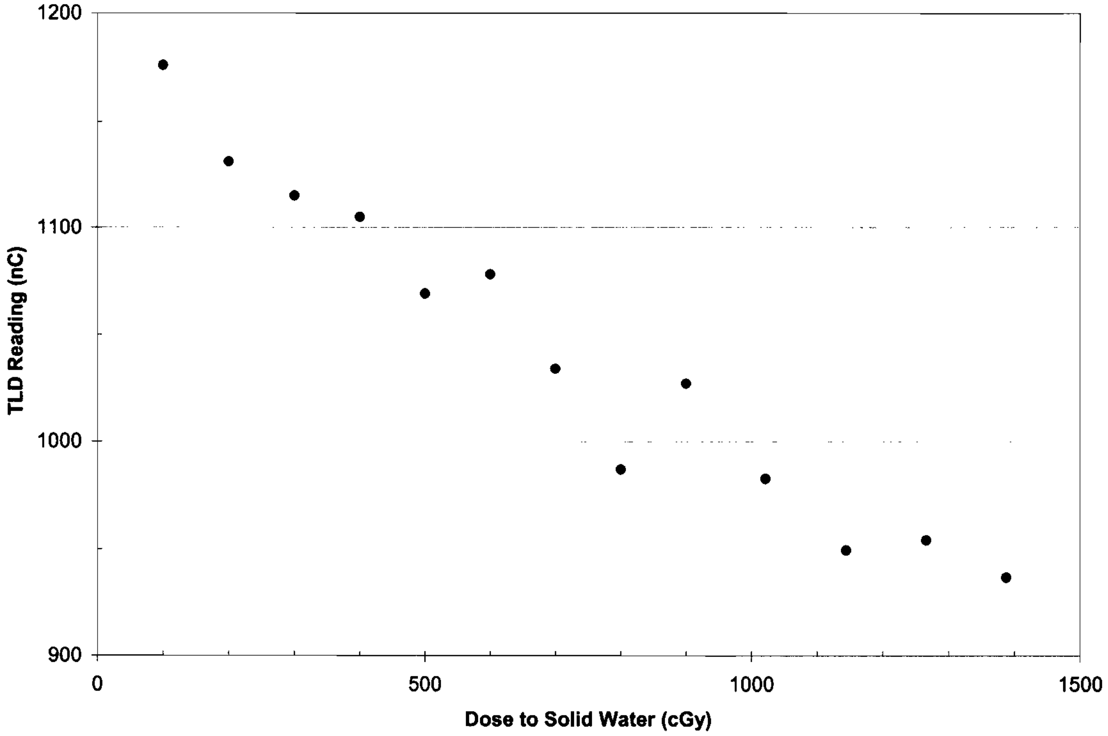

Figure 5-8: TLD response as a function of cumulative delivered dose for multiple calibration measurements.

Measurements of depth dose profiles in the heterogeneous phantoms was carried out by irradiating 4 TLDs simultaneously at each depth in the phantom to 100 MU for a collimator setting of 10x10 cm^2.

Stopping power ratios were calculated using the SPRRZnrc user code using an electron kinetic energy cutoff of 235 keV, based on the average chord length of the TLD being 0.3 mm, and Equation (5.11) was applied to convert each TLD reading to dose in the medium. The fluence perturbation corrections are discussed in Section 5.6.3.

5.6 Heterogeneous phantom Monte Carlo simulations

5.6.1 BEAMnrc/EGSnrc

The phantoms illustrated in Figure 5-5 were simulated with the DOSXYZnrc user code using a phase space file for an open 10x10 cm^2 field. Cross-section data for the phantom materials were prepared using the data preparation package in PEGS4 based on the compositions described in Table 5-1. A billion incident histories were simulated for each phantom and depth dose profiles along the central axis were scored using voxel size of 1 cm x 1 cm x 0.2 cm. In the vicinity of the interfaces a 1 mm voxel height was used. The photon and electron cut-off energies were 10 keV and 700 keV, respectively.

5.6.2 PEREGRINE

Mathematical phantoms were defined to simulate the heterogeneous lung and bone phantoms. The CT numbers of the materials in each phantom were chosen to obtain the calculated electron densities in Table 5-1 based on the CT-to electron density calibration curve used in CORVUS. A statistical quality factor of 0.2% was specified and a dosel grid interval of 0.24 cm was used. Depth dose profiles were extracted using the CORVUS 5.0 dose profile digitization tool.

5.6.3 Monte Carlo study of TLD response

To investigate the fluence perturbation correction term Φ_{det}^{med} described in Equation (5.11), Monte Carlo simulations of the TLD measurements were performed using the DOSXYZnrc user code. A shown in Figure 5-9, the geometry of the calibration and heterogeneous phantoms were simulated with and without the TLDs present at the measurement depth. Photon and electron cut-off energies of 10 keV and 521 keV, respectively, were used. Fluence correction factors were calculated by dividing the simulated dose to the medium in the absence of the TLD, $D_{med}(d)$, by the product of the dose to the TLD in the medium, $D_{tld,med}(d)$, and the stopping power ratio of medium to TLD, $\left(\bar{L}/\rho\right)_{tld}^{med}$, at that point.:

$$\Phi_{tld}^{med} = \frac{D_{med}(d)}{D_{tld,med}(d)\left(\bar{L}/\rho\right)_{tld}^{med}(d)} \quad . \tag{5.12}$$

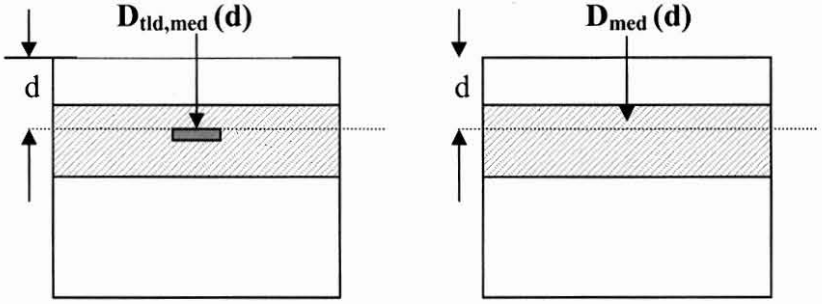

Figure 5-9: Geometry of DOSXYZnrc simulations of TLD measurements in calibration and heterogeneous phantoms.

5.7 Summary

In this chapter we have presented a description of the detectors and measurement techniques used for a comparison of PEREGRINE, measurements and the EGSnrc Monte Carlo code in homogeneous and heterogeneous phantoms. The results of this evaluation are presented and discussed in Chapter 6.

5.8 References

[1] P.R. Almond, P.J. Briggs, B.M. Coursey, W.F. Hanson, M.S. Huq, R. Nath and D.W.O. Rogers, "AAPM's TG-51 protocol for clinical reference dosimetry of high-energy photon and electron beams," Med. Phys. **26**, 1847-1870 (1999).

[2] IAEA, "The use of plane parallel ionization chambers in high energy electron and photon beams: an international code of practice for dosimetry," Technical Report series Vol. 381, International Atomic Energy Agency, Vienna (1997).

[3] P. Francescon, S. Cora, C. Cavedon, P. Schalchi, S. Reccanello and F. Colombo, "Use of a new type of radiochromic film, a new parallel-plate micro-chamber, MOSFETs, and TLD 800 microcubes in the dosimetry of small beams," Med. Phys. **25**, 503-511 (1998)

[4] H-R Lee, M. Pankuch, J.C. Chu and J. Spokas, "Evaluation and characterization of a parallel plate microchamber's functionalities in small beam dosimetry," Med. Phys. **29**, 2489-2496 (2002).

[5] Nordic Association of Clinical Physics, "Procedures in external radiation therapy dosimetry with electron and photon beams with maximum energies between 1 and 50 MeV," Acta Radiol. Oncol. **19**, 55-79 (1980).

[6] J.R. Cameron, N. Suntharalingam and G.N. Kenney, *Thermoluminescent Dosimetry*, (University of Wisconsin Press, Madison, 1968).

[7] A.F. McKinlay, *Thermoluminescence Dosimetry*, (Medical Physics Handbooks Vol 5, Adam Hilger Ltd, Bristol, 1981).

[8] Radiation Therapy Oncology Group, Philadelphia, PA.

Chapter 6:

Results and Discussion

6.1 Evaluation of PERGRINE in homogeneous water phantom

A comparison of depth dose and off-axis profiles in water for collimator settings ranging from 2x2 cm^2 to 30x30 cm^2 between PEREGRINE and measurements using the Exradin A14P chamber is shown in Figures 6-1 and 6-2.

The agreement between measured and calculated depth dose profiles is within 1% for all field sizes. Agreement between the measured and calculated off-axis profiles is also

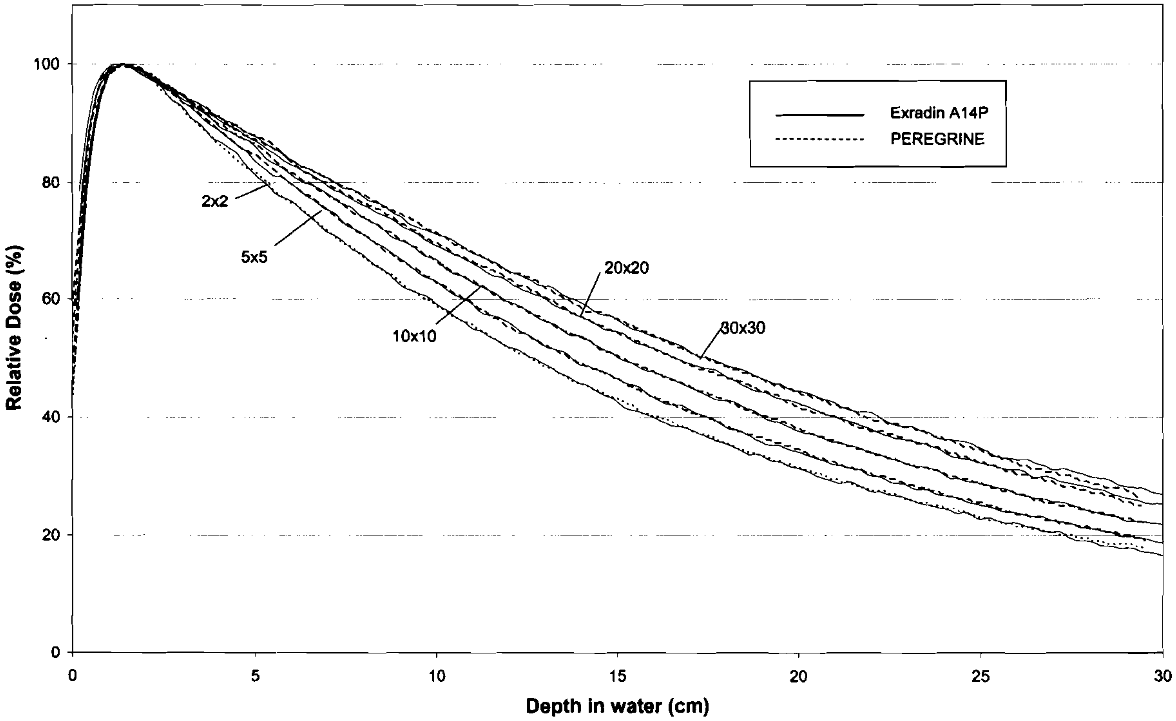

Figure 6-1: Comparison of 6 MV depth dose profiles in water for field sizes ranging from 2x2 cm^2 to 30x30 cm^2. The solid lines indicate measurements with Exradin A14P chamber while the dashed lines indicate PEREGRINE simulations.

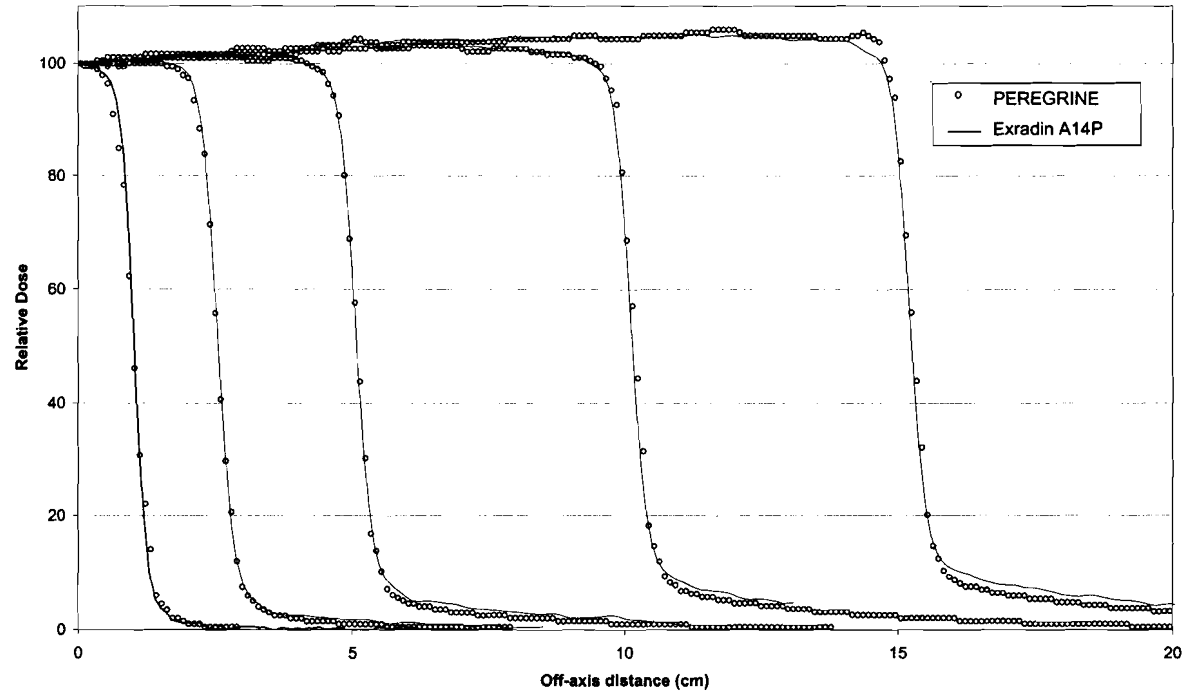

Figure 6-2: Comparison of 6 MV off-axis profiles at a depth of 1.5 cm in water for field sizes of 2x2 cm^2 to 30x30 cm^2. The solid lines indicate measurements with the Exradin A14P chamber while the open circles indicate PEREGRINE simulations.

within 1%, with some exceptions.

In the umbra region outside the field edges, for field sizes of 10x10 cm^2 and larger, PEREGRINE appears to underestimate the dose by 3% of the central axis value. This discrepancy may be related to uncertainty in the measurements due to the significant polarity effect of the Exradin A14P chamber. For the 30x30 cm^2 field in the umbra region the difference between the readings for the two polarities was 5% of the central axis dose. The polarity effect is more significant for these larger fields where there is more scattered radiation which interacts in the collecting electrode and cable. However, the magnitude of the polarity effect is not large enough to fully account for the discrepancy between the measurements and PEREGRINE. Discrepancies were also noted between the calculated and measured 30x30 cm^2 off-axis profiles, particularly at the field edge where PEREGRINE overestimates the dose by 3%. It appears that the PEREGRINE beam model does not accurately model the 30x30 cm^2 off-axis fluence. This, and the discrepancies in the umbra

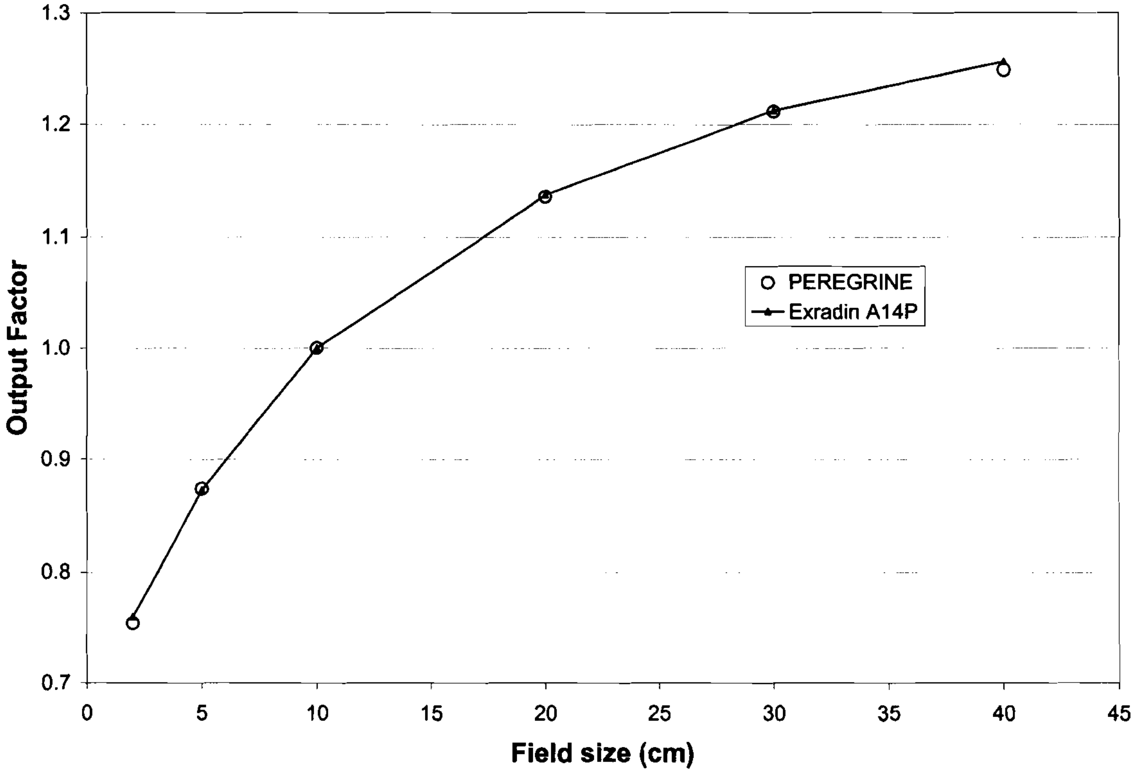

Figure 6-3: Comparison of 6 MV relative output factors measured at a depth of 15 cm in water for field sizes ranging from 2x2 cm^2 to 40x40 cm^2. The solid line indicates measurements with the Exradin A14P chamber while the open circles indicate PEREGRINE simulations.

region, could be related to incomplete modeling of a scattered photon or electron subsource in the PEREGRINE beam model, possibly due to an incorrect choice of radial cutoffs used to construct the set of correlated histograms describing the beam model subsources, or an underestimation of lateral scattering of electrons at the field edges by the electron transport algorithm implemented in PEREGRINE.

A comparison of output factors calculated by PEREGRINE and measurements in water for field sizes ranging from 2x2 cm^2 to 40x40 cm^2 is shown in Figure 6-3. The agreement between PEREGRINE and measurements is within 1%. Each measurement point represents the average of readings taken at two polarities with the Exradin A14P chamber. The statistical uncertainty of the measurements is within 0.1% of the measured value. The polarity correction was 16%, on average, for these measurements.

6.2 Evaluation of PEREGRINE in the buildup region

A comparison of dose in the buildup region calculated using PEREGRINE, BEAMnrc/DOSXYZnrc and measurements with the NACP chamber is shown in Figures 6-4 and 6-5 for 10x10 cm^2 and 40x40 cm^2 fields, respectively.

The NACP measurements are in good agreement with the BEAMnrc/DOSXYZnrc simulations except near the surface where the NACP chamber appears to overestimate the surface dose by up to 13%. The positional uncertainty on the measurements is ± 0.2 mm which can be translated into a dose uncertainty of ± 2%. The DOSRZnrc simulations of the dose deposited in the measuring volume of the chamber, as described in Section 5.4.2, predict a relative cavity dose of 45 ± 1% and 67 ± 2% at the surface for the 10x10 cm^2 and 40x40 cm^2 fields. The measured relative ionization for these fields is 47 ± 2% and 69.0 ± 0.3%. The excellent agreement between the predicted and measured ionization indicates that the observed discrepancy is due to an overresponse of the NACP chamber and that the results obtained using EGSnrc/DOSXYZnrc in the buildup region are accurate.

The overresponse of the NACP chamber in the buildup region can be explained by electrons which are scatterred into the lower density air cavity from the chamber walls[1]. These electrons originate either from photon interactions in the wall and medium surrounding the chamber, or as contaminant electrons in the incident radiation beam. The amount of scattered electrons is dependent on the size of the air cavity, with the amount of in-scatter increasing with increasing cavity size. The width of the guard ring will also determine how many of these scattered electrons will reach the sensitive volume of the chamber. For a 6 MV photon beam, assuming a mean photon energy of 2 MeV, the energy of an electron scattered through an angle of 45° is approximately 1 MeV. The 2 mm wide guard ring in the NACP chamber is not adequate to prevent these electrons from reaching the collecting electrode. Another possible source of the chamber overresponse is backscattering of electrons from the 5 mm thick graphite backplate. The higher density of graphite (1.8 g/cm^3) compared to water leads to a larger amount of backscatter than would occur if this backplate was replaced by water[2].

In the buildup region, where a steep gradient exists in the electron fluence across the chamber gap, charged particle equilibrium is not achieved and these in-scatterred electrons are not compensated by electrons scattered out of the chamber air cavity.

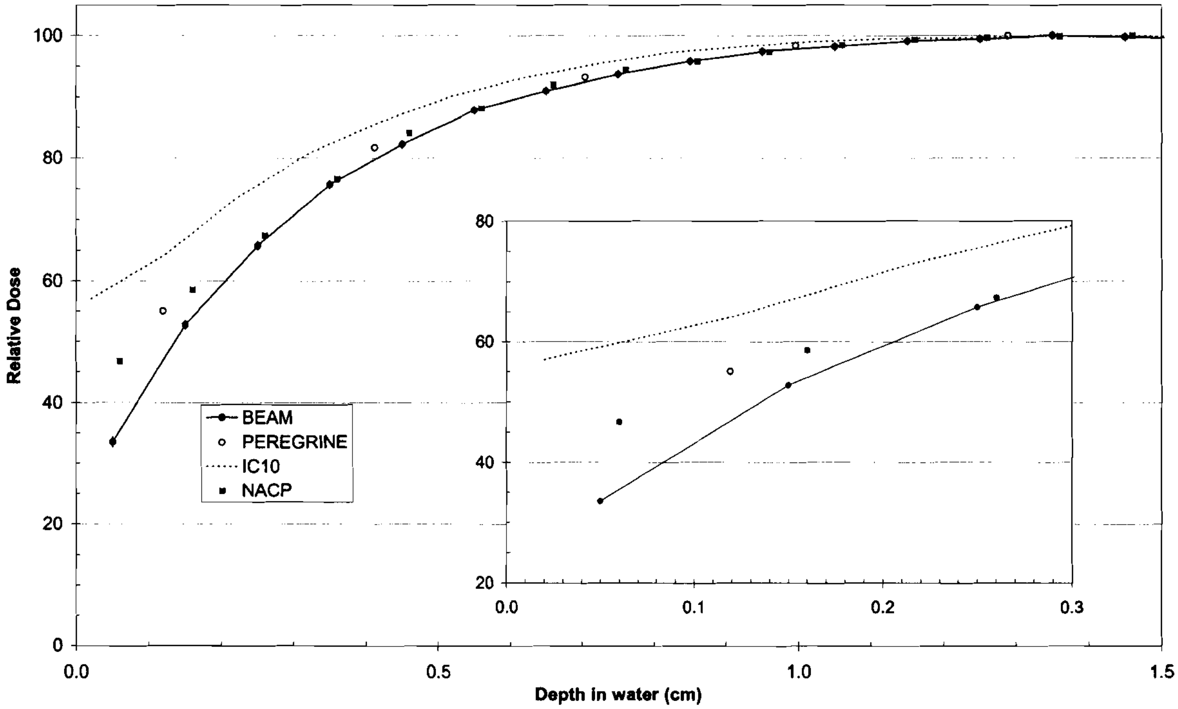

Figure 6-4: Comparison of 6 MV buildup region dose for a 10x10 cm^2 field in water. The solid line indicates BEAMnrc/DOSXYZnrc simulation, open circles indicate the PEREGRINE simulation, the dashed line indicates IC10 measurement and the filled squares represent NACP measurements.

Therefore it is necessary to apply a perturbation correction factor to the measured dose when applying the Spencer-Attix cavity theory as outlined in Equation (5.1). The source of this perturbation correction is two-fold, the previously mentioned fluence perturbations introduced by the chamber and a gradient correction factor which is related to uncertainty in the location of the effective point of measurement of the chamber when measuring in the buildup region.

The perturbation corrections for the 10x10 cm^2 field were calculated to be 1.28 ± 0.02 and 1.010 ± 0.008 at the surface and d_{max}, respectively, assuming the effective point of measurement to be on the inside surface of the entrance window of the NACP chamber. It can be seen that the correction factor approaches unity at d_{max} when CPE conditions are achieved.

In comparison to EGSnrc, PEREGRINE appears to overestimate the dose near the surface by as much as 13%. During the initial dosimetric validation of PEREGRINE simulations of dose in the buildup region were compared with measurements using an IC10 cylindrical chamber. In comparison with measurements, PEREGRINE appeared to underestimate the surface dose by approximately 10%. Based on an observation that the discrepancy increased with increasing field size and was not present for fields blocked by a wedge Hartmann-Siantar et al concluded that the source of the discrepancy was a deficit in the number of contaminant electrons reaching the phantom surface[3]. To compensate for this discrepancy the weight of the electron subsource in the beam model was increased by 120% for the 6 MV source model.

An IC10 chamber measurement has been included in Figures 6-4 and 6-5 to illustrate how it significantly overestimates the dose in the buildup region. This overestimation is due to in-scatterring of electrons into the measuring volume. The perturbation correction is more significant for cylindrical chambers than for parallel-plate chambers, especially in the buildup region, due to lack of guarding and a less well defined effective point of measurement. It is therefore necessary to apply a correction factor which is dependent on the inner diameter of the chamber[4]. It is interesting to note that the PEREGRINE simulations based on the unmodified source model agreed within 1% with simulations based on phase space files generated with BEAMnrc. It can therefore be concluded that at 6 MV the discrepancies observed between the original source model and measurements were due to issues of chamber response in the buildup region.

Similar discrepancies between Monte Carlo simulations, using PEREGRINE and BEAMnrc, and measurements have been noted in the buildup region for 18 MV photon beams[3,5]. This discrepancy is larger than that for 6 MV photons and cannot be fully accounted for by ion chamber response issues which has led some authors to speculate whether the discrepancy is due to the failure of the EGSnrc code to fully model the photon beams produced by linear accelerators. These studies have included investigations of whether contributions from neutrons, which are not modeled by the EGSnrc code, or an unaccounted source of electrons within the accelerator head are responsible for this underestimation[6,7]. To date, these discrepancies remain unresolved.

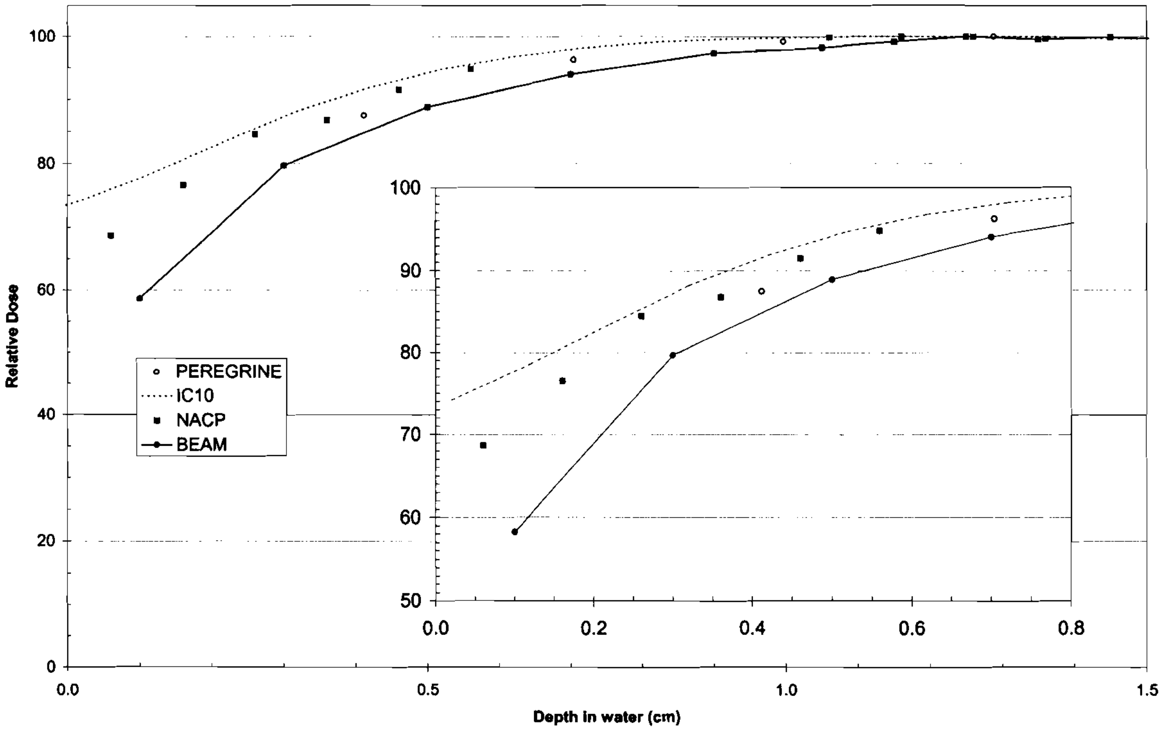

Figure 6-5: Comparison of 6 MV buildup region dose for a 40x40 cm^2 field in water. The solid line indicates BEAMnrc/DOSXYZnrc simulation, open circles indicate the PEREGRINE simulation, the dashed line indicates IC10 measurement and the filled squares represent NACP measurements.

6.3 Evaluation of PEREGRINE in heterogeneous phantoms

A comparison of measured and calculated 6 MV depth dose profiles in the heterogeneous phantoms for a collimator setting of 10x10 cm^2 is shown in Figures 6-6 through 6-9.

Measurements with the NACP chamber agree with EGSnrc/DOSXYZnrc within 1%. The agreement of TLD measurements is within 3% with slightly better agreement obtained for the 5 cm lung phantom where the measurements were repeated 3 times so that each point represents the average of 12 TLD readings. The statistical uncertainty of the TLD measurements was 1.3% on average and ranged up to 6.2% for some depths. Fluctuations in the output of the linear accelerator between the calibration and measurement irradiations, changes in the temperature of the annealing and readout cycles, photomultiplier tube

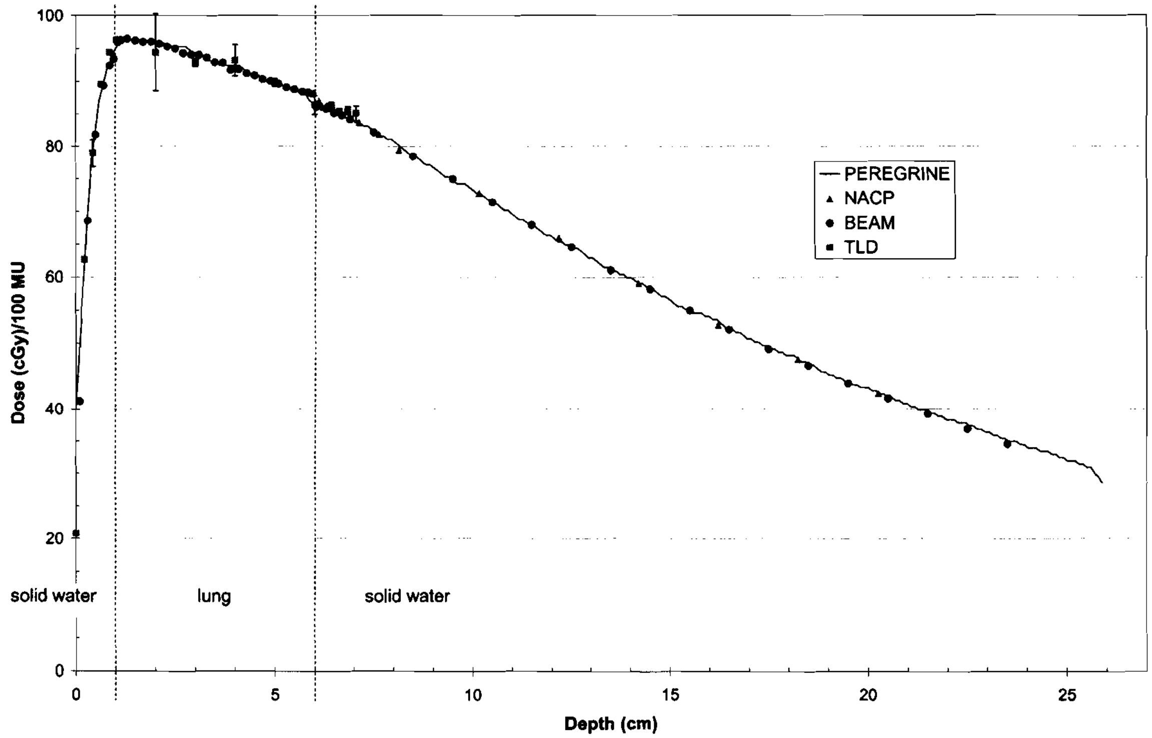

Figure 6-6: Comparison of 6 MV 10x10 cm^2 depth dose profiles in a solid water phantom containing a 5 cm slab of lung equivalent plastic. The solid line indicates PEREGRINE simulations, circles indicate BEAMnrc/DOSXYZnrc simulations, triangles indicated measurements with the NACP chamber and squares indicate measurements with TLD-700 chips. Each TLD measurement point represents the average of 12 readings.

response as well as contamination or damage of the TLDs from their handling all contribute to this uncertainty. The non-uniform composition of the lung equivalent plastic may also lead to a positional dependence of the dose deposited in the TLD within the lung material at a given depth.

The restricted stopping power ratios of medium to lithium fluoride were calculated to be, on average, 1.2081 ± 0.0003, 1.231 ± 0.002 and 1.0980 ± 0.0002 for the water, lung and bone equivalent plastics. The fluence correction term $\Phi_{\mathrm{det}}^{med}$ from Equation (5.11), calculated from DOSXYZnrc simulations of the TLD measurements, are summarized in Figure 6-7. In the calibration phantom a fluence correction of 0.992 ± 0.009 was calculated at a depth of 1.5 cm.

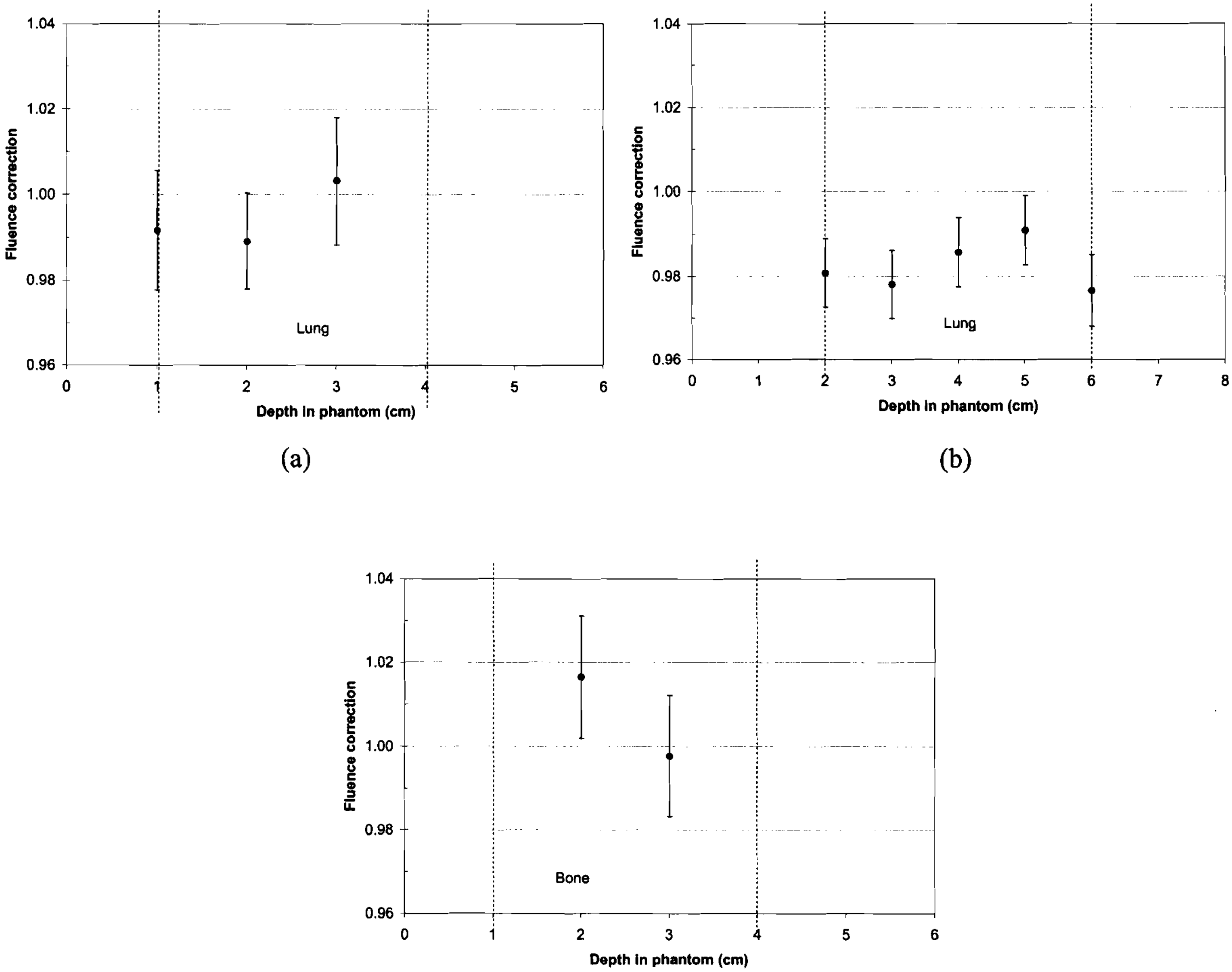

(a) (b)

(c)

Figure 6-7: Fluence corrections for TLD measurements at different depths in (a) 3 cm lung phantom (b) 5 cm lung phantom and (c) 3 cm bone phantom.

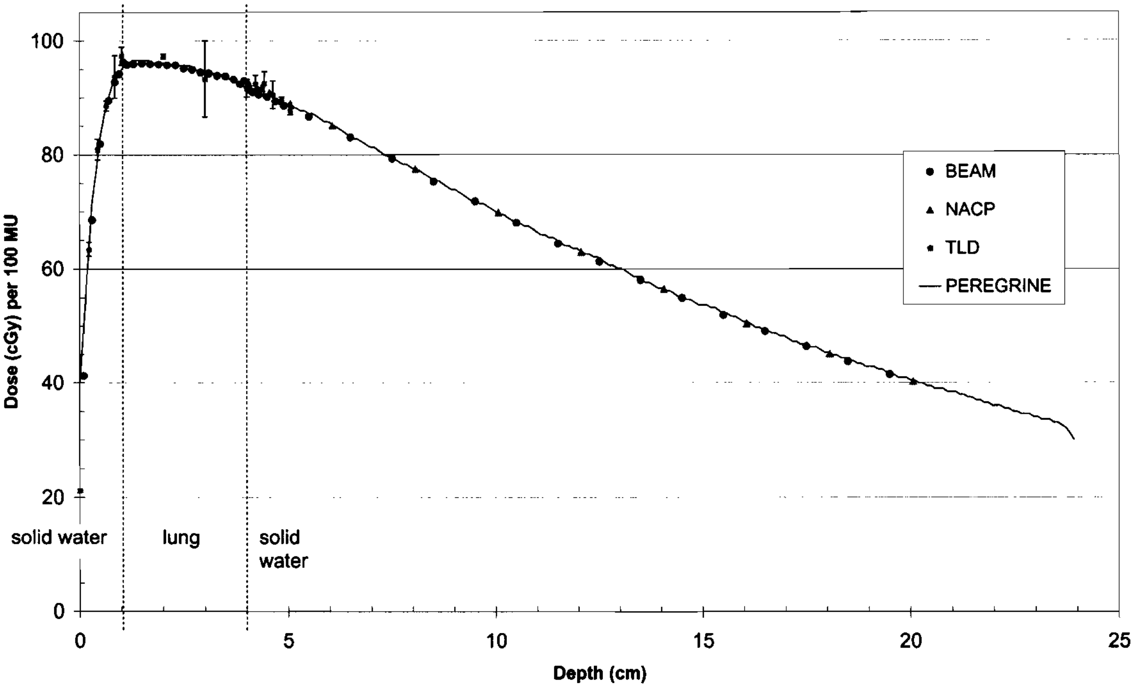

Figure 6-8: Comparison of 6 MV 10x10 cm² depth dose profiles in a solid water phantom containing a 3 cm slab of lung equivalent plastic. The solid line indicates PEREGRINE simulations, circles indicate BEAMnrc/DOSXYZnrc simulations, triangles indicated measurements with the NACP chamber and the squares indicate measurements with TLD-700 chips. Each TLD measurement point represents the average of 4 readings.

Due to the very small dimensions of the TLD, the uncertainty on the BEAMnrc/DOSXYZnrc simulations of the TLD measurements is very large. Considering the relative uncertainty on the calculations, with the exception of the 5 cm lung phantom, the correction factors at most points within the phantoms do not appear to be significant, however more simulation histories are required make any conclusions about these corrections. The 1-2 % fluence correction is attributed to the difference of the atomic number and density of lithium fluoride compared to the phantom materials which leads to a change in the electron fluence inside the TLD compared to the surrounding medium. Another possible explanation for this fluence perturbation is the contribution of photon interactions occurring inside the TLD. Mobit et al determined from simulations using EGS4 that the dose contributions from photon interactions inside a 1 mm thick LiF chip was 34 % of the total dose[8,9]. In this case it is more appropriate to apply the Burlin cavity theory to account for the

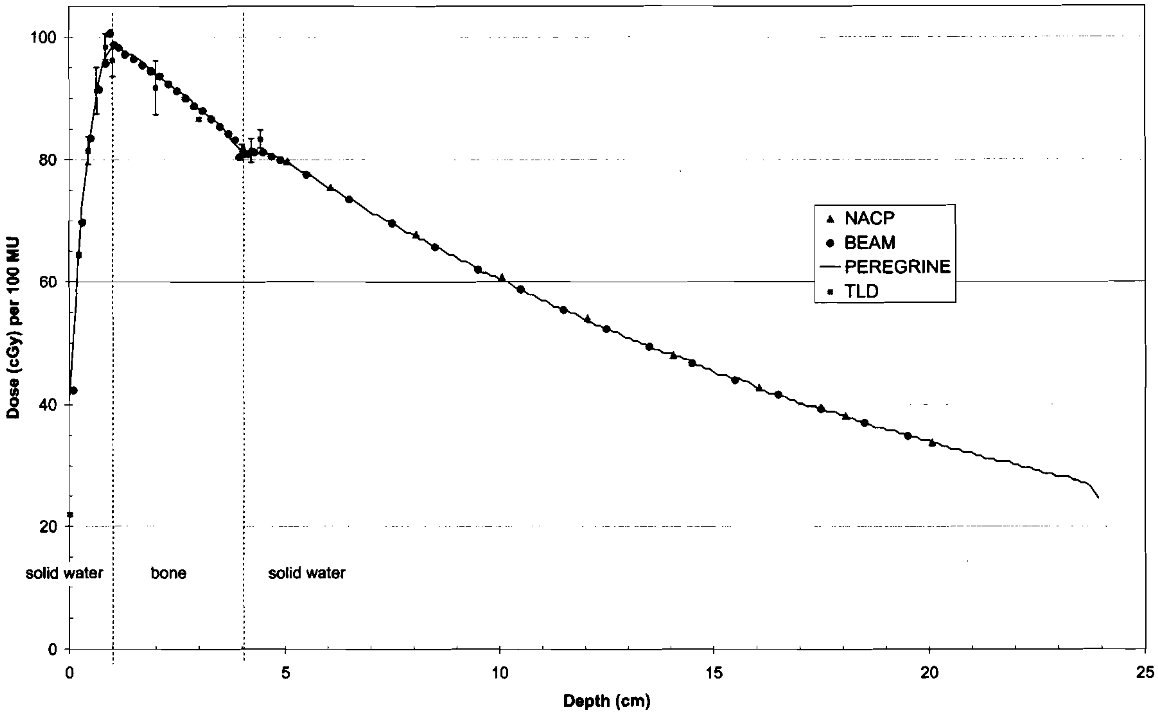

Figure 6-9: Comparison of 6 MV 10x10 cm^2 depth dose profiles in a solid water phantom containing a 3 cm slab of bone equivalent plastic. The solid line indicates PEREGRINE simulations, circles indicate BEAMnrc/DOSXYZnrc simulations, triangles indicated measurements with the NACP chamber and squares indicate measurements with TLD-700 chips. Each TLD measurement point represents the average of 4 readings.

contributions from these photon interactions. However, due the small thickness of the TLDs used in these measurements, it is expected that the number of photon interactions would be far less significant and the Spencer-Attix cavity theory can be applied. Application of the fluence correction factors improves the agreement between measurements and BEAMnrc/DOSXYZnrc for some points within the lung and bone phantoms but a more significant improvement could be realized by further repetition of the TLD measurements to account for the measurement uncertainties mentioned above.

Agreement between BEAMnrc/DOSXYZnrc and PEREGRINE is within 1% for all phantoms. The statistical uncertainty on each point of the DOSXYZnrc simulations is on average 0.5%. The most significant discrepancies occur at the interfaces where PEREGRINE fails to predict the perturbation at the interface due to averaging over the relatively larger dimensions of the scoring dosel compared to the 1 mm depth resolution used in the DOSXYZnrc simulations.

6.4 Comparison of PEREGRINE and CORVUS in heterogeneous phantoms

A comparison of 10x10 cm^2 depth dose profiles calculated by CORVUS, using the equivalent pathlength inhomogeneity correction, and PEREGRINE in the heterogeneous phantoms is shown in Figure 6-10 through 6-12. For these calculations the field size was defined by the MLC openings and the collimator jaw openings were set to back up the MLC leaves by 8 mm and 2 mm in the direction of leaf motion and across the leaf bank, respectively. A statistical quality factor of 0.1% was specified for the PEREGRINE simulations. The depth dose profiles in the heterogeneous phantoms were normalized to the dose at d_{max} for a 10x10 cm^2 MLC defined field in a homogeneous water phantom. Depth dose profiles calculated by CORVUS with no inhomogeneity correction are also shown for comparison.

The equivalent pathlength correction employed in the CORVUS dose calculation algorithm appears to overestimate the dose by approximately 5% inside the lung and bone layers. Beyond the heterogeneous layer the agreement is within 2%. This discrepancy is due, in part, to the fact that the dose calculated by CORVUS is based on dose deposition kernels which are calculated in water and then scaled by the relative electron density obtained from CT data. Therefore, CORVUS effectively calculates dose to water with a modified electron density unlike the PEREGRINE code which calculates dose to tissue. In terms of treatment plan evaluation, it is preferable to calculate dose to tissue as this is likely to yield better correlations with biological outcomes. The discrepancies between the PEREGRINE and CORVUS dose calculations in the vicinity of the lung and bone materials are also attributed to the inability of the CORVUS algorithm to account for electron transport in these materials.

In the 3 cm lung phantom, the PEREGRINE calculation predicts a reduced dose at the solid water/lung interface due to a decrease in backscatter from the lower density lung material downstream. Likewise, at the distal lung/solid water interface there is an increase in dose to the lung layer, from the increase in backscatter from the higher density solid water layer. The loss of electronic equilibrium at the interface is followed by a rebuildup in the

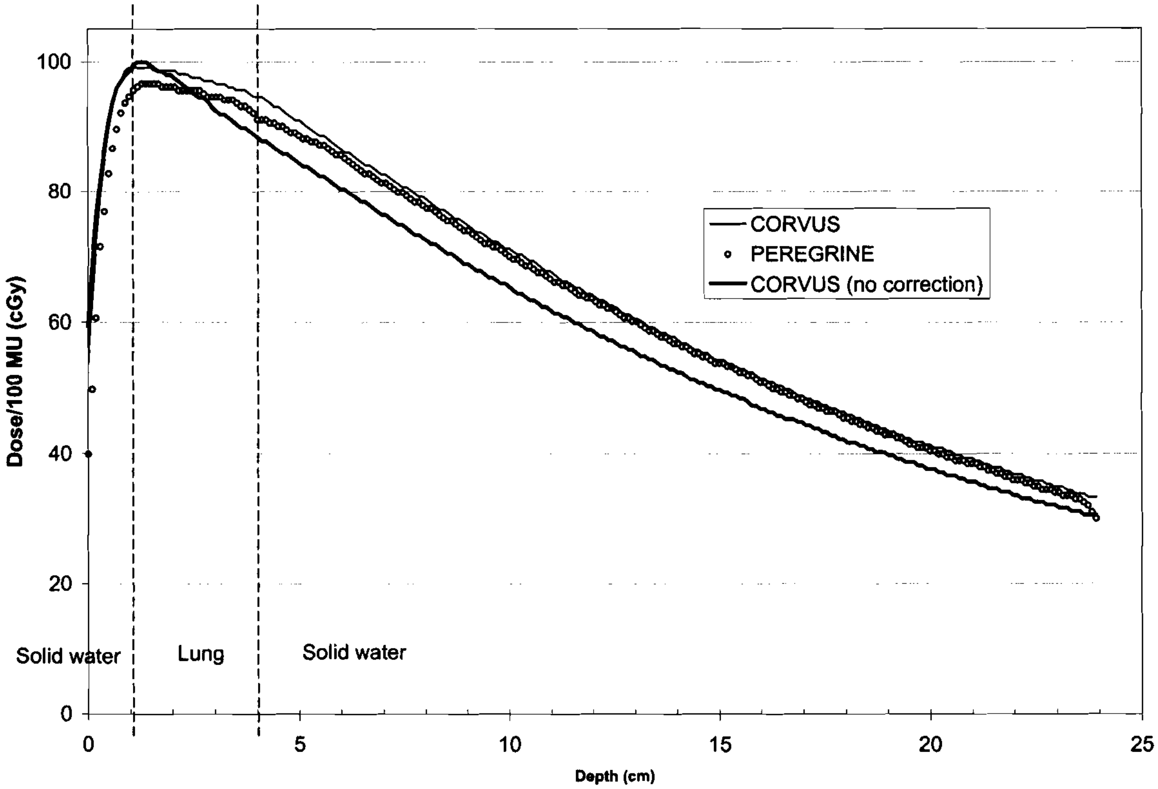

Figure 6-10: Comparison of 6 MV 10x10 cm^2 depth dose profiles in a solid water phantom containing a 3 cm slab of lung equivalent plastic. The field size is defined by the MLC with the jaws backing up the MLC leaves by 8 mm and 2 mm in the direction of leaf motion and across the leaf bank, respectively. The solid line indicates CORVUS calculation using no heterogeneity correction, the thin solid line indicates CORVUS calculation with heterogeneity correction and the open circles indicate PEREGRINE simulations.

solid water layer. These perturbations are not predicted by the CORVUS dose calculation algorithm which does not account for electron transport at these interfaces.

Inside the lung material the dose is influenced by the competing effects of reduced primary photon attenuation and an increase in lateral scattering of electrons which reduces the dose deposited along the central axis. This second effect, which is not modeled by CORVUS leads, in part, to an overestimation of the dose inside the lung layer[10,11]. These discrepancies are larger in the 5 cm lung phantom where, due to the increased thickness of the lung layer, the effects of lateral scattering of electrons are more significant.

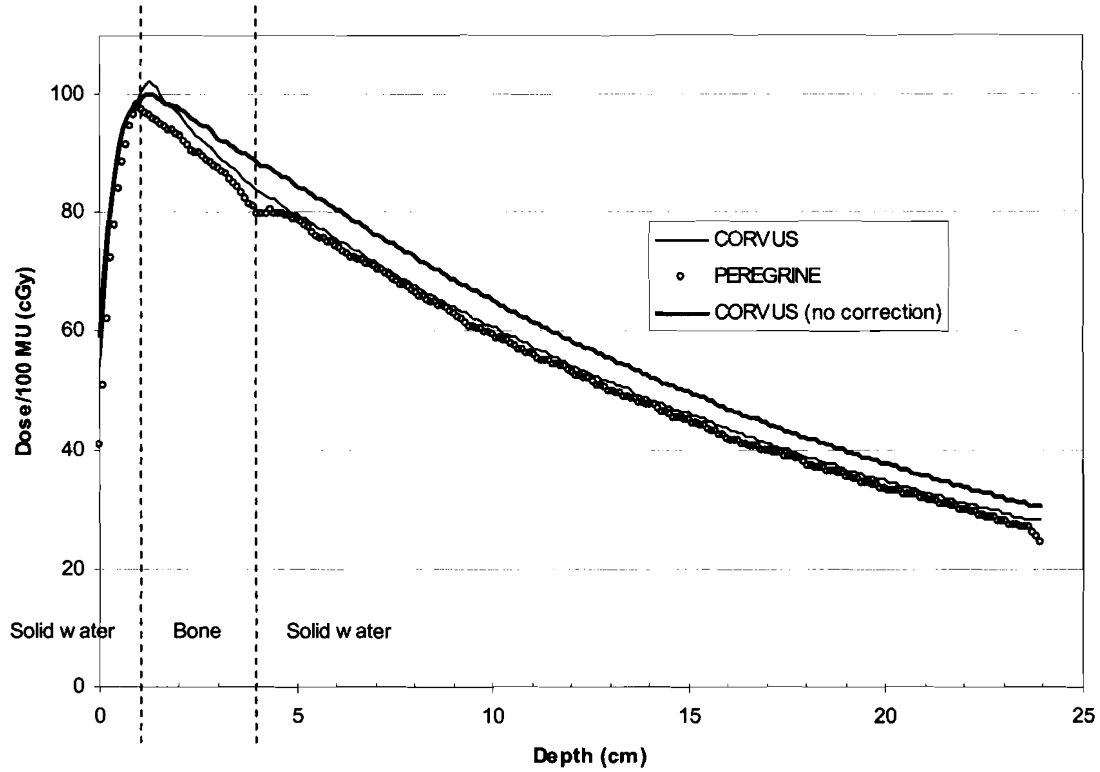

Figure 6-11: Comparison of 6 MV 10x10 cm^2 depth dose profiles in a solid water phantom containing a 3 cm slab of bone equivalent plastic. The field size is defined by the MLC with the jaws backing up the MLC leaves by 8 mm and 2 mm in the direction of leaf motion and across the leaf bank, respectively. The solid line indicates CORVUS calculation using no heterogeneity correction, the thin solid line indicates CORVUS calculation with heterogeneity correction and the open circles indicate PEREGRINE simulations.

Beyond the lung layer, the effects of decreased primary photon attenuation in the lung are dominant, leading to an increase in dose compared to a homogeneous water phantom. For a 6 MV photon beam the dominant mode of interaction is Compton scattering where the cross-sections are primarily dependent on the electron density of the medium. The equivalent pathlength correction, which scales the dose deposition kernels by the relative electron densities of the medium, therefore predicts the perturbation of the dose beyond the lung layer with a reasonably good accuracy for both phantoms. The 2% discrepancy in this region is attributed to the difference in stopping powers and photon attenuation coefficients between the Solid Water used in PEREGRINE calculations and the density modified water used in the

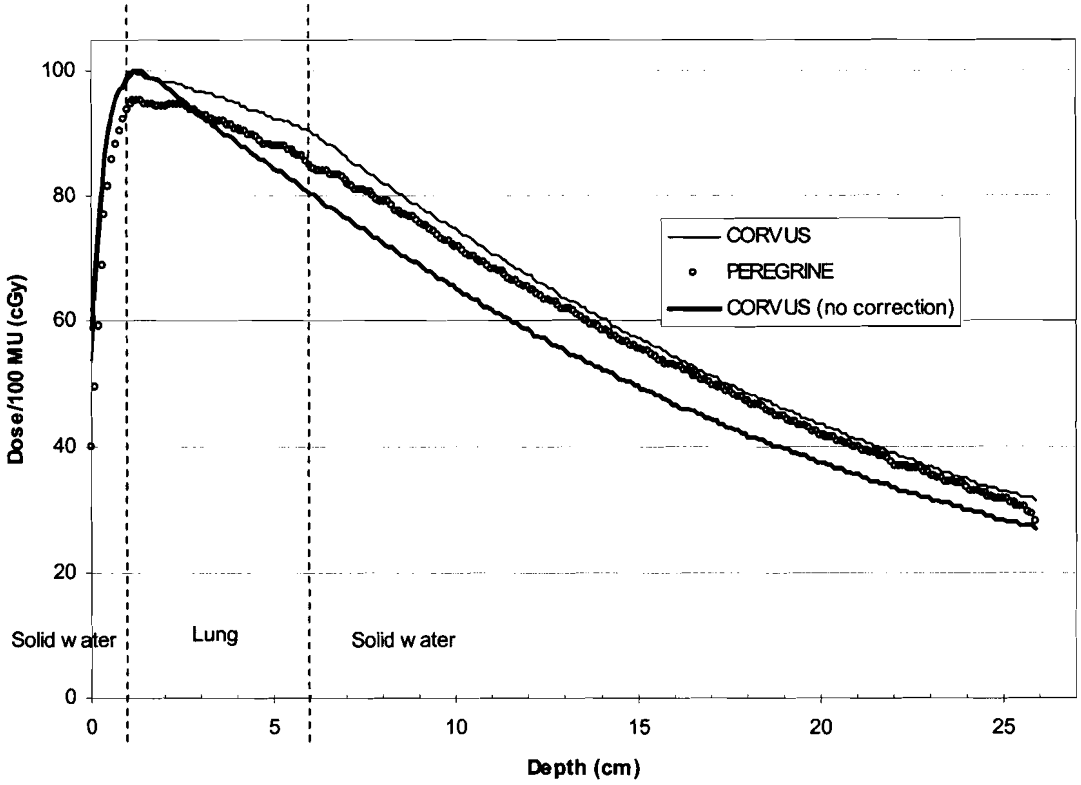

Figure 6-12: Comparison of 6 MV 10x10 cm^2 depth dose profiles in a solid water phantom containing a 5 cm slab of lung equivalent plastic. The field size is defined by the MLC with the jaws backing up the MLC leaves by 8 mm and 2 mm in the direction of leaf motion and across the leaf bank, respectively. The solid line indicates CORVUS calculation using no heterogeneity correction, the thin solid line indicates CORVUS calculation with heterogeneity correction and the open circles indicate PEREGRINE simulations.

CORVUS calculation.

In the bone phantom, the PEREGRINE calculation predicts an increase in the dose before the solid water/bone interface which is caused by backscatter from the higher density bone layer. At the distal bone/solid water interface there is a reduction in dose in the bone medium due to the decreased backscatter from the lower density solid water layer, followed by a re-buildup in the solid water. The dose profile calculated by CORVUS does not predict these perturbations.

Inside the bone layer the overestimation of the dose by CORVUS is partly due to the difference in interaction properties between the lung equivalent plastic and density modified water used in the CORVUS calculation. Furthermore, inside the higher density bone material the dose is affected by the increased attenuation of primary photons, which reduces the dose in the bone, and the reduced lateral scattering of electrons, compared to water, which increases the dose along the central axis. As in the case of the lung phantom, the discrepancy inside the bone layer is attributed in part to the inability of the CORVUS dose calculation algorithm to account for the reduced lateral scattering of electrons in the bone.

Beyond the bone layer the CORVUS algorithm predicts the reduced dose, due to increased primary photon attenuation, with reasonable accuracy, if the discrepancy due to the difference between Solid Water and density modified water is considered.

The differences between the dose calculated by CORVUS and PEREGRINE are expected to be larger for smaller field sizes for which the lateral disequilibrium inside lung and bone is more significant. A recent study using the EGSnrc Monte Carlo code has shown a 40% reduction in dose inside a 3 cm thick lung layer for a 0.5x0.5 cm^2 field compared to a 5x5 cm^2 field[12]. It was also noted that this perturbation increased with increasing thickness, decreasing beam energy and decreasing density of the heterogeneous layer. Similar trends for dose perturbations in the vicinity of an air cavity have also been observed in a study using the EGS4 Monte Carlo code[13].

6.5 Clinical IMRT case

To quantify the clinical impact of the differences observed between PEREGRINE and CORVUS calculations in the heterogeneous phantoms, a comparison of dose distributions calculated using the two codes was performed for a lung case subjected to IMRT. The treatment plan optimization was performed with no heterogeneity correction. After optimization, the final dose calculation was performed using either CORVUS with no heterogeneity correction, CORVUS with the equivalent pathlength correction and PEREGRINE. A statistical quality factor of 1% was specified for the PEREGRINE simulation. A comparison of the dose distributions obtained with these three methods is shown in Figure 6-13. The dose is normalized to the prescribed dose of 10 Gy, which occurs at 74% of the maximum dose. Cumulative dose volume histograms for the target, heart and tumour-bearing lung are shown in Figure 6-14.

The isodose lines in the PEREGRINE dose distributions are generally broader than those calculated by CORVUS, particularly in the low dose ranging up to 20% of the planned dose. The cumulative DVHs calculated by PEREGRINE are consistently shifted towards higher doses compared to those calculated by CORVUS. More detailed information regarding the dose coverage can be obtained by comparing differential DVHs, as shown in Figure 6-15, where the difference between the fractional volume receiving a given dose, calculated by PEREGRINE and CORVUS, is plotted as a function of the dose. In the target, CORVUS overestimates by approximately 2% the volume which receives between 90% and 110% and then underestimates the volume receiving greater than 110% by 2%. This discrepancy is due to dose perturbations occurring at the interface between the lung and tumour which are not modeled by CORVUS.

For the heart, CORVUS overestimates the volume receiving up to 20% of the planned target dose by as much as 13%. The volume of heart receiving more than 20% of the planned dose is then underestimated by up to 16%. Similar results were observed for the right lung which also lies in the low dose region.

For the tumour bearing lung, CORVUS overestimates the volume receiving less than 20% of the planned dose by up to 4% and then underestimates the volume of tissue receiving more than 20% of the planned dose by up to 2%. As observed in the differential DVH for the target, CORVUS overestimates the volume of tissue receiving between 100% and 120% of the planned dose.

The discrepancies in the low dose regions are attributed to lateral scattering of electrons in the lung, which causes the broadening of the 10% and 20% isodose volumes. Consequently, a larger volume of the lung and heart is covered by the 20% isodose volume and the average dose to the heart and lung is higher. The mean dose to the heart and left lung was calculated to be 46% and 7% higher, respectively, by PEREGRINE compared to CORVUS. It should be noted, however, that since PEREGRINE was observed to overestimate the dose in the buildup region after an air/water interface by 13% a similar overestimate of the dose in the vicinity of the low density lung can be expected.

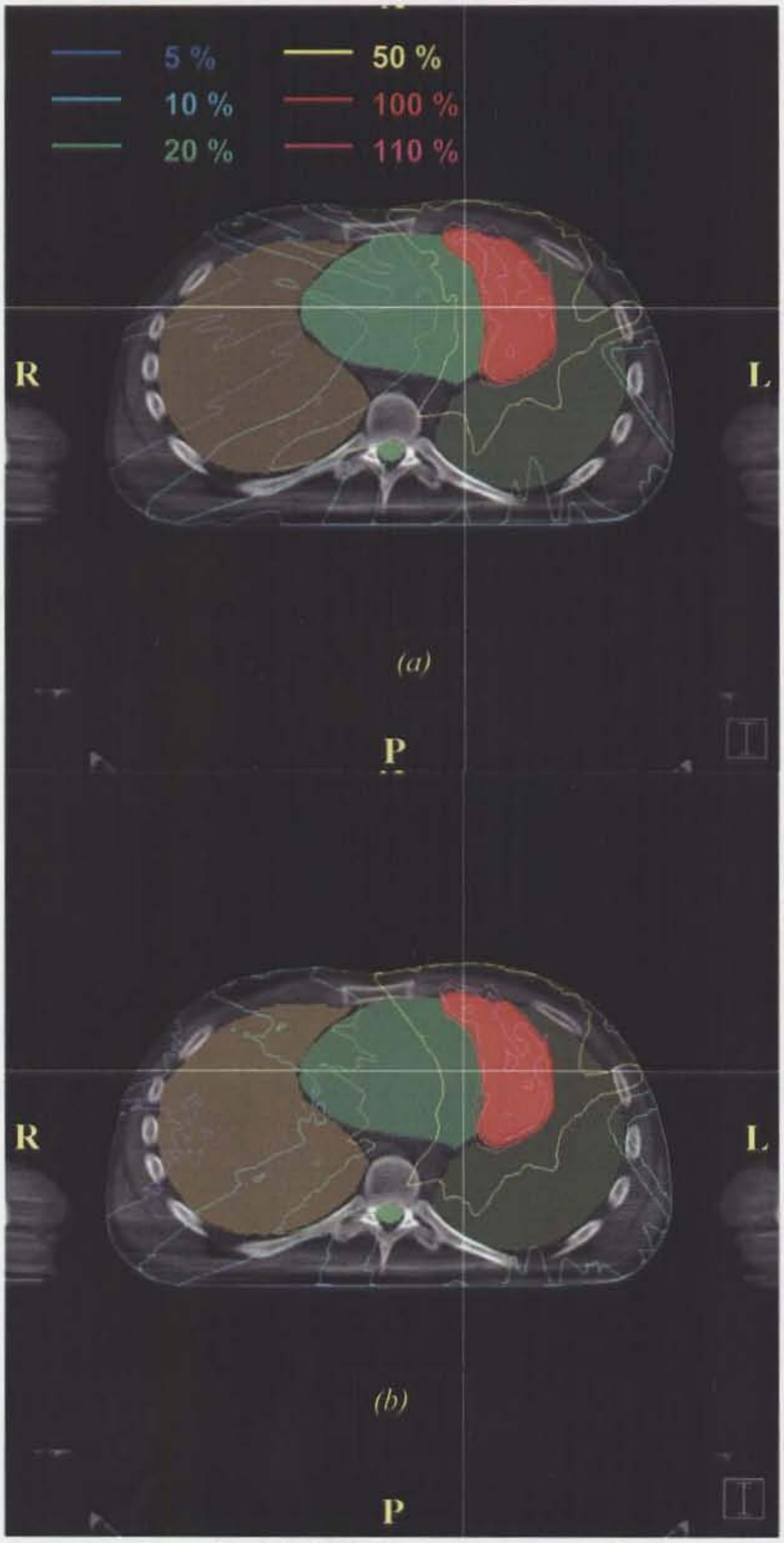

Figure 6-13: Comparison of axial IMRT dose distributions for treatment of a lung calculated by (a) CORVUS with equivalent pathlength inhomogeneity correction and (b) PEREGRINE. The dose distributions are normalized to the prescribed dose of 10 Gy.

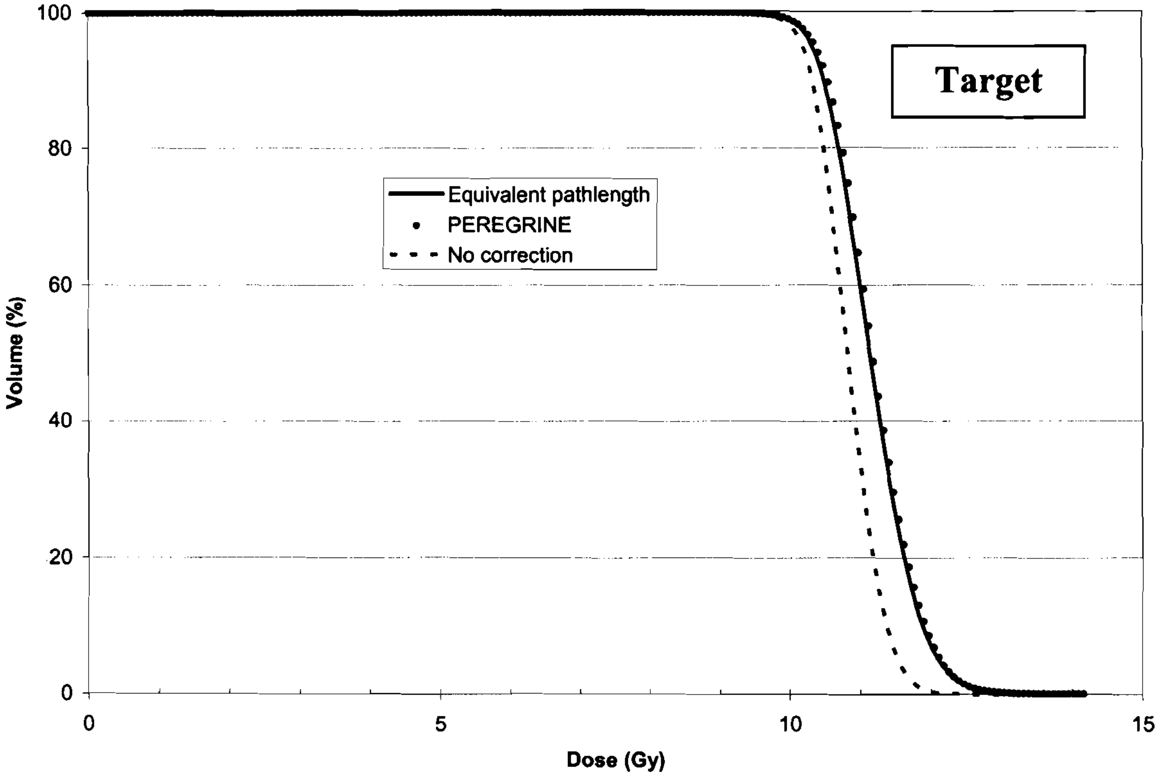
Target
Equivalent pathlength
PEREGRINE
No correction
Volume (%)
100
80
60
40
20
0
0
5
10
15
Dose (Gy)

(a)

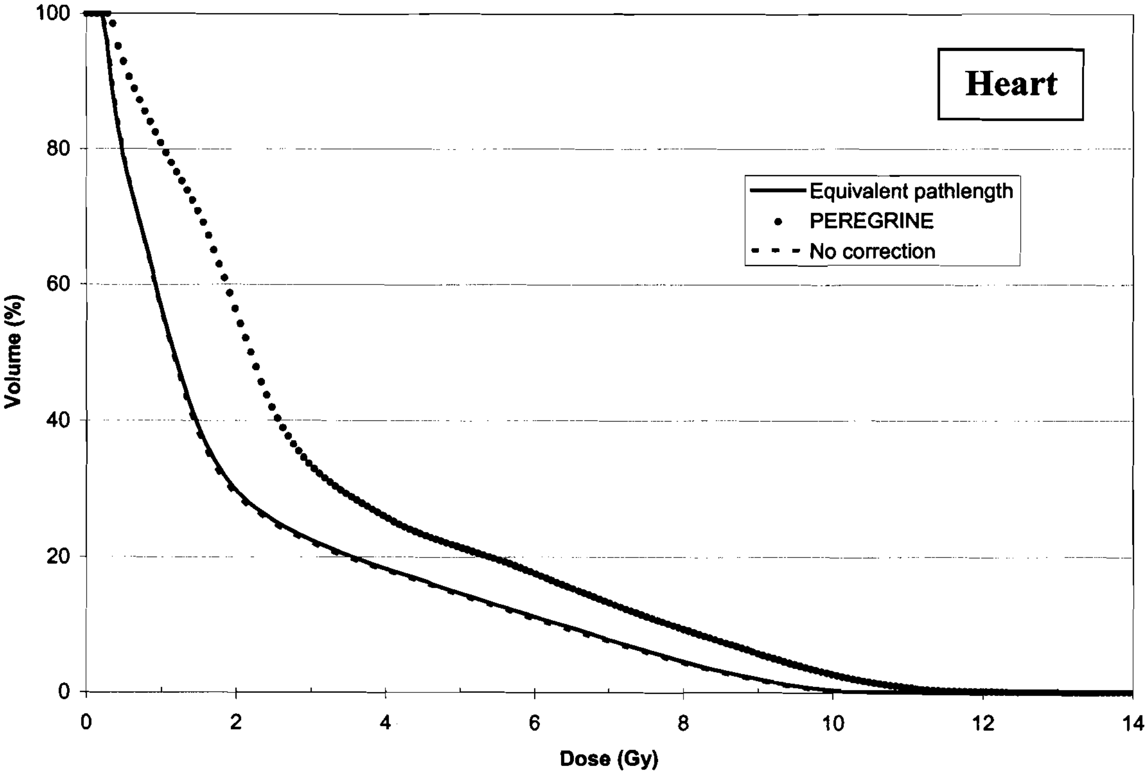
Heart
Equivalent pathlength
PEREGRINE
No correction
Volume (%)
100
80
60
40
20
0
0
2
4
6
8
10
12
14
Dose (Gy)

(b)

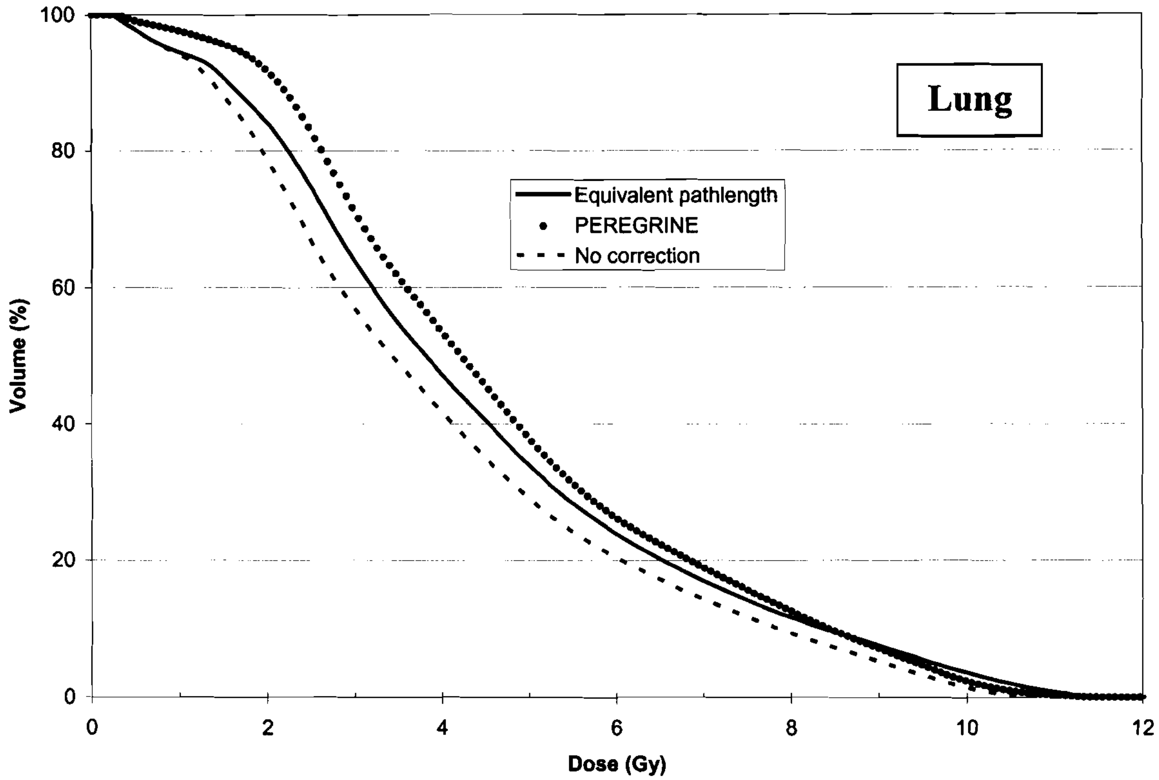

(c)

Figure 6-14: Cumulative dose volume histograms for (a) target, (b) heart and (c) tumour bearing lung. The solid line indicates CORVUS calculation with equivalent pathlength inhomogeneity correction, the dashed lines indicates CORVUS calculation with no inhomogeneity correction and the filled circles indicate PEREGRINE calculations.

The discrepancy is larger for the heart as a greater proportion of its volume is covered by the 10% and 20 % isodose lines and consequently the effects of the broadening of these isodoses is more significant than for the left lung.

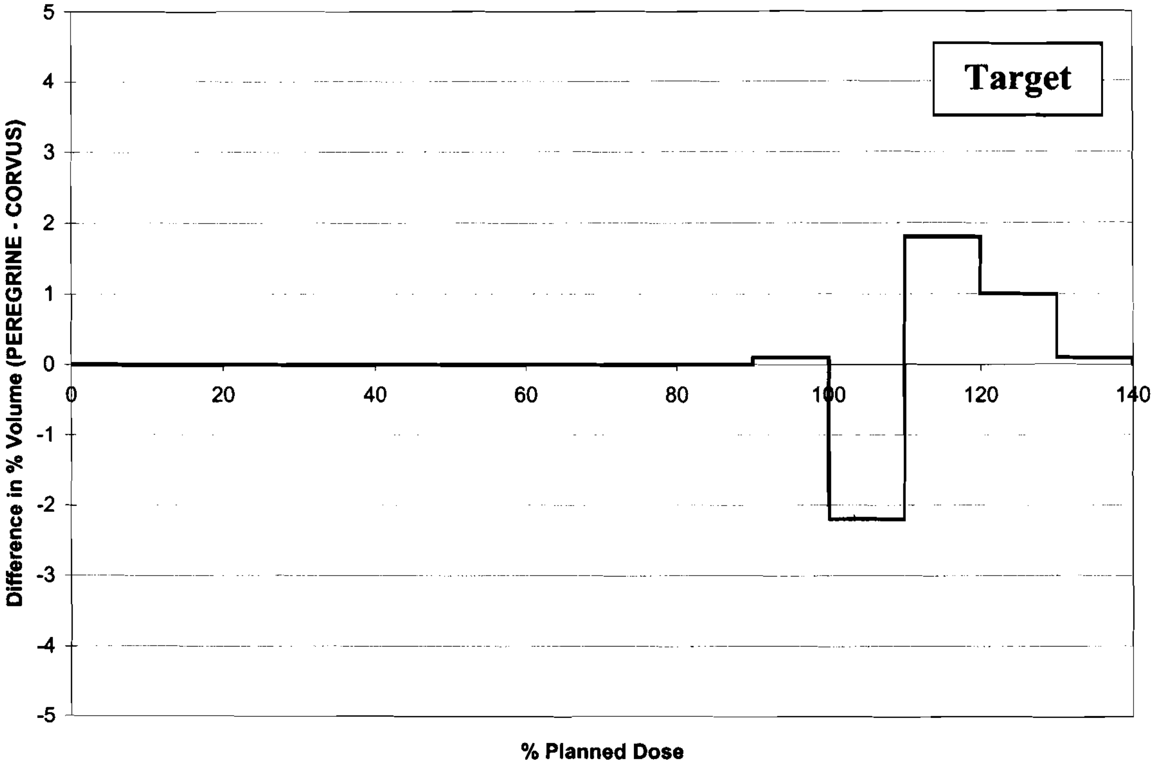
Target
Difference in % Volume (PEREGRINE - CORVUS)
5
4
3
2
1
0
-1
-2
-3
-4
-5
0
20
40
60
80
100
120
140
% Planned Dose

(a)

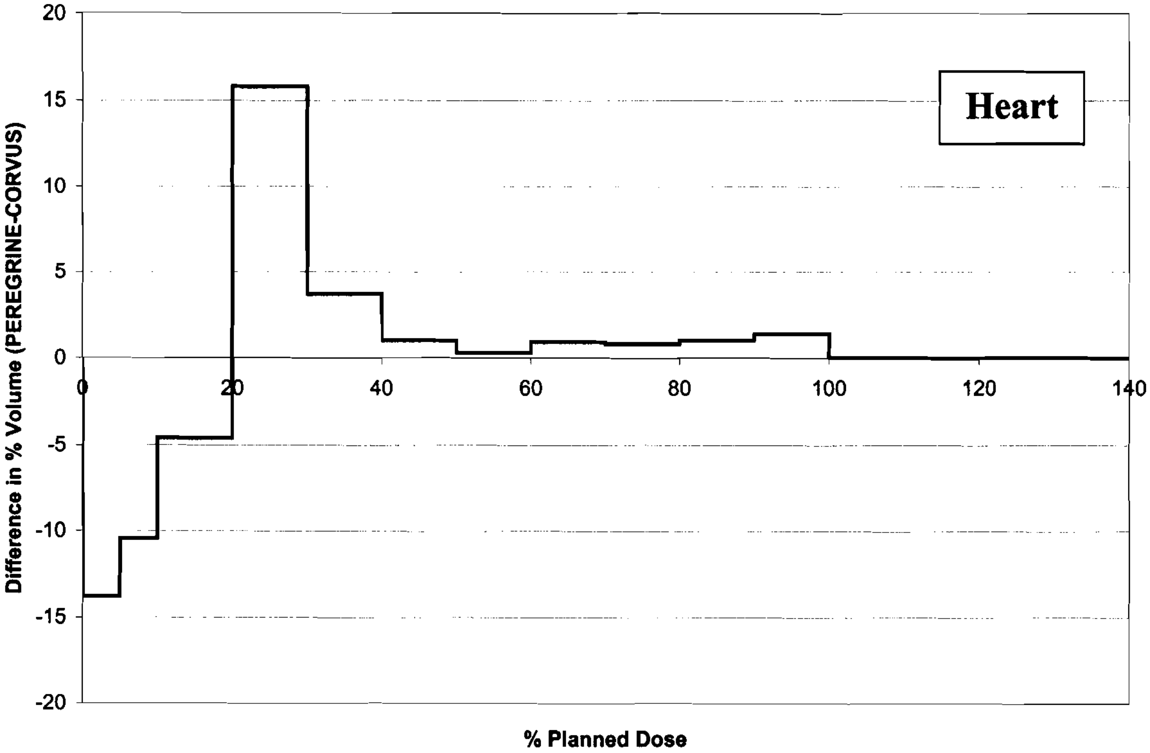
Heart
Difference in % Volume (PEREGRINE-CORVUS)
20
15
10
5
0
-5
-10
-15
-20
0
20
40
60
80
100
120
140
% Planned Dose

(b)

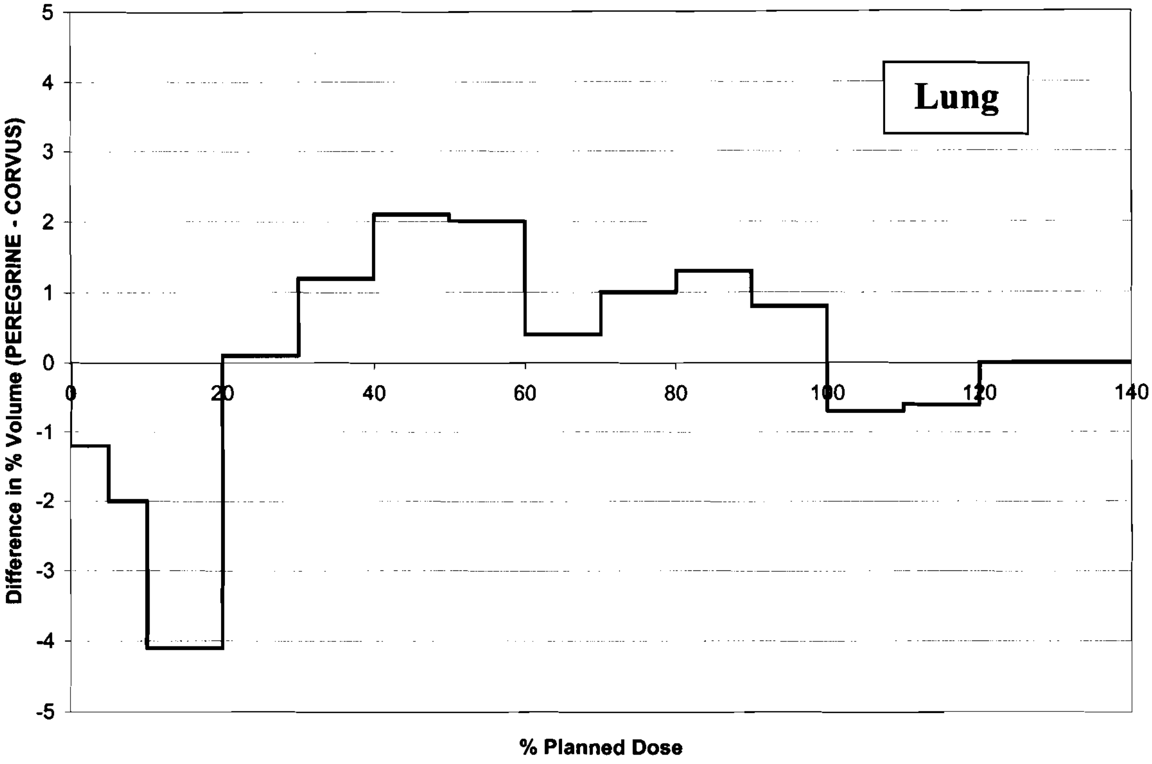

(c)

Figure 6-15: Histograms showing the difference between the percentage volume calculated by PEREGRINE and CORVUS with equivalent pathlength inhomegeneity correction for a given fraction of the planned dose. Histograms are shown for (a) target, (b) heart and (c) tumour bearing lung.

The higher dose calculated by PEREGRINE in the heart and lung may also be due to an underestimation of the MLC leakage contribution in the CORVUS algorithm. These sensitive structures may be shielded by the MLC leaves for a large portion of the treatment and therefore the MLC leakage dose represents a significant contribution in relation to the total dose received by the organ.

The trends noted in this comparison are consistent with a previous study which compared dose calculations using CADplan (Varian Oncology Systems, Palo Alto, CA), which also uses a density scaling inhomogeneity correction, and BEAMnrc/XVMC for 18 MV lung treatments employing parallel opposed beams[14].

To summarize, although no significant differences in terms of tumour coverage were noted between PEREGRINE and CORVUS, the heterogeneity correction employed in CORVUS may underestimate the mean delivered dose to sensitive structures in the vicinity of low density tissue by as much as 46%. The discrepancy is most significant for tissues receiving a low dose in the range of 10% to 30% of the planned dose.

There are two clinical implications related to the differences seen between the dose calculated by PEREGRINE and CORVUS. Firstly, the increased dose to the sensitive structures calculated by PEREGRINE may prompt a modification to the treatment plan, especially in cases where tight tolerance doses are imposed due to sensitization by a previous treatment regime. Secondly, an improved calculation of the dose distribution in the patient may lead to an improved correlation of treatment outcomes, such as normal tissue complications, with the dose delivered to the particular organ. This data could then be applied to re-evaluate the tolerance doses which are currently used in treatment planning[15].

6.6 References

[1] B. Nilsson and A. Montelius, "Fluence perturbation in photon beams under nonequilibrium conditions," Med. Phys. **13**, 191-195 (1986).

[2] B. Nilsson, A. Montelius and P. Andreo, "Wall effects in plane-parallel ionization chambers," Phys. Med. Biol. **41**, 609-623 (1996).

[3] C.L. Hartmann Siantar, R.S. Walling, T.P. Daly, B. Faddegon, N. Albright, P. Bergstrom, A.F. Bielajew, C. Chuang, D. Garrett, R.K. House, D. Knapp, D.J. Wiczorek and L.J. Verhey, "Description and dosimetric verification of the PEREGRINE Monte Carlo dose calculation system for photon beams incident on a water phantom," Med. Phys. **28**, 1322-1337 (2001).

[4] Task Group 21, "A protocol for the determination of absorbed dose form high-energy photon and electron beams," Med. Phys. **10**, 741-759 (1983).

[5] G.X. Ding, "Energy spectra, angular spread, fluence profiles and dose distributions of 6 and 18 MV photon beams: results of Monte Carlo simulations for a Varian 2100EX accelerator," Phys. Med. Biol. **47**, 1025-1046 (2002).

[6] G.X. Ding, C. Duzenli and N.I. Kalach, "Are neutrons responsible for the dose discrepancies between Monte Carlo calculations and measurements in the build-up region for a high-energy photon beam?," Phys. Med. Biol. **47**, 3251-3261 (2002).

[7] G.X. Ding, "Dose discrepancies between Monte Carlo calculations and measurements in the buildup region for a high-energy photon beam," Med. Phys. **29**, 2459-2463 (2002).

[8] P.N. Mobit, A.E. Nahum and P. Mayles, "An EGS4 Monte Carlo examination of general cavity theory," Phys. Med. Biol. **42**, 1319-1334 (1997).

[9] P.N. Mobit, "The use of Monte Carlo simulations for characterizing the energy response of thermoluminescent dosimeters in radiation therapy beams," International Workshop on Recent Development in Accurate Radiation Dosimetry, American Association of Physicists in Medicine Symposium Proceedings 13, 6-17 (2002).

[10] P.J. Keall and P.W. Hoban, "Superposition dose calculation incorporating Monte Carlo generated electron track kernels," Med. Phys. **23**, 479-485 (1996).

[11] M.K. Woo and J.R. Cunningham, "The validity of the density scaling method in primary electron transport for photon and electron beams," Med. Phys **17**, 187-194 (1990).

[12] A.O. Jones, I.J. Das and F.L. Jones, "A Monte Carlo study of IMRT beamlets in inhomegeneous media," Med. Phys. **30**, 296-300 (2003).

[13] X.A. Li, C. Yu and T. Holmes, "A systematic evaluation of air cavity dose perturbation in megavoltage x-ray beams," Med. Phys. **27**, 1011-1017 (2000).

[14] K.S. Al-Yahya, "Implementation of Monte Carlo treatment planning for lung cancer patients," M.Sc. Thesis, McGill University, 2002.

[15] B. Emami, J. Lyman, A. Brown, L. Coia, M. Goitein, J.E. Munzenrider, B. Shank, L.J. Solin and M. Wesson, "Tolerance of normal tissue to therapeutic radiation," Int. J. Radiation Oncology Biol. Phys. **21**, 109-122 (1991).

Chapter 7:

Conclusions and Future Work

7.1 Summary and conclusions

The accuracy of patient dose calculations for external beam photon therapy can be improved by the use of a Monte Carlo dose calculation code, which explicitly models the transport of the incident radiation through the accelerator head and the patient. This is particularly of interest for intensity modulated radiation therapy (IMRT) where the accuracy of conventional dose calculation algorithms is compromised by the approximations used to model the effects of the MLC and the calculation of dose in regions of non-uniform density. The PEREGRINE Monte Carlo dose calculation code is the first commercially available Monte Carlo code for calculation of IMRT dose distributions. An evaluation of the dosimetric accuracy of PEREGRINE was performed for 6 MV photon beams by comparing calculated dose profiles with measurements and dose profiles calculated using the EGSnrc Monte Carlo code in homogeneous and heterogeneous phantoms.

A model of the Varian CL21EX linear accelerator was built using the BEAMnrc code. A new MLC component module, called DYNVMLC, was developed to fully model the Millenium 120 leaf collimator including the details of the inner and outer leaves. A leaf material density of 18.0 g/cm^3 and abutting leaf gap of 0.004 cm were chosen to match calculated interleaf and abutting leaf leakage profiles to film measurements at a depth of 5 cm in Solid Water.

Depth dose profiles, off-axis profiles and output factors measured in water for field sizes ranging from 2x2 cm^2 to 30x30 cm^2 using an Exradin A14P parallel plate chamber were compared to PEREGRINE calculations. Agreement between the measurements and PEREGRINE was within 1% along the central axis for all fields. The agreement between the measurements and PEREGRINE for the off-axis dose was within 1% with the exception of the penumbra region where the measurements yield systematically lower dose than the

PEREGRINE calculations by 3% of the central axis dose, which may be related to uncertainty in the measurements due to the significant polarity effect of the Exradin chamber, as well as deficiencies in the PEREGRINE beam model to predict the 30x30 cm^2 off-axis fluence accurately.

Measurements in the buildup region for a 10x10 cm^2 and 40x40 cm^2 field with an NACP parallel plate chamber were found to overestimate the dose by 13% compared to simulations using EGSnrc due to chamber overresponse near the water surface. Assuming an effective point of measurement on the inside surface of the front window the parallel plate chamber, a chamber perturbation correction of 1.28 ± 0.02 at the water surface was calculated for the 10x10 cm^2 field. In comparison to EGSnrc, PEREGRINE overestimates the dose near the surface by 13% due to the artificially increased weight of the electron subsource weight in the 6 MV beam model in order to match PEREGRINE simulations to measurements with an IC10 chamber in the buildup region.

Central axis depth dose profiles were measured in heterogeneous phantoms consisting of water, bone and lung equivalent plastics with TLD-700 dosimeters and the NACP chamber. The agreement between measurements and profiles calculated using EGSnrc was within 1% for the NACP chamber and within 3% for TLDs. Fluence perturbation corrections for the TLD measurements were determined to be on the order of 1% to 2%. Agreement between PEREGRINE and EGSnrc was within 1% for all phantoms.

A comparison of dose profiles calculated by PEREGRINE and the CORVUS dose calculation algorithm was performed in the heterogeneous phantoms. In comparison to PEREGRINE, CORVUS overestimates the dose inside the lung and bone equivalent plastics by 5% due to the inability of the equivalent pathlength inhomogeneity correction to model the effects of electron transport in these regions. The accuracy of the CORVUS algorithm is also compromised by the fact that in principle it calculates dose to water instead of dose to tissue. Dose distributions calculated by CORVUS and PEREGRINE were compared for a lung case treated with dynamic IMRT. The treatment plan was optimized in CORVUS without heterogeneity corrections and the final dose calculation was calculated using either CORVUS, with and without the heterogeneity correction, or PEREGRINE. The CORVUS dose calculation algorithm underestimates the dose to sensitive structures which lie in low dose regions receiving up to 20% of the prescribed dose. The mean dose in the critical structures was predicted to be up to 46% higher by PEREGRINE although the accuracy of these calculations will be affected by the fact that it has been shown that PEREGRINE overestimates the dose in the buildup region.

Overall the agreement between PEREGRINE, EGSnrc and measurements for simple uniform fields is excellent in both homogeneous and heterogeneous phantoms, with the exception of the buildup region and for 30x30 cm^2 fields where limitations in the PEREGRINE beam model affect the accuracy. A clinical comparison of IMRT dose distributions indicates that the accuracy of dose calculations to sensitive structures in the vicinity of low-density tissues is significantly improved using PEREGRINE compared to the inhomogeneity correction implemented in the CORVUS dose calculation algorithm.

7.2 Future work

Further investigation of the dosimetric accuracy of the PEREGRINE dose calculation code should include an evaluation of the MLC model implemented in PEREGRINE. As PEREGRINE is intended for calculation of IMRT dose distributions, where the fields are defined by the MLC openings, the accuracy of this model may significantly affect the dose calculation, especially in the low dose areas. A comparison of dose profiles calculated by PEREGRINE and BEAMnrc, using the new MLC component module, is planned for open and blocked MLC defined fields.

Further evaluation of the accuracy of PEREGRINE dose calculations in heterogeneous phantoms is planned for smaller field sizes where the perturbations are expected to be more significant. These smaller fields would also be more comparable to the small subfields used in IMRT. A comparison of dose calculations in an air cavity phantom is also planned.

Modifications to the DYNVMLC component module are also planned to permit sampling of the leaf openings from leaf sequence files for dynamic and step and shoot IMRT treatments. This will be followed by a comparison of IMRT dose distributions calculated using BEAMnrc/XVMC and PEREGRINE to evaluate the clinical significance of the discrepancies in the buildup region, as well as any limitations of the MLC model used in PEREGRINE.

Finally, although 18 MV photons are not currently used for IMRT treatments at our institution, the comparison process outlined in this work can be applied to evaluate the accuracy of PEREGRINE at this energy. Of particular interest is the accuracy of the dose calculations in the buildup region where significant discrepancies have been reported and have yet to be resolved.

Bibliography

AAPM Task Group 21, "A protocol for the determination of absorbed dose form high-energy photon and electron beams," Med. Phys. **10**, 741-759 (1983).[89]

AAPM Task Group No. 50, "Basic applications of multileaf collimators," AAPM Report No. 72, American Association of Physicists in Medicine (2001).[51]

AAPM Task Group 55, "Radiochromic film dosimetry: Recommendations of AAPM Radiation Therapy Task Group 55," Med. Phys. **25**, 2093-2115 (1998).[25]

P.R. Almond, P.J. Briggs, B.M. Coursey, W.F. Hanson, M.S. Huq, R. Nath and D.W.O. Rogers, "AAPM's TG-51 protocol for clinical reference dosimetry of high-energy photon and electron beams," Med. Phys. **26**, 1847-1870 (1999).[69,71,77]

K.S. Al-Yahya, "Implementation of Monte Carlo treatment planning for lung cancer patients," M.Sc. Thesis, McGill University, 2002.[105]

M.R. Arnfield, C. Hartmann-Siantar, L. Cox and R. Mohan, "The impact of electron transport on the accuracy of computed dose," Med. Phys. 27, 1266-1274 (2000).[9].

F.H. Attix, *Introduction to Radiological Physics and Radiation Dosimetry*, (John Wiley & Sons, New York, 1986).[12]

M.J. Berger, "Monte Carlo Calculation of the Penetration and Diffusion of Fast Charged Particles," *Methods in Computational Physics Volume 1: Statistical Physics* (Academic Press, New York, 1963).[37]

M.J. Berger and S.M. Seltzer, "Tables of Energy Losses and Ranges of Electrons and Positrons," NASA Report SP-3012, NASA Washington (1964).[41]

M.J. Berger and S.M. Seltzer, "ETRAN, Monte Carlo code system for electron and photon transport through extended media," *Documentation for RSIC Computer Code Package CCC-107* (Oak Ridge Natl. Lab., Oak Ridge, Tennessee, 1973).[40]

P.R. Bevington and D.K. Robinson, *Data Reduction and Error Analysis for the Physical Sciences*, (McGraw-Hill, New York, 1992).[39]

A.F. Bielajew, "HOWFAR and HOWNEAR: Geometry Modeling for Monte Carlo Particle Transport," NRCC Reports PIRS-0341 (1995).[43]

A.F. Bielajew and D.W.O Rogers, "PRESTA – The "Parameter Reduced Electron-Step Transport Algorithm" for electron Monte Carlo transport," NRCC Report PIRS-0042, NRCC Canada (1987).[40,41]

A.F. Bielajew, H. Hirayama, W.R. Nelson and D.W.O. Rogers "History, overview and recent improvements of EGS4," NRCC Report PIRS-0436, NRCC Canada (1994).[41]

T.R. Bortfeld, D.L. Kahler, T.W. Waldron and A.L. Boyer, "X-ray field compensation with multileaf collimators," Int. J. Radiation Oncology Biol. Phys. **28**, 723-730 (1994).[7]

J.D. Bourland and E.L. Chaney, "A finite-size pencil beam model of photon dose calculations in three dimensions," Med. Phys. **19**, 1401-1411 (1992).[29]

A.L. Boyer and S. Liu, "Geometric analysis of light-field position of a multileaf collimator with curved ends," Med. Phys. **24**, 757-762 (1997).[51]

W.H. Bragg, *Studies in radioactivity*, (MacMillan and Co., London, 1912).[19]

T.E. Burlin, "A general cavity theory of ionization," Br. J. Radiology **39**, 727-734 (1966). [21]

R. Cameron, N. Suntharalingam and G.N. Kenney, *Thermoluminescent Dosimetry*, (University of Wisconsin Press, Madison, 1968).[27,72]

D.E. Cullen, M.H. Chen, J.H. Hubbell, S.T. Perkins, E.F.Plechaty, J.A. Rathkopf and J.H Scofield, Lawrence Livermore National Laboratory Report UCRL-50400, Volume 6, LLNL, Livermore (1989).[48]

G.X. Ding, "Energy spectra, angular spread, fluence profiles and dose distributions of 6 and 18 MV photon beams: results of Monte Carlo simulations for a Varian 2100EX accelerator," Phys. Med. Biol. **47**, 1025-1046 (2002).[89]

G.X. Ding, "Dose discrepancies between Monte Carlo calculations and measurements in the buildup region for a high-energy photon beam," Med. Phys. **29**, 2459-2463 (2002).[89]

G.X. Ding, C. Duzenli and N.I. Kalach, "Are neutrons responsible for the dose discrepancies between Monte Carlo calculations and measurements in the build-up region for a high-energy photon beam?," Phys. Med. Biol. **47**, 3251-3261 (2002).[89]

C. Duzenli, B. McClean and C. Field, " Backscatter into the beam monitor chamber: Implications for dosimetry of asymmetric collimators," Med. Phys. **20**, 363-367 (1993).[45]

B. Emami, J. Lyman, A. Brown, L. Coia, M. Goitein, J.E. Munzenrider, B. Shank, L.J. Solin and M. Wesson, "Tolerance of normal tissue to therapeutic radiation," Int. J. Radiation Oncology Biol. Phys. **21**, 109-122 (1991).[106]

P. Francescon, S. Cora, C. Cavedon, P. Schalchi, S. Reccanello and F. Colombo, "Use of a new type of radiochromic film, a new parallel-plate micro-chamber, MOSFETs, and TLD 800 microcubes in the dosimetry of small beams," Med. Phys. **25**, 503-511 (1998).[69]

S. Goudsmit and J.L. Saunderson, “Multiple Scattering of Electrons,” Phys. Rev. **57**, 24 (1940).[37]

L.H. Gray, “The absorption of penetrating radiation,” Proc. Roy. Soc. **A122**, 647-668 (1929). [19]

L.H. Gray, “An ionization method for the absolute measurement of y-ray energy,” Proc. Roy. Soc. **A156**, 578-596 (1936).[19]

E. Hall, *Radiobiology for the Radiologist* (J.R. Lippincott Co., Philadelphia, 1994).[1]

C.L. Hartmann Siantar, R.S. Walling, T.P. Daly, B. Faddegon, N. Albright, P. Bergstrom, A.F. Bielajew, C. Chuang, D. Garrett, R.K. House, D. Knapp, D.J. Wieczorek and L.J. Verhey, “Description and dosimetric verification of the PEREGRINE Monte Carlo dose calculation system for photon beams incident on a water phantom,” Med. Phys. **28**, 1322-1337 (2001).[44,89]

M.S. Huq, I.J. Das, T. Steinberg and J.M. Galvin, “A dosimetric comparison of various multileaf collimators,” Phys. Med. Biol. **47**, 159-170 (2002).[53]

IAEA, “The use of plane parallel ionization chambers in high energy electron and photon beams: an international code of practice for dosimetry,” Technical Report series Vol. 381, International Atomic Energy Agency, Vienna (1997).[69]

ICRU, “Stopping Powers for Electrons and Positrons,” ICRU Report No. 37, International Commission on Radiation Units and Measurements, Bethesda (1984).[48]

ICRU, “Prescribing, Recording and Reporting Photon Beam Therapy,” ICRU Report No.50, International Commission on Radiation Units and Measurements, Bethesda (1993).[5]

IMRT Collaborative Working Group, “Intensity-Modulated Radiotherapy: Current Status and Issues of Interest,” Int. J. Radiation Oncology Biol. Phys. **51,** 880-914 (2001).[7]

D.A. Jaffray and J.J. Battista, “X-ray sources of medical linear accelerators: Focal and extra-focal radiation,” Med. Phys. **20**, 1417-1427 (1993).[29]

H.E. Johns and J.R. Cunningham, *The Physics of Radiology*, (Charles C. Thomas, Springfield, 1983).[20]

A.O. Jones, I.J. Das and F.L. Jones, “A Monte Carlo study of IMRT beamlets in inhomegeneous media,” Med. Phys. **30**, 296-300 (2003).[99]

A. Kapur, C.M. Ma and A.L. Boyer, “Monte Carlo simulations for multileaf collimator leaves: design and dosimetry,” *Proc. Chicago 2000 World Congress on Medical Physics and Biomedical Engineering* (2000).[54]

I. Kawrakow, “Accurate condensed history Monte Carlo simulation of electron transport. I EGSnrc, the new EGS4 version,” Med Phys **27**, 485 – 498 (2000).[41]

I. Kawrakow and D.W.O. Rogers, “The EGSnrc Code System: Monte Carlo Simulation of Electron and Photon Transport,” NRCC Reports PIRS-701, NRC Canada (2001).[42]

P.J. Keall and P.W. Hoban, “Superposition dose calculation incorporating Monte Carlo generated electron track kernels,” Med. Phys. **23**, 479-485 (1996).[96]

F.M. Khan and R.A. Potish, *Treatment Planning in Radiation Oncology* (William and Wilkins, Baltimore, 1998).[4]

H-R Lee, M. Pankuch, J.C. Chu and J. Spokas, “Evaluation and characterization of a parallel plate microchamber's functionalities in small beam dosimetry,” Med. Phys. **29**, 2489-2496 (2002).[70]

X.A. Li, C. Yu and T. Holmes, "A systematic evaluation of air cavity dose perturbation in megavoltage x-ray beams," Med. Phys. **27**, 1011-1017 (2000).[99]

I. Lux and L. Koblinger, *Monte Carlo Particle Transport Methods:Neutron and Photon Calculations*, (CRC Press, Boca Raton, 1991).[48]

T.R. Mackie and J.R. Palta, "Teletherapy: Present and Future," *Proceedings of the AAPM 1996 Summer School* (American Association of Physicists in Medicine, College Park, 1996).[29]

A.F. McKinlay, *Thermoluminescence Dosimetry*, (Medical Physics Handbooks, Adam Hilger Ltd. Bristol, 1981).[26,72]

P.N. Mobit, A.E. Nahum and P. Mayles, "An EGS4 Monte Carlo examination of general cavity theory," Phys. Med. Biol. **42**, 1319-1334 (1997).[93]

P.N. Mobit, "The use of Monte Carlo simulations for characterizing the energy response of thermoluminescent dosimeters in radiation therapy beams," International Workshop on Recent Development in Accurate Radiation Dosimetry, American Association of Physicists in Medicine Symposium Proceedings 13, 6-17 (2002).[93]

G. Moliere, "Theorie der Streuung schneller geladener Teilchen II:Mehrfach-und Vielfachstreuung," Z. Naturforsch. **3a**, 78 (1948).[37]

National Cancer Institute of Canada, "Canadian Cancer Statistics 2002," Toronto (2002).[1]

National Institute of Science and Technology, Gaithersburg, MD. [14,18].

Nordic Association of Clinical Physics, "Procedures in external radiation therapy dosimetry with electron and photon beams with maximum energies between 1 and 50 MeV," Acta Radiol. Oncol. **19**, 55-79 (1980).[70]

W.R. Nelson, J. Hirayama and D.W.O Rogers, "The EGS4 code system," Stanford Linear Accelerator Report SLAC-265 (1985).[41]

B. Nilsson and A. Montelius, "Fluence perturbation in photon beams under nonequilibrium conditions," Med. Phys. **13**, 191-195 (1986).[87]

B. Nilsson, A. Montelius and P. Andreo, "Wall effects in plane-parallel ionization chambers," Phys. Med. Biol. **41**, 609-623 (1996).[87]

P.S. Nizin and X.S. Chang, "Primary dose in photon beams with lateral electronic disequilibrium," Med. Phys. **18**, 744-748, (1991).[29]

NOMOS, "CORVUS Beam Utilities 4.1 User Manual," NOMOS Corporation, Cranberry Township, PA , 2002.[29]

J.E. O'Connor, "The variation of scattered x-rays with density in an irradiated body," Phys. Med. Biol. **1**, 352-369 (1957).[30]

J.R. Palta, D.K. Yeung and V. Frouhar, "Dosimetric considerations for a multileaf collimator system," Med. Phys **23**, 1219-1224 (1996).[51]

S.T. Perkins, D.E. Cullen and S.M. Seltzer, Lawrence Livermore National Laboratory Report No. UCRL-50400, Vol. 31, LLNL, Livermore (1991).[48]

Radiation Therapy Oncology Group, Philadelphia, PA.[73].

D.W.O. Rogers and A.F. Bielajew, "Monte Carlo Techniques of Electron and Photon Transport for Radiation Dosimetry," *The Dosimetry of Ionizing Radiation*, (Academic Press, New York, 1990).[35,38,39]

D.W.O. Rogers, B.A. Faddegon, G.X. Ding, C.M. Ma and J. We, "BEAM: A Monte Carlo code to simulate radiotherapy treatment units", Med Phys **22** 503– 524 (1995).[43,60]

D.W.O. Rogers, C.M. Ma, G.X. Ding and B. Walters, "BEAMnrc Users Manual," NRCC Report PIRS-0509(A), National Research Council of Canada, 1996.[55]

A.E. Schach von Wittenau, L.J. Cox, P.M. Bergstrom, Jr., W.P. Chandler and C.L. Hartmann Siantar, "Correlated histogram representation of Monte Carlo derived medical accelerator photon-output phase space", Med. Phys. **26**,1196-1211 (1999).[44]

D. Sheikh-Bagheri and D.W. Rogers, "Sensitivity of megavoltage photon beam Monte Carlo simulations to electron beam and other parameters," Med. Phys. **29**, 379-390 (2002).[61]

L.V. Spencer and F.H. Attix, "A theory of cavity ionization," Radiation Res. **3**, 239-254 (1955).[20]

E. Storm and H.I. Israel, "Photon cross-sections from 1 keV to 100 MeV for element Z=1 to Z=100," Atomic Data and Nuclear Data Tables **7**, 565-681 (1997).[41]

J. Van Dyk, *The Modern Technology of Radiation Oncology: A Compendium for Medical Physicists and Radiation Oncologists* (Medical Physics Publishing, Madison, Wisconsin, 1999).[3,4,9]

B.R.B. Walters, I. Kawrakow and D.W.O. Rogers "History by history statistical estimators in the BEAM code system," Med. Phys. **29**, 2745 – 2752 (2002).[39]

S. Webb, "Optimisation of conformal radiotherapy dose distributions by simulated annealing," Phys. Med. Biol. **34**, 1349-1370 (1989).[6]

A.B. Wolbarst, *Physics of Radiology*, (Medical Physics Publishing, Wisconsin, 1993). [23]

M.K. Woo and J.R. Cunningham, “The validity of the density scaling method in primary electron transport for photon and electron beams,” Med. Phys **17**, 187-194 (1990).[96]

X.R. Zhu, P.A. Jursinic, D.F. Grimm, F. Lopez, J.J. Rownd and M.T. Gillin, “Evaluation of Kodak EDR2 film for dose verification of intensity modulated radiation therapy delivered by a static multileaf collimator,” Med. Phys. **29**, 1687-1692 (2002).[67]